Spin dynamics in hybrid spintronic devices and semiconductor nanostructures

Spin dynamics in hybrid spintronic devices and semiconductor nanostructures

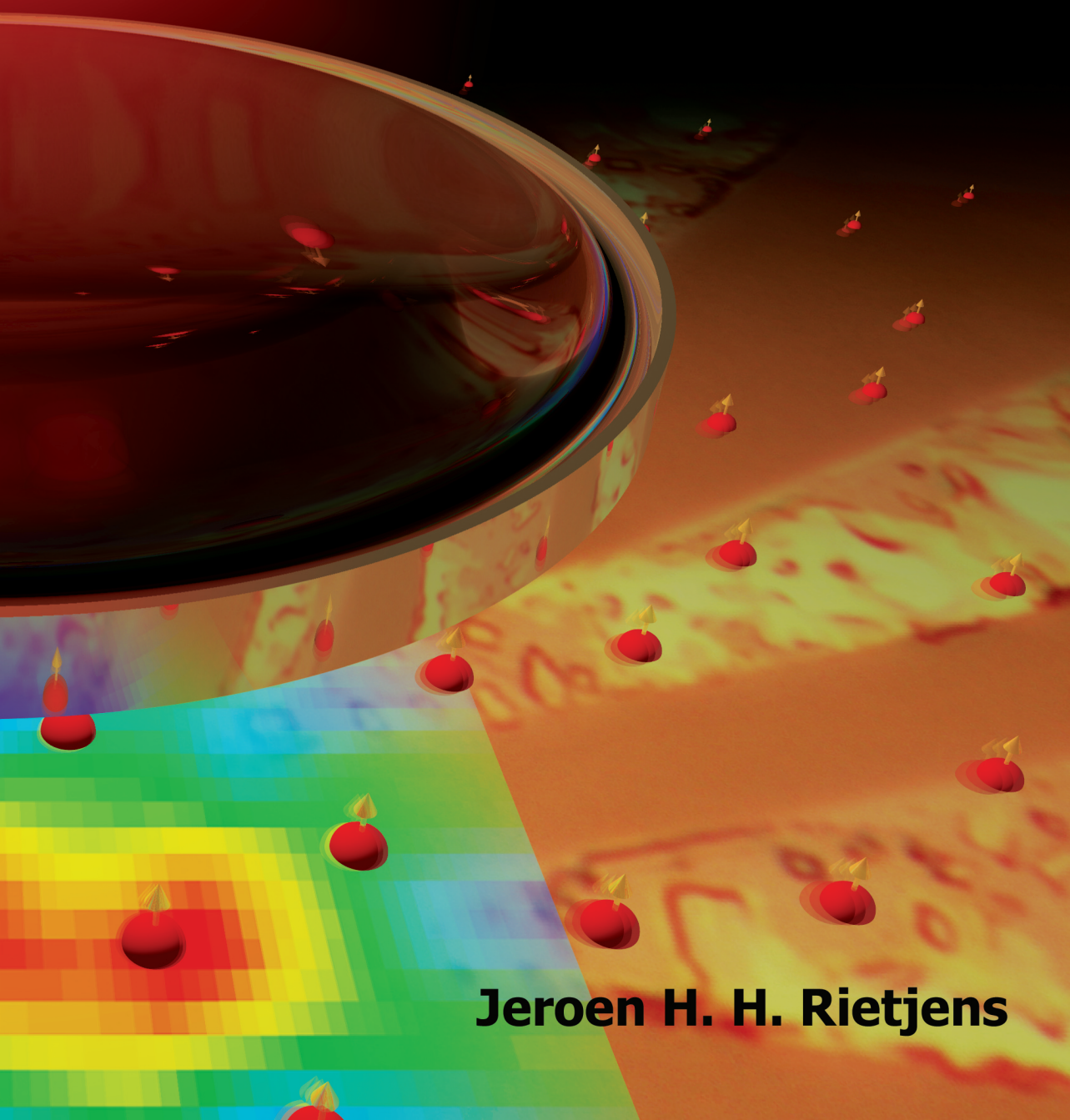

Jeroen H. H. Rietjens

Spin dynamics in hybrid spintronic devices and semiconductor nanostructures

PROEFSCHRIFT

ter verkrijging van de graad van doctor
aan de Technische Universiteit Eindhoven,
op gezag van de Rector Magnificus,
prof.dr.ir. C.J. van Duijn,
voor een commissie aangewezen door het College voor Promoties
in het openbaar te verdedigen
op maandag 9 februari 2009 om 16.00 uur

door

Jeroen Henricus Hubertus Rietjens

geboren te Weert

Dit proefschrift is goedgekeurd door de promotoren:

prof.dr. B. Koopmans
en
prof.dr.ir. H.J.M. Swagten

Copromotor:
dr. E.P.A.M. Bakkers

A catalogue record is available from the Eindhoven University of Technology Library

ISBN: 978-90-386-1525-7

The work described in this Thesis has been carried out in the group Physics of Nanostructures, at the Department of Applied Physics of the Eindhoven University of Technology, the Netherlands.

This research was supported by NanoNed, a national nanotechnology program coordinated by the Dutch Ministry of Economic Affairs. Flagship NanoSpintronics. Project number 7160 / 6473 - 2C1.

Printed by Universiteitsdrukkerij Technische Universiteit Eindhoven

Cover design by Jeroen Rietjens and Frans Snik

Dedicated to:

Huub,

Femke

en

Guus

Contents

Chapter 1

Introduction

At the end of the nineteenth century, the general consensus among physicists was that most of nature was quite well understood, and that nature offered physics as a scientific discipline no big secrets yet to be unveiled. A few problems still existed, such as the interpretation of experiments regarding photo-emission from metals, and difficulties with the concept of the ether as a medium for light propagation, but these were not labeled as big issues. The general consensus could not have been more wrong. The emergence of relativity and quantum mechanics during the following decades not only completely changed our view on the universe, it also fueled the revolutionary changes to society of the past century, leading to the electronics, and information eras. The development of a quantum theory of solids, with the introduction of the concept of band structure, has led to a profound understanding of solid state materials. Especially the invention of the solid state transistor can be seen as the starting point of the semiconductor industry and the ongoing miniaturization of electronic circuitry, leading to ever faster computers, and hand-held consumer electronics such as mobile phones and palmtops, to name a few examples.

1.1 Spintronics

Quantum mechanics and relativity have also led to the concept of spin, which is the intrinsic magnetic moment of an elementary particle. The most common elementary particle, the electron, also has, besides its elementary charge, a finite intrinsic magnetic moment. The orientation of the spin can be parallel or anti-parallel to a quantization axis (e.g. the direction of a magnetic field), leading to the terms spin up and spin down. This electron spin forms the basis of a relatively young, but very active and successful research field, named Spintronics [1–3]. This research field tries to utilize the spin degree of freedom in conventional charge based electronics, or in conceptual new devices, in order to obtain improved device performance and new functionalities. More fundamentally, it involves the study of the active control

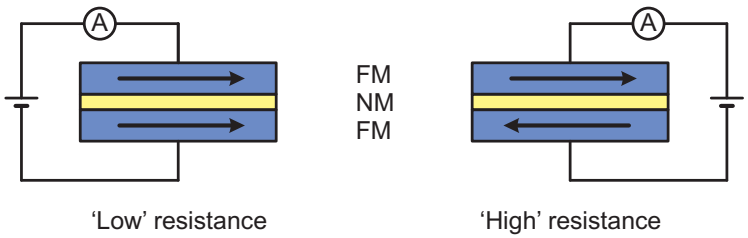

Figure 1.1: Schematic illustration of the GMR and TMR effect, in which a parallel alignment of the magnetization of the two ferromagnetic (FM) electrodes has a lower resistance than an anti-parallel alignment. In the case of GMR, the non-magnetic (NM) layer is a metal, in the case of TMR the NM layer is an insulator.

and manipulation of spin in solid state systems. One key achievement that gave a huge boost to the field is the discovery of the Giant-Magneto-Resistance-effect (GMR-effect) by Albert Fert [4] and Peter Grünberg [5], who have been awarded the Nobel Prize in Physics of 2007 for their discovery. The GMR-effect enabled the tremendous increase in data storage capabilities of computer hard-disk drives over the past decade by implementing the effect (within an astonishing ten years after the discovery) into a very sensitive magneto-resistive sensor in the read-head of the hard-disk. Another key discovery is the large room-temperature Tunnel-Magneto-Resistance-effect (TMR-effect) in 1995 [6], which nowadays replaces the GMR-effect in sensors, and which might lead to a universal non-volatile solid state memory, the magnetic random access memory (MRAM).

Let us briefly discuss the GMR-effect and TMR-effect in more detail, with the help of Fig. 1.1. Consider a tri-layer consisting of two ferromagnetic (FM) materials, separated by a non-magnetic (NM) spacer. In the case of GMR, the non-magnetic spacer is a conductor, such as Cu, with a thickness of the order of a few nanometer. The tri-layer is referred to as a spin-valve. The resistance of this structure depends on the relative orientation of the magnetization of the magnetic layers, as a result of spin dependent scattering of electrons in the magnetic layers. When the electron spin is parallel (anti-parallel) with the magnetization, the scattering probability is low (high), which results is a low (high) resistance. The total current is carried by spin up as well as by spin down electrons. Using the two-channel picture of spin transport, first introduced by Mott, it can be readily seen that a parallel orientation of the magnetization of the two FM layers has a lower total resistance than an anti-parallel orientation. With GMR, the resistance changes that can be achieved with such a tri-layer are typically of the order 20%. A crucial aspect in this system is that the thickness of the non-magnetic spacer layer is lower than the spin scattering length, such that spin is conserved when electrons transverse from one magnetic layer to the other. When the non-magnetic spacer layer is an insulator of $\approx 1-2$

nanometer thickness, it acts as a tunnel barrier. In this case, the tri-layer is referred to as a magnetic tunnel junction. The tunneling rates of spin up and spin down electrons are (to first order) dependent on the density of filled states in one electrode times the density of empty states the other electrode, both at the Fermi level. With the presence of the FM layers, these tunneling rates depend on the spin type, and on the relative orientation of the magnetization of the two FM layers. Again, a parallel alignment of the magnetization results in lower resistance than an anti-parallel alignment.

These two systems thus convert magnetic information (the relative orientation of the magnetization of the two FM layers) to electric information (via the resistance), which can be processed with standard electronics. Engineering of the properties of the FM layers, e.g. via interlayer coupling and exchange bias, have led to the development of very accurate magnetic field sensors based on the GMR-effect. Also, the record high TMR-values of up to 70% with CoFeB as a magnetic electrode and AlOx as an isolating spacer [7], and well over 500% with CoFeB and MgO [8–10], pave the way for implementing magnetic tunnel junction as memory elements in a non-volatile solid state memory. In combination with a design that uses the so-called spin transfer torque [11, 12] to switch the magnetization of one of the ferromagnetic electrodes (i.e. the magnetization is switched by a spin polarized current, instead of with a magnetic field), this could lead to a universal scalable magnetic solid state memory [13].

Besides the material aspects, also the dynamic properties of the magnetic electrodes are important, e.g. in the case of fast switching of the magnetization of the electrode. Magnetization dynamics at GHz frequencies takes place in the so-called precessional regime, which means that the magnetization can only be switched by a precessional motion. The fasted switch possible is that of half a precession period, called a ballistic switch. Experimentally, ballistic precessional switching via magnetic field pulses has been demonstrated in micron and sub-micron sized magnetic elements [14, 15], while similar results are being pursued using spin transfer switching [16, 17]. These achievements form a complementary step towards the development of magnetic memories.

The above mentioned spin valve and magnetic tunnel junction are examples of metallic spintronic applications. In order to fully utilize the spin degree of freedom in conventional electronics, a spin polarization must be created, manipulated, transported, and detected in conventional semiconductors. The research field which studies these aspects is named Semiconductor Spintronics.

1.2 Semiconductor Spintronics

Semiconductor spintronics has the promise of improved device performance over current and future charge-based semiconductor technology [18]. Several proposals and experimental studies include a spin-FET (field-effect transistor [19, 20], see Fig.

1.2a), a spin-LED (light-emitting diode), a spin-RTD (resonant tunneling diode), and quantum bits for quantum computation and communication. Typical questions that are posed in respect of these proposals are: How can a significant spin polarization be created in a (typically) non-magnetic semiconductor, such as Si or GaAs? How can a spin polarization be efficiently and electrically detected? What are the mechanisms for spin relaxation, and can a spin polarization be maintained long enough to perform spin manipulation and / or transport? What are ways to manipulate a spin polarization, in order to obtain device functionality? In the past decade an enormous progress has been made in finding solutions to these questions, which we will consider in more detail below.

Spin injection and detection

The oldest and most easiest way to create a non-equilibrium spin polarization in a non-magnetic semiconductor is by optical means [21]. Circularly polarized photons can transfer angular momentum to the semiconductor via the optical selection rules of direct band-gap semiconductors, thereby exciting more electrons of one spin type than of the other. However, for device applications it is desirable to have an electrical method for creating a spin polarization, which is often referred to as electrical spin injection. First attempts were based on depositing ferromagnetic contacts on InAs. InAs is one of the few semiconductors with an ideal interface to a transition metal, resulting in low Ohmic contacts without Schottky barrier formation. However, later it was realized that the large difference in conductivity between a FM and a semiconductor results in a low spin injection efficiency, an obstacle referred to as the conductivity mismatch [22]. Using semiconductors as a source of spin polarization, either via spin splitting in a large magnetic field [23], or by using a ferromagnetic semiconductor such as GaMnAs [24], efficient spin injection into GaAs could be achieved at low temperatures and / or high magnetic field. These methods did, however, not allow room temperature spin injection. This conductivity mismatch problem could be circumvented by introducing a tunnel barrier between the FM and semiconductor, which acts as a large spin dependent resistance [25]. Indeed, successful electrical spin injection into GaAs has been achieved using a Schottky-barrier [26], and an insulating barrier such as AlOx [27], and MgO [28]. To prove successful spin injection, most studies used a LED-structure underneath the injection electrode, a configuration also referred to as spin-LED. The degree of circular polarization of the electroluminescence originating from this spin-LED is related to the injected spin polarization. More recently, spin injection into Si was demonstrated in a similar way [29].

The above demonstrations of spin injection relied, as mentioned, on optical detection of light emission from a spin-LED. Naturally, in view of application in devices, a more convenient way would be electrical detection of spin injection. This is, however, a much more difficult task, because either a lateral geometry of the electrodes is needed, or spin transport through a full wafer. Electrical detection of

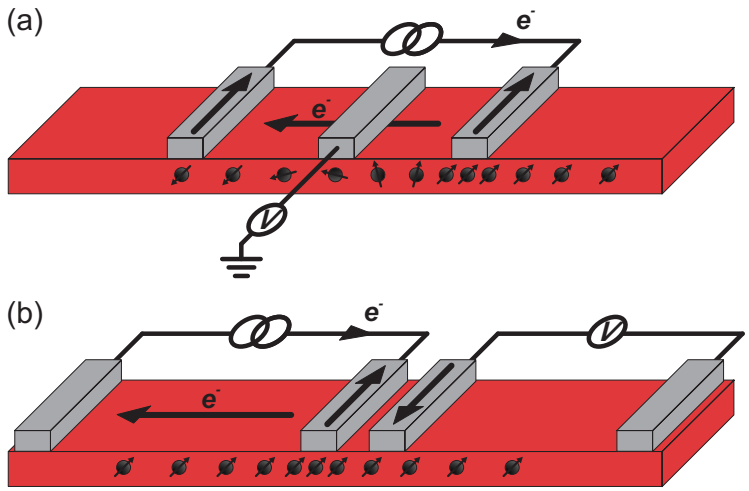

Figure 1.2: (a) Schematic picture of the Datta-Das spin-transistor, in which spins are injected at one FM electrode (right electrode), rotated by a gate-voltage on the middle electrode via the Rashba-effect [43], and detected at a second FM electrode. The transistor is 'on' ('off') when the spin are parallel (anti-parallel) to the detection electrode. (b) Schematic picture of a lateral spin injection and detection device with a non-local geometry.

spin accumulation was demonstrated with a multi-terminal device [30], and later full electrical spin injection and detection in GaAs [31], and also Si [32], using a non-local lateral geometry (see Fig. 1.2b). We note that a non-local measurement is needed in order to rule out spurious effects, such as magnetoresistance in the electrodes, and local Hall effects. Spin transport through a full 300 μm Si wafer was demonstrated using hot electron spin injection [33, 34].

A completely different way to generate a (non-equilibrium) spin polarization in a semiconductor is by exploiting the spin-Hall effect. This is the effect that a charge current induces a spin polarization of opposite sign perpendicular to the current direction, similar to the Hall voltage in the ordinary Hall effect. The separation of spin up and spin down electrons is a spin-orbit effect, and results from a spin dependent scattering potential seen by the electrons. In this case no ferromagnetic contact or external magnetic field is needed to create a spin polarization. The spin Hall effect has been demonstrated in GaAs and InGaAs channels [35]. The investigation of the full potential of the spin Hall effect as a source of spin polarization in semiconductors is currently an active research topic.

Spin relaxation, transport, and manipulation

A huge boost to the interest in semiconductor spintronics was the discovery of long room temperature spin relaxation times in non-magnetic semiconductors, which are three order of magnitude longer than in metals [36]. Such high relaxation times are needed to perform spin manipulation and transport. In $n-$GaAs, spin relaxation times up to 100 ns were measured at low temperatures (< 5 K) [37], while the spin relaxation mechanisms were identified for different donor concentrations [38]. Soon after this discovery, several groups reported on spin transport in electric, magnetic, and strain fields, using optical injection and detection of spins [39–41]. Later, also lateral spin transport was optically imaged using electrical injection of spins [42]. These studies proved that spin packages can be transported by electric fields over more than 100 μm in $n-$GaAs at low temperature.

Besides spin relaxation and transport, several studies aimed at the active control of spin dynamics. The Datta-Das spin transistor relies on spin manipulation via the Rashba-effect [43], but other methods involve controlling the magnitude of the electron g factor (and thereby the precession frequency) [44], or applying short electric tipping pulses [45]. Other studies focused on the manipulation of spin relaxation in $n-$GaAs with stray fields originating from patterned ferromagnetic structures [46–48]. Despite this enormous progress, demonstration of a spin-transistor according to the Datta-Das proposal remains one of the big challenges for semiconductor spintronics.

Single spins

Up to now we have only discussed systems in which a spin ensemble is injected, transported, manipulated, and detected. For applications in the field of quantum computation and information, however, it it desirable to gain control over single spins [49]. A single spin is an ideal two-level quantum system, which can be used as a quantum bit (qubit), the building block of a quantum computer. One way of isolating a single spin is by using semiconductor quantum dots, either by forming electrostatically defined quantum dots with lateral gate electrodes [50], or by incorporating the dots in a semiconductor matrix via self-assembly during growth [51]. In recent years, experimental studies on ensemble and single dots have confirmed long spin decoherence times in several quantum dot systems [52]. Also schemes for single spin manipulation in quantum dots have been demonstrated, thereby taking the first essential steps for using semiconductor quantum dots as qubits for quantum computation.

1.3 This Thesis

The main focus of this Thesis is on the dynamic behavior of magnetization and ensemble spins in various hybrid spintronic devices and semiconductor nanostruc-

tures. We will focus on magnetization dynamics in an MRAM element, and on spin relaxation and precession in lateral and perpendicular spin injection devices. Also, we will explore the possibilities of optical spin injection in semiconductor nanowires, and try to identify the main spin relaxation mechanism in such wires. Finally, we will investigate the possibility of controlling the electron or hole g factor in self-assembled semiconductor quantum dots.

This Thesis is organized as follows. In Chapter 2 we will discuss the basic theoretical aspects of magnetization dynamics in ferromagnetic thin layers, and of spin orientation, relaxation and precession in semiconductors, with a focus on $n-$doped GaAs. Chapter 3 gives a description of the measurement techniques used throughout this Thesis, which are for a large part based on the magneto-optical Kerr-effect. This effect is explained in detail, and a model is presented which calculates the Kerr-effect originating from an arbitrary layered structure. This Chapter also presents unpublished experimental results related to perpendicular magnetized electrodes for spin injection, and measurements of spin relaxation, precession, and diffusion in a lateral spin injection device. Precessional magnetization dynamics in a micron sized ferromagnetic element is the subject of Chapter 4. In this Chapter, the questions related to uniform magnetization switching via precessional motion in a potential MRAM element will be addressed. Chapter 5 is devoted to the determination and understanding of electron spin relaxation in a spin-LED under operational conditions. The influence of important device parameters, such as carrier densities, temperature, and recombination rate on the spin relaxation rate will be the central topic. The potential applicability of semiconductor nanowires as building blocks for spintronic applications will be investigated in Chapter 6, with the emphasis on carrier and spin dynamics in these nanowires. We will show that by using microscopic techniques, it is possible to optically study individual nanowires. Chapter 7 concludes this Thesis and is dedicated to spin relaxation and precession of electrons and holes in self-assembled semiconductor quantum dots. The central question is if it is possible to control the electron or hole g factor by changing the internal electric field.

Bibliography

[1] S. A. Wolf, D. D. Awschalom, R. A. Buhrman, J. M. Daughton, S. von Molnár, M. L. Roukes, A. Y. Chtchelkanova, and D. M. Treger, *Spintronics: A spin-based electronics vision for the future*, Science **294**, 1488-1495 (2001). 1.1

[2] I. Žutić, J. Fabian, S. Das Sarma, *Spintronics: Fundamentals and applications*, Rev. Mod. Phys. **76**, 323-410 (2004).

[3] C. Chappert, A. Fert, and Frédéric Nguyen Van Dau, *The emergence of spin electronics in data storage*, Nat. Mater. **6**, 813-823 (2007). 1.1

[4] M. N. Baibich, J. M. Broto, A. Fert, F. Nguyen Van Dau, F. Petroff, P. Eitenne, G. Creuzet, A. Friederich, and J. Chazelas, *Giant magnetoresistance of (001)Fe/(001)Cr magnetic superlattices*, Phys. Rev. Lett. **61**, 2472-2475 (1988). 1.1

[5] G. Binasch, P. Grünberg, F. Saurenbach, and W. Zinn, *Enhanced magnetoresistance in layered magnetic structures with antiferromagnetic interlayer exchange*, Phys. Rev. B **39**, 4828-4830 (1989). 1.1

[6] J. S. Moodera, L. R. Kinder, T. M. Wong, and R. Meservey, *Large magnetoresistance at room temperature in ferromagnetic thin film tunnel junctions*, Phys. Rev. Lett. **74**, 3273-3276 (1995). 1.1

[7] D. Wang, C. Nordman, J. M. Daughton, Z. Qian, and J. Fink, 70% *TMR at room temperature for SDT sandwich junctions with CoFeB as free and reference layers*, IEEE Trans. Magn. **40**, 2269-2271 (2004). 1.1

[8] S. S. P. Parkin, C. Kaiser, A. Panchula, P. M. Rice, B. Hughes, M. Samant, and S.-H. Yang, *Giant tunnelling magnetoresistance at room temperature with MgO (100) tunnel barriers*, Nat. Mater. **3**, 862-867 (2004). 1.1

[9] S. Yuasa, T. Nagahama, A. Fukushima, Y. Suzuki, and K. Ando, *Giant room-temperature magnetoresistance in single-crystal Fe/MgO/Fe magnetic tunnel junctions*, Nat. Mater. **3**, 868-871 (2004).

[10] S. Ikeda, J. Hayakawa, Y. Ashizawa, Y. M. Lee, K. Miura, H. Hasegawa, M. Tsunoda, F. Matsukura, and H. Ohno, *Tunnel magnetoresistance of* 604% *at 300 K by suppression of Ta diffusion in CoFeB/MgO/CoFeB pseudo-spin-valves annealed at high temperature*, Appl. Phys. Lett. **93**, 082508 (2008). 1.1

[11] J. C. Slonczewski, *Current-driven excitation of magnetic multilayers*, J. Magn. Magn. Mater. **159**, L1-L7 (1996). 1.1

[12] L. Berger, *Emission of spin waves by a magnetic multilayer transversed by a current*, Phys. Rev. B **54**, 9353-9358 (1996). 1.1

[13] T. Kawahara, R. Takemura, K. Miura, J. Hayakawa, S. Ikeda, Y. M. Lee, R. Sasaki, Y. Goto, K. Ito, T. Meguro, F. Matsukura, H. Takahashi, H. Matsuoka, and H. Ohno, *2 Mb SPRAM (SPin-Transfer Torque RAM) With Bit-by-Bit Bi-Directional Current Write and Parallelizing-Direction Current Read*, IEEE J. Sol. St. Circ. **43**, 109 (2008). 1.1

[14] Th. Gerrits, H. A. M. van den Berg, J. Hohlfeld, L. Bär, and Th. Rasing, *Ultrafast precessional magnetization reversal by picosecond magnetic field pulse shaping*, Nature (London) **418**, 509-512 (2002). 1.1

[15] H. W. Schumacher, C. Chappert, R. C. Sousa, P. P. Freitas, and J. Miltat, *Quasiballistic magnetization reversal*, Phys. Rev. Lett. **90**, 017204 (2003). 1.1

[16] T. Devolder, J. Hayakawa, K. Ito, H. Takahashi, S. Ikeda, P. Crozat, N. Zerounian, Joo-Von Kim, C. Chappert, and H. Ohno, *Single-Shot Time-Resolved Measurements of Nanosecond-Scale Spin-Transfer Induced Switching: Stochastic Versus Deterministic Aspects*, Phys. Rev. Lett. **100**, 057206 (2008). 1.1

[17] S. Serrano-Guisan, K. Rott, G. Reiss, J. Langer, B. Ocker, and H. W. Schumacher, *Biased Quasiballistic Spin Torque Magnetization Reversal*, Phys. Rev. Lett. **101**, 087201 (2008). 1.1

[18] D. D. Awschalom, and M. Flatté, *Challenges for semiconductor spintronics*, Nat. Phys. **3**, 153-159 (2007). 1.2

[19] S. Datta, and B. Das, *Electronic analog of the electrooptic modulator*, Appl. Phys. Lett. **56**, 665-667 (1990). 1.2

[20] K. C. Hall, W. H. Lau, K. Gündoğdu, M. E. Flatté, and T. F. Boggess, *Nonmagnetic semiconductor spin transistor*, Appl. Phys. Lett. **83**, 2937-2939 (2003). 1.2

[21] *Optical Orientation* (Modern Problems in Condensed Matter Sciences, Vol. 8), edited by F. Meier, and B. P. Zachachrenya (North-Holland, Amsterdam, 1984). 1.2

[22] G. Schmidt, D. Ferrand, L. W. Molenkamp, A. T. Filip, and B. J. van Wees, *Fundamental obstacle for electrical spin injection from a ferromagnetic metal into a diffusive semiconductor*, Phys. Rev. B **62**, R4790-R4793 (2000). 1.2

[23] R. Fiederling, M. Kleim, G. Reuscher, W. Ossau, G. Schmidt, A. Waag, and L. W. Molenkamp, *Injection and detection of a spin-polarized current in a light-emitting diode*, Nature (London) **402**, 787-790 (1999). 1.2

[24] Y. Ohno, D. K. Young, B. Beschoten, F. Matsukura, H. Ohno, and D. D. Awschalom, *Electrical spin injection in a ferromagnetic semiconductor heterostructure*, Nature (London) **402**, 790-792 (1990). 1.2

[25] E. I. Rashba, *Theory of electrical spin injection: Tunnel contacts as a solution of the conductivity mismatch problem*, Phys. Rev. B **62**, R16267-R16270 (2000). 1.2

[26] A. T. Hanbicki, B. T. Jonker, G. Itskos, G. Kioseoglou, and A. Petrou, *Efficient electrical spin injection from a magnetic metal/tunnel barrier contact into a semiconductor*, Appl. Phys. Lett. **80**, 1240-1242 (2002). 1.2

[27] V. F. Motsnyi, V. I. Safarov, J. De Boeck, J. Das, W. Van Roy, E. Goovaerts, and G. Borghs, *Electrical spin injection in a ferromagnet/tunnel barrier/semiconductor heterostructure*, Appl. Phys. Lett. **81**, 265-267 (2002). 1.2

[28] X. Jiang, R. Wang, R. M. Shelby, R. M. Macfarlane, S. R. Bank, J. S. Harris, and S. S. P. Parkin, *Highly spin-polarized room-temperature tunnel injector for semiconductor spintronics using MgO(100)*, Phys. Rev. Lett. **94**, 056601 (2005). 1.2

[29] B. T. Jonker, G. Kioseoglou, A. T. Hanbicki, C. H. Li, and P. E. Thompson, *Electrical spin-injection into silicon from a ferromagnetic metal/tunnel barrier contact*, Nat. Phys. **3**, 542 (2007). 1.2

[30] X. Lou, C. Adelmann, M. Furis, S. A. Crooker, C. J. Palmstrøm, and P. A. Crowell, *Electrical detection of spin accumulation at a ferromagnet-semiconductor interface*. Phys. Rev. Lett. **96**, 176603 (2006). 1.2

[31] X. Lou, C. Adelmann, S. A. Crooker, E. S. Garlid, J. Zhang, K. S. Madhukar Reddy, S. D. Flexner, C. J. Palmstrøm, and P. A. Crowell, *Electrical detection of spin transport in lateral ferromagnet-semiconductor devices*, Nat. Phys. **3**, 197-202 (2007). 1.2

[32] O. M. J. van 't Erve, A. T. Hanbicki, M. Holub, C. H. Li, C. Awo-Affouda, P. E. Thompson, and B. T. Jonker, *Electrical injection and detection of spin-polarized carriers in silicon in a lateral transport geometry*, Appl. Phys. Lett. **91**, 212109 (2007). 1.2

[33] I. Appelbaum, B. Huang, and D. Monsma, *Electronic measurement and control of spin transport in silicon*, Nature (London) **447**, 295 (2007). 1.2

[34] B. Huang, D. Monsma, and I. Appelbaum, *Coherent Spin Transport through a 350 Micron Thick Silicon Wafer*, Phys. Rev. Lett. **99**, 177209 (2007) 1.2

[35] Y. K. Kato, R. C. Myers, A. C. Gossard, and D. D. Awschalom, *Observation of the spin Hall effect in semiconductors*, Science **306**, 1910-1913 (2004). 1.2

[36] J. M. Kikkawa, I. P. Smorchkova, N. Samarth, and D. D. Awschalom, *Room-temperature spin memory in two-dimensional electron gases*, Science **277**, 1284-1287 (1997). 1.2

[37] J. M. Kikkawa, and D. D. Awschalom, *Resonant spin amplification in n-type GaAs*, Phys. Rev. Lett. **80**, 4313-4316 (1998). 1.2

[38] R. I. Dzhioev, K. V. Kavokin, V. L. Korenev, M. V. Lazarev, B. Y. Meltser, M. N. Stepanova, B. P. Zakharchenya, D. Gammon, and D. S. Katzer, *Low-temperature spin relaxation in n-type GaAs*, Phys. Rev. B **66**, 245204 (2002). 1.2

[39] J. M. Kikkawa, and D. D. Awschalom, *Lateral drag of spin coherence in gallium arsenide*, Nature (London) **397**, 139-141 (1999). 1.2

[40] Y. K. Kato, R. C. Myers, A. C. Gossard, and D. D. Awschalom, *Coherent spin manipulation without magnetic fields in strained semiconductors*, Nature (London) **427**, 50-53 (2004).

[41] S. A. Crooker, and D. L. Smith, *Imaging spin flows in semiconductors subject to electric, magnetic, and strain fields*, Phys. Rev. Lett. **94**, 236601 (2005). 1.2

[42] S. A. Crooker, M. Furis, X. Lou, C. Adelmann, D. L. Smith, C. J. Palmstrøm, and P. A. Crowell, *Imaging spin transport in lateral ferromagnet/semiconductor structures*, Science **309**, 2191-2195 (2005). 1.2

[43] Yu. A. Bychkov, and E. I. Rashba, *Oscillatory effects and the magnetic susceptibility of carriers in inversion layers*, J. Phys. C: Solid State Phys. **17**, 6039-6045 (1984). 1.2, 1.2

[44] G. Salis, Y. Kato, K. Ensslin, D. C. Driscoll, A. C. Gossard, and D. D. Awschalom, *Electrical control of spin coherence in semiconductor nanostructures*, Nature (London) **414**, 619-622 (2001). 1.2

[45] Y. Kato, R. C. Myers, D. C. Driscoll, A. C. Gossard, J. Levy, and D. D. Awschalom, *Gigahertz electron spin manipulation using voltage-controlled g-tensor modulation*, Science **299**, 1201-1204 (2003). 1.2

[46] L. Meiera, G. Salis, C. Ellenberger, K. Ensslin, and E. Gini, *Stray-field-induced modification of coherent spin dynamics*, Appl. Phys. Lett. **88**, 172501 (2006). 1.2

[47] S. Halma, G. Bacher, E. Schuster, W. Keune, M. Sperl, J. Puls, and F. Henneberger, *Local spin manipulation in ferromagnet-semiconductor hybrids*, Appl. Phys. Lett. **90**, 051916 (2007).

[48] P. E. Hohage, J. Nannen, S. Halm, G. Bacher, M. Wahle, S. F. Fischer, U. Kunze, D. Reuter, and A. D. Wieck, *Coherent spin dynamics in Permalloy-GaAs hybrids at room temperature*, Appl. Phys. Lett. **92**, 241920 (2008). 1.2

[49] D. Loss, and D. P. DiVincenzo, *Quantum computation with quantum dots*, Phys. Rev. A **57**, 120-122 (1998). 1.2

[50] R. Hanson, L. P. Kouwenhoven, J. R. Petta, S. Tarucha, and L. M. K. Vandersypen, *Spins in few-electron quantum dots*, Rev. Mod. Phys. **79**, 1217-1265 (2007). 1.2

[51] M. S. Skolnick, and D. J. Mowbray, *Self-assembled semiconductor quantum dots: Fundamental Physics and Device Applications*, Annu. Rev. Mater. Res. 34, 181-218 (2004). 1.2

[52] M. Paillard, X. Marie, P. Renucci, T. Amand, A. Jbeli, and J. M. Gérard, *Spin Relaxation Quenching in Semiconductor Quantum Dots*, Phys. Rev. Lett. **86**, 1634 (2001). 1.2

Chapter 2

Magnetization and spin dynamics

This Chapter discusses the main physical processes and phenomena that are needed to explain and discuss experimental data in Chapters 3 to 7, but which are not treated in depth in these Chapters. We will first discuss the general concepts of magnetization precession and spin waves in ferromagnets, which we will encounter in Chapter 4. Next, we will focus on optical spin orientation in semiconductors, and the main spin relaxation mechanisms in bulk and quantum systems, which will be important in Chapters 5-7. Special attention will be given to spin relaxation in bulk $n-GaAs$. The final topic is spin precession and dephasing in semiconductors, which will be relevant in Chapters 3 and 7.

2.1 Magnetization dynamics in ferromagnets

The magnetization of a ferromagnet is a local quantity that describes in which direction an ensemble of local magnetic moments (spins) is aligned. The direction of this magnetization can usually be changed by applying a magnetic field. A strong magnetic field will in general align all the magnetic moments of a ferromagnet in the same direction, a situation which is called saturation. In magnetic storage devices, such as hard disk-drives or magnetic random access memory, the binary data is stored as the parallel or anti-parallel alignment of the magnetization direction with respect to a preset axis in small magnetic grains or elements. Nowadays, it is required that the writing of the data, and thus the switching of the magnetization, occurs on a (sub-)nanosecond time-scale. On this timescale, the magnetization dynamics in ferromagnets is governed by the Landau-Lifshitz-Gilbert (LLG) equation [1–3]. This equation describes the motion of the local magnetization vector, and takes the following form

$$\frac{d\vec{m}(\vec{x},t)}{dt} = \gamma\mu_0 \left(\vec{m}(\vec{x},t) \times \vec{H}_{eff}(\vec{x},t)\right) + \frac{\alpha}{M_s}\left(\vec{m}(\vec{x},t) \times \frac{d\vec{m}(\vec{x},t)}{dt}\right). \tag{2.1}$$

Here, $\vec{m}(\vec{x},t) = \vec{M}(\vec{x},t)/M_s$ is the normalized local magnetization vector, γ the gyromagnetic ratio ($\gamma = g\frac{e}{2m_e}$, with g the gyromagnetic splitting factor of the electron in the magnetic material, and e and m_e the electron charge and mass respectively), μ_0 the magnetic permeability of vacuum and $\vec{H}_{eff}(\vec{x},t)$ the local effective magnetic field, M_s the saturation magnetization, and α a phenomenological (Gilbert) parameter, which is a measure of the damping in the system [2, 3]. This equation states that the local effective magnetic field exerts a torque on the local magnetization, and that this torque is responsible for the motion of the magnetization. This motion is a precessional motion around the local effective field, since the direction of the torque is perpendicular to both the magnetization vector, and the local effective field. Depending on the value of α, the precessional motion can be over-damped, critically damped or under-damped. In most cases with thin magnetic layers, $\alpha \ll 1$, and the motion is in the under-damped regime, leading to many revolutions of the magnetization vector (also called ringing). The local effective field is the sum of several different fields, which include the exchange field, the dipole field (or demagnetizing field), crystalline and shape anisotropy, coupling fields from neighboring layers (via exchange bias or interlayer coupling), and the externally applied magnetic field. In particular, the exchange and dipole field give rise to short and long range interactions, respectively, between local magnetic moments, and can thereby induce spin-waves [4]. We will not discuss all the aspects of spin waves in detail, but state here three important classes of lateral spin waves encountered in thin magnetic elements. These classes are defined by the relative orientation of the magnetization $\vec{M}$, the wavevector, $\vec{q}$, of the spin wave, and the normal of the sample plane $\vec{n}$. For $\vec{n} \parallel \vec{M} \perp \vec{q}$, we have the so-called forward volume magnetostatic mode , for $\vec{n} \perp \vec{M} \perp \vec{q}$, it is the Damon-Eshbach surface mode [5], and for $\vec{n} \perp \vec{M} \parallel \vec{q}$, the spin

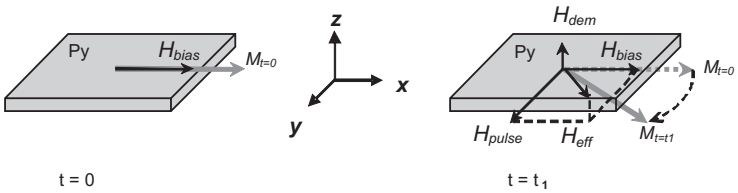

Figure 2.1: Geometry for simulating magnetization dynamics with the LLG-equation. The external bias field (H_{bias}), and initial magnetization ($M_{t=0}$) of the Py ($Ni_{80}Fe_{20}$) element are in the $\hat{x}$ direction. The magnetic field pulse (H_{pulse}) is applied in the $\hat{y}$ direction. The effective field (H_{eff}) at $t = t_1$ is the sum of H_{bias}, H_{pulse}, and the demagnetization field (H_{dem}). The motion of the magnetization vector is also indicated.

waves are referred to as the backward volume magnetostatic spin waves (BWVMS) [6]. These BWVMS will be important in Chapter 4, and are interesting because of their particular (negative) dispersion relation. In micrometer sized ferromagnetic elements, quantization of the wavevector of these spin waves can occur when the wavelength of the waves becomes comparable to the size of the element [7]. Also, in regions with a strong inhomogeneous internal magnetic field, localization of modes can occur [8, 9]. This localization is a result of the dispersion relation of the spin waves, which ensures that waves with a certain wavevector can only exist in a limited internal magnetic field range. We will encounter such localized spin waves in Chapter 4.

We will briefly show an illustrative example of the excitation of the magnetization by a short magnetic field pulse. We consider only a region of a thin ferromagnetic layer with a spatially uniform magnetization. We neglect the exchange and dipolar fields from neighboring regions, and assume only shape anisotropy is present in the system. For thin films, the shape anisotropy in the perpendicular direction is dominant, and we assume there is no preferential in-plane direction for the magnetization. The magnetization is in this case no longer dependent on position, and Eq. 2.1 simplifies considerably to

$$\frac{d\vec{m}(t)}{dt} = \gamma\mu_0 \left(\vec{m}(t) \times \vec{H}_{eff}(t)\right) + \frac{\alpha}{M_s}\left(\vec{m}(t) \times \frac{d\vec{m}(t)}{dt}\right). \tag{2.2}$$

This equation can be linearized for all three components of the magnetization vector, and integrated with the effective magnetic field as input. We use the geometry sketched in Fig. 2.1, which shows all the relevant contributions to $\vec{H}_{eff}$ for this particular example. The response of the magnetization to a short (0.25 ns) square magnetic field pulse is presented Fig. 2.2, with $\alpha = 0.01$, and $M_s = 900$ kA/m. The magnetization is initially aligned along the $\hat{x}$ direction by an external bias field in the same direction. For $t < 0$ this is the only contribution to $\vec{H}_{eff}$, and as $\vec{M}$ and $\vec{H}_{eff}$ are parallel, no torque is exerted on $\vec{M}$. At $t = 0$ ns, a magnetic field pulse

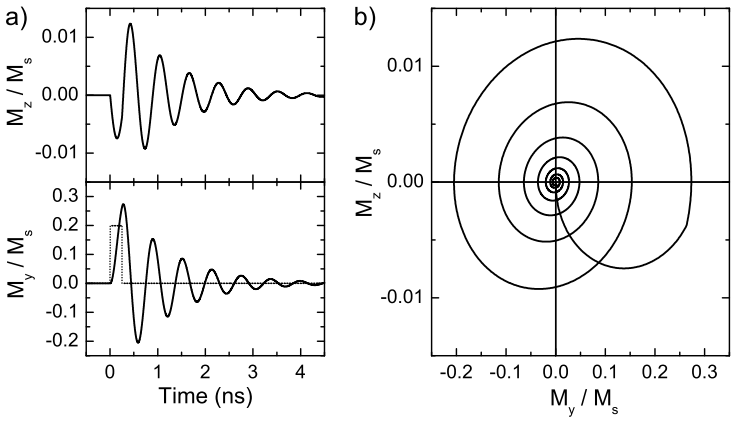

Figure 2.2: The responses of the magnetization due to a magnetic field pulses of 0.25 ns, plotted (a) in a $m_y - t$, and a $m_z - t$ graph, and (b) in a $m_z - m_y$ graph. In the $m_y - t$ graph of (a) also the field pulse (with amplitude 0.4 kA/m) is plotted. In the calculation, $\alpha = 0.01$, and $M_s = 900$ kA/m.

is applied in the $\hat{y}$ direction, which changes $\vec{H}_{eff}$, and a finite torque is exerted on the magnetization in the $-\hat{z}$ direction. The magnetization rotates out of the plane, which is accompanied by a strong demagnetization field in the $+\hat{z}$ direction, as shown in Fig. 2.1. After $t = 0$ ns, the effective field is the sum of the bias field, the field pulse, and the demagnetization field. While the field pulse is present, the magnetization precesses around the new $\vec{H}_{eff}$. However, as the duration of the field pulse is smaller than the period of the precession, $\vec{H}_{eff}$ changes again when the field pulse ends, and the magnetization starts to precess around the initial equilibrium axis in the $\hat{x}$ direction. This precession is clearly shown in Fig. 2.2b, and its amplitude decays on a timescale set by α. In real experiments, usually the $z-$component of the magnetization is measured, and the signals that are obtained are similar to Fig. 2.2a(top). From such measurements, the precession frequency and damping parameter can be easily extracted.

2.2 Optical orientation in semiconductors

In contrast to ferromagnets, the traditional semiconductors are not magnetic, and therefore in equilibrium no net spin polarization is present. However, as stated in the Introduction, semiconductors are of great interest for spintronic applications. The reason for this is mainly due to the fact that one is nowadays able to create a non-equilibrium spin polarization in a wide range of semiconductor systems that lasts long enough to perform spin transport and manipulation experiments, which may

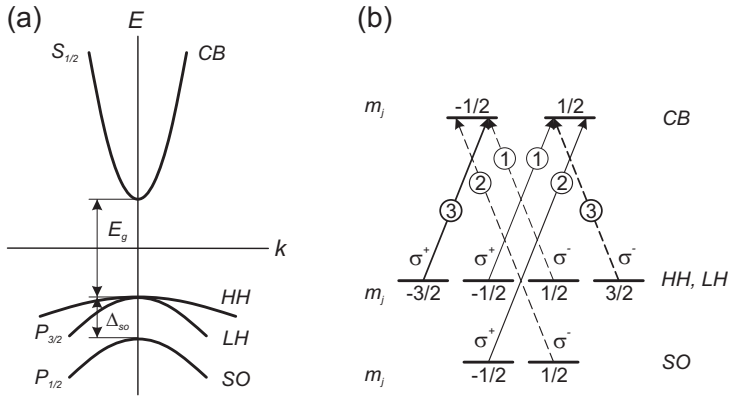

Figure 2.3: (a) Schematic band structure of GaAs near the $\Gamma-$point, with the conduction band (CB), and valence bands heave hole (HH), light hole (LH), and spin-orbit split-off (SO). The bandgap E_g, spin-orbit splitting Δ_{so}, and the angular momenta of the bands are indicated. (b) The selection rules for interband transitions between the m_j sub-levels in the valence and conduction band. σ^- and σ^+ indicate excitations with left- and right-circularly polarized light, while the circled numbers indicate the relative transition intensities for each excitation.

lead to useful applications in the (near) future. In this Section we will briefly discuss the physics of optical orientation, which is the creation of a non-equilibrium spin ensemble in a semiconductor by optical means. It forms the basis of the experimental techniques to study spin relaxation in bulk and quantum systems, which we shall encounter in Chapters 5, 6, and 7.

Optical orientation has been extensively studied, both theoretically and experimentally [10]. In the latter case, the most widely studied material is GaAs, which is characteristic for III/V and II/VI semiconductors with the zinc-blende crystal structure. Here, we shall also focus on GaAs, as this is the material which is mostly used in the devices and nanostructures studied in this Thesis. The band structure of GaAs near the Γ-point is shown in Fig. 2.3a [11]. The bandgap E_g is 1.52 eV at $T = 0$ K, while the split-off band is separated from the light- and heavy-hole band by $\Delta_{so} = 0.34$ eV. The conduction (CB) and valence (heavy hole, HH, and light hole, LH) bands are parabolic, with a much smaller effective mass of electrons in the conduction band, compared to holes in the valence bands. Optical excitation follows the dipole selection rules for interband transitions for this zinc-blende crystal structure. The eigenmodes of the photons for such transitions are left- and right-handed circular polarization, denoted as σ^- (negative helicity), and σ^+ (positive helicity), respectively. $\sigma^\pm$ photons cause transitions with $\Delta m_j = \pm 1$, as indicated in Fig. 2.3b. The relative intensity of the transitions depends on the specific valence elec-

trons involved: 3 for HH-transitions, 1 for LH-transitions, and 2 for SO-transitions. It follows that excitation with σ^+ photons with an energy $E_g < \hbar\omega < E_g + \Delta_{so}$ ($\hbar$ is Planck's constant h divided by 2π, and ω the photon angular frequency) results in a spin polarization of

$$P = \frac{n_\uparrow - n_\downarrow}{n_\uparrow + n_\downarrow} = \frac{1-3}{1+3} = -\frac{1}{2}. \tag{2.3}$$

Strictly speaking this is only true for transitions at the Γ-point, as for transitions away from the Γ-point the electron and hole wavefunctions become coupled to other bands. For transitions close to the Γ-point, the coupling is small, and Eq. 2.3 is a good approximation. Excitation with a photon energy $\hbar\omega > E_g + \Delta_{so}$ should thus result in zero spin polarization. However, in this case electrons from the HH-band and LH-band are excited relatively high in the conduction band, and their spin polarization will decrease while cooling to the bottom of the conduction band. Electrons excited from the SO-band have much less excess energy, and cooling is relatively unimportant. The result is a net positive spin polarization of a few percent.

2.3 Spin relaxation mechanisms

In the previous Section we have discussed a useful method for creating a non-equilibrium spin polarization in semiconductors. Naturally, this spin polarization will not last forever as a result of spin relaxation. Several mechanisms for spin relaxation have been identified: Elliott-Yafet (EY), D'yakonov-Perel' (DP), Bir-Aronov-Pikus (BAP), and hyperfine-interaction (HF) [10, 12]. We shall discuss the basic concepts of these mechanisms below.

Elliot-Yafet-mechanism

In the EF-mechanism, electron spins relax via momentum scattering events, because the electron wave functions are an admixture of both spin states due to spin-orbit coupling [13, 14]. At each scattering event of electrons with impurities or phonons, there is thus a finite (though small) probability of a spin-flip. An analytical formula for the spin relaxation rate due to the EF-mechanism is given by [15, 16]

$$\frac{1}{\tau_s} \propto \left(\frac{\Delta_{so}}{E_g + \Delta_{so}}\right)^2 \left(\frac{E_k}{E_g}\right) \frac{1}{\tau_p(E_k)}, \tag{2.4}$$

where τ_p is the momentum scattering time at energy E_k. From this formula, we see that the EF-mechanism is more efficient in materials with a small band-gap, and for high electron energy. Also, we see that the spin relaxation time is proportional to the momentum scattering time, as expected.

Because holes have a non-zero orbital moment ($L = 1$), spin-orbit coupling in the valence band leads to complete admixture of orbital and spin moments of holes.

Due to this complete admixture, the EF-mechanism predicts a hole spin relaxation time of the order of the momentum scattering time, which is typically less than one ps in bulk-semiconductors.

D'yakonov-Perel'-mechanism

In the DP-mechanism, spin relaxation is mediated by the internal effective magnetic field, which is the result of spin-splitting of the conduction band in crystals lacking inversion symmetry [17]. The internal magnetic field leads to spin precession of electrons. When the precession period is much longer than the momentum scattering time, the electron spin rotates a small angle about the magnetic field between each momentum scattering event. Because the spin-splitting, and thus the direction of the internal magnetic field, is k-dependent, the electron spin rotates in different directions after each scattering event. This leads to a random walk of the spin orientation, and finally to spin relaxation. In this case, the shorter the momentum scattering time, the less efficient the DP-mechanism (in contrast to the EF-mechanism). Also, the higher the electron energy, the larger the spin splitting in the conduction band, and the faster the spin precession and spin relaxation. An analytical formula for the spin relaxation rate due to the DP-mechanism is given by [16]

$$\frac{1}{\tau_s} \propto \tau_p(E_k)\alpha^2 \frac{E_k^3}{E_g}, \tag{2.5}$$

with α a dimensionless parameter specifying the strength of the spin-orbit coupling. From this equation we can see that $1/\tau_s$ increases much faster with electron energy than for the EF-case, and it is expected that the DP-mechanism is dominant at large donor concentration (n_D) and high temperature (T). For degenerate semiconductors, τ_p is given by [18]

$$\frac{1}{\tau_p} \propto \frac{n_D}{E_F^{3/2}} \left[\ln(1+x) - \frac{x}{1+x} \right], \tag{2.6}$$

with $x \propto E_F/n_D^{1/3}$, and E_F the Fermi level. We see that τ_p increases with increasing Fermi level, and decreases with increasing donor concentration. In the absence of optically excited carriers, E_F is determined entirely by the donor concentration, via $E_F \propto n_D^{2/3}$ (see also Eq. 2.14). For this case we can rewrite Eq. 2.5 after substitution of Eq. 2.6, and obtain

$$\frac{1}{\tau_s} \propto \frac{E_g}{n_D^2} \left[\ln(1+x) - \frac{x}{1+x} \right]. \tag{2.7}$$

From this formula it follows that for spin relaxation at the Fermi level $\tau_s \propto n_D^{-\nu}$, with $\nu < 2$ as a result of the (weak) dependence of the term between the square brackets on n_D. In the presence of optically excited carriers, ν will be larger as

a result of the explicit dependence of τ_p on E_F (which increases with increasing excitation density). We shall implement the DP-mechanism in the case of $n-$GaAs, together with carrier recombination, in a model that calculates the time evolution of a spin distribution after optical orientation. This is described in the next Section.

Bir-Aronov-Pikus-mechanism

In the BAP-mechanism, electron scattering with holes involving spin flip is the dominant process [19, 20]. This process is mediated by the electron-hole exchange interaction. The spin-flip scattering probability depends on the state of the holes (bound to acceptors or free, non-degenerate or degenerate, fast or slow). For the case of non-degenerate holes, and including both bound and free holes, the spin relaxation rate is given by

$$\frac{1}{\tau_s} \propto \frac{< \bar{D_s^2} >}{E_B} \frac{v_e}{v_B} \left(n_A a_B^3\right) \left(\frac{p}{n_A} |\psi(0)|^4 + \frac{5}{3} \frac{n_A - p}{n_A} \right), \tag{2.8}$$

with D_s the exchange constant, E_B and a_B the Bohr-energy, and -radius for the exciton respectively, $v_B = \frac{\hbar}{m_e a_B}$, and m_e and v_e the electron effective mass and velocity, respectively. p is the free hole density, n_A the acceptor density (and thus the density of bound holes), while $|\psi(0)|^2$ is the Sommerfield-factor, which is a measure for the screening of the Coulomb-potential between the electron and hole.

For the case of degenerate holes, and fast electrons ($v_e > v_F$, with v_F the Fermi-velocity of the holes), the spin relaxation rate is given by

$$\frac{1}{\tau_s} \propto \frac{< \bar{D_s^2} >}{E_B} \frac{v_e}{v_B} \left(p a_B^3\right) \frac{T}{E_F} |\psi(0)|^4. \tag{2.9}$$

The strength of the BAP-mechanism depends on the hole density according to $1/\tau_s \sim n_A$ for non-degenerate holes (Eq. 2.8), and according to $1/\tau_s \sim p^{1/3}$ for degenerate holes (Eq. 2.9, with $E_F \propto p^{2/3}$, see also Eq. 2.14). In the intermediate regime only a weak dependence on p is observed. The temperature dependence of τ_s for degenerate holes is given by Eq. 2.9, from which it follows that (with $v_e = \sqrt{3k_BT/m_e}$, k_B Boltzmann's constant) $1/\tau_s \propto T^{3/2}$. Measurements of the temperature dependence of τ_s in GaAs by Aronov *et al.* [16], could be well described by the expression

$$1/\tau_s = 2.3 \cdot p^{1/3} T^{3/2}, \tag{2.10}$$

with τ_s in seconds, p in cm^{-3} and T in Kelvin. We will use this equation in Chapter 5 to compare our data with the theoretical predictions. We note that BAP is the dominant mechanism in heavily $p-$doped samples at relatively low temperatures. Due to the strong energy dependence in the DP-mechanism, spin relaxation via DP will dominate at high temperature, even at high acceptor concentrations.

Hyperfine-interaction

Finally, in the HF-mechanism, the combined random magnetic moments of nuclei lead to a fluctuating magnetic field experienced by localized or confined electrons. The HF-mechanism is too weak in bulk semiconductors to be dominant over EY and DP, due to the itinerant nature of the electrons. It is, however, an important mechanism for single-spin decoherence of localized electrons, e.g. electrons confined in quantum dots or bound to donors. For these electrons, the DP mechanism is suppressed, leading to very large spin relaxation times.

2.4 Modeling spin relaxation in $n-$GaAs

Spin relaxation in $n-$GaAs is extensively studied during the last decades, following the discovery of large spin relaxation times exceeding 100 ns for moderate doping levels [18, 21]. For donor concentrations above the metal-insulator transition (thus $> 2{\cdot}10^{16}$ cm^{-3}) the spin relaxation is mediated by the DP-mechanism. In Chapter 3 we will discuss the experimental technique used in this Thesis to study spin relaxation in several devices and semiconductor nanostructures. An example, presented to outline the capabilities of the technique, involves a semiconductor heterostructure with a $n-$GaAs transport channel. Here, we will present a simple model to describe spin relaxation in $n-$GaAs as a function of excitation density, including the effect of recombination.

In order to model the spin relaxation in a $n-$GaAs layer, we will assume a uniform doping profile, and uniform carrier excitation. Also, we will set the temperature to $T = 0$. The electron density due to doping is equal to the donor concentration, n_D, while the density of electrons due to laser excitation is n_L. Following the optical selection rules for zinc-blende crystal structures, the spin up density, $\bar{n}_\uparrow$, right after laser excitation is given by $\bar{n}_\uparrow = \frac{1}{2}n_D + \frac{3}{4}n_L$, while the spin down density, $\bar{n}_\downarrow$, is given by $\bar{n}_\downarrow = \frac{1}{2}n_D + \frac{1}{4}n_L$. The bar indicates the total spin up and spin down density respectively, i.e. integrated over all electron energies in the conduction band. The situation after laser excitation and thermalization is schematically shown in Fig. 2.4. We are interested in the net electron spin moment, S, as a function of time after laser excitation, which is given in units of $\hbar/2$ by

$$S(t) = \bar{n}_\uparrow(t) - \bar{n}_\downarrow(t) = \int_{E_g}^{E_{F\uparrow}(t)} n(E)dE - \int_{E_g}^{E_{F\downarrow}(t)} n(E)dE. \tag{2.11}$$

Here, $n(E)$ is the density of states function in the conduction band, while $E_{F,\uparrow(\downarrow)}(t)$ represent the time-dependent electron quasi-Fermi level for spin up (down) electrons. When the electron quasi-Fermi level for spin up and spin down electrons is different, there will be a net flow of majority spins to minority spins due to spin relaxation, until the electron quasi-Fermi level of each spin band is equal, and the net spin

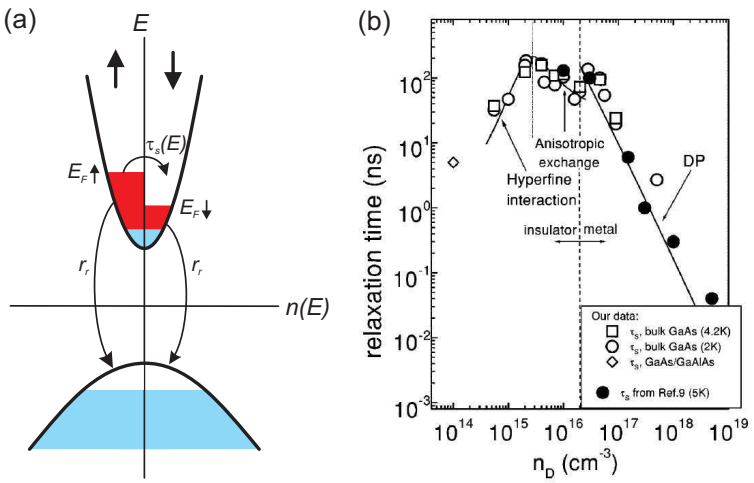

Figure 2.4: (a) Schematic representation of the spin dependent density of states after laser excitation in $n-$GaAs. The conduction band (CB), valence band (VB), and the processes of spin relaxation and recombination are indicated. τ_s is the spin relaxation time, r_r represents the recombination parameter. (b) Spin relaxation time as a function of donor concentration in GaAs, adapted from [18]. The DP-calculation for $10^{16} < n_D < 10^{19}$ can be approximated with $\tau_s \propto n_D^{-1.77}$.

moment is zero. Spin flip events of both spin up and spin down electrons take place at all electron energies, and since spin relaxation is mediated by the DP-mechanism, the spin flip rate depends strongly on the electron energy. In the following we will present the equations of the model for only the spin up density. The spin down density is found by interchanging the $\uparrow$'s and $\downarrow$'s. The rate equation for the spin up density is given by

$$\frac{d\bar{n}_\uparrow(t)}{dt} = -\int_{E_g}^{E_{F\uparrow}(t)} \frac{n(E)}{\tau_s(E)} dE + \int_{E_g}^{E_{F\downarrow}(t)} \frac{n(E)}{\tau_s(E)} dE. \tag{2.12}$$

The first term on the right hand side represents the loss of spin up electrons due to spin flips, while the second term represents the gain of spin up electrons due to spin flips of spin down electrons. $\tau_s(E)$ is the energy dependent spin relaxation time according to the DP-mechanism. In order to carry out the integrals, it is convenient to express the total spin density in terms of the (time-dependent) electron quasi-Fermi level. From the formula for the 3D density of states in the conduction band,

$$n(E) = 8\pi\sqrt{2}\left(\frac{m_e}{h^2}\right)^{3/2}\sqrt{E - E_g} = n_0\sqrt{E - E_g}, \tag{2.13}$$

with n_0 a constant introduced for convenience, it follows that

$$\bar{n}_{\uparrow}(E_{F\uparrow}(t)) = \int_{E_g}^{E_{F\uparrow}(t)} n(E)dE = \frac{2}{3}n_0 \left(E_{F\uparrow}(t) - E_g\right)^{3/2}. \tag{2.14}$$

We take the dependence of τ_s on n_D, as presented by Dzhioev *et al.* [18], to calculate the spin flip time for each electron energy. Their theoretical estimation can be approximated by

$$\tau_s(n_D) = c_D n_D^{-1.77}, \tag{2.15}$$

with c_D a constant which has the numerical value $1.23 \cdot 10^{22}$ if n_D is expressed in units of cm^{-3}. As mentioned in the previous Section, the absolute value of the exponent of n_D is slightly smaller than 2 in the absence of optically excited carriers. However, for simplicity we will also use this expression in the presence of optically excited carriers, and replace n_D with $(n_D + n_L)$. In doing so, we underestimate the electron spin relaxation rate at high excitation density. In the experiments of Dzhioev *et al.* the electron quasi-Fermi levels of both sub-bands after optical orientation are nearly equal, and close to the equilibrium Fermi level. This means that electron spin relaxation takes place at the equilibrium Fermi level. Therefore, we can replace the donor concentration n_D with the electron (spin up or spin down) concentration, and use Eq. 2.14 with $E_{F\uparrow} = E$, to express τ_s as a function of energy, yielding

$$\tau_s(E) = c_D \left(\frac{2}{3}n_0\right)^{-1.77} (E - E_g)^{-2.66}. \tag{2.16}$$

Substituting Eqs. 2.13, 2.14, and 2.16 in Eq. 2.12, carrying out the integrals, rearranging, and setting $E_g = 0$ (which does not affect the calculation), results in

$$\frac{dE_{F\uparrow}(t)}{dt} = \frac{\left(\frac{2}{3}n_0\right)^{1.77}\left(-E_{F\uparrow}(t)^{4.16} + E_{F\downarrow}(t)^{4.16}\right)}{4.16 c_D \sqrt{E_{F\uparrow}(t)}}. \tag{2.17}$$

This equation, together with its spin down counterpart, describes the electron spin relaxation in $n-$GaAs via the DP-mechanism for various donor concentrations, and excitation densities.

However, besides spin relaxation, also recombination with unpolarized holes (the hole spin relaxation time is extremely short, as mentioned in the previous Section) takes place. The recombination of spin up (down) electrons is proportional to the electron spin up (down), and hole spin down (up) density. The amount of recombination events might thus be different for spin up and spin down electrons as a result of a difference in their densities. The recombination of spin up electrons can be expressed as

$$\frac{d\bar{n}_{\uparrow}(t)}{dt}|_{rec} = -r_r \bar{n}_{\uparrow}(t)\bar{p}_{\downarrow}(t) = -r_r \bar{n}_{\uparrow}(t)\frac{1}{2}[\bar{n}_{\uparrow}(t) + \bar{n}_{\downarrow}(t) - n_D], \tag{2.18}$$

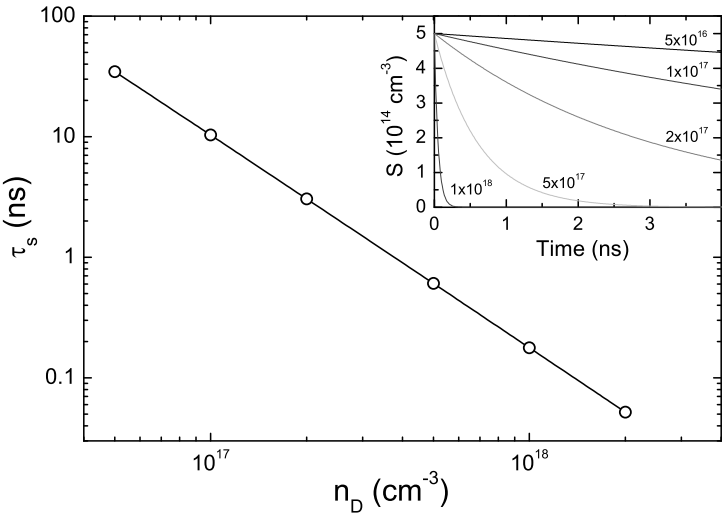

Figure 2.5: Calculated spin relaxation times τ_s as a function of donor density n_D. The inset shows the time traces produced by the model. Single exponential fits to these traces yield the spin relaxation time presented in the main graph.

with r_r the recombination parameter, and $\bar{p}_\downarrow$ the total hole spin down density. Using again Eq. 2.14, we can express Eq. 2.18 in terms of the quasi-Fermi levels, and obtain (with $E_g = 0$)

$$\frac{dE_{F\uparrow}(t)}{dt}|_{rec} = -\frac{r_r E_{F\uparrow}(t)}{3}\left(\frac{2}{3}n_0\left(E_{F\uparrow}(t)^{3/2} + E_{F\downarrow}(t)^{3/2}\right) - n_D\right). \qquad (2.19)$$

The right-hand side of Eq. 2.19 can be added to the right-hand side of Eq. 2.17, thereby obtaining the full rate equation for the spin up density. Together with the similar equation for the spin down density this forms a system of two coupled differential equations, which can be solved in order to obtain $E_{F\uparrow}(t)$ and $E_{F\downarrow}(t)$. Using Eq. 2.12 we obtain $\bar{n}_\uparrow(t)$ and $\bar{n}_\downarrow(t)$. Substituting these quantities in Eq. 2.11 finally yields $S(t)$, the evolution of the total spin density as a function of time. We have employed a numerical technique to solve the coupled differential equations, and have calculated $S(t)$ for several values of the input parameters n_D, n_L, and r_r.

First, we verified that the model agrees with the paper of Dzhioev *et al.*, which should be the case because the data of Dzhioev *et al.* serves as an input. Therefore, we calculated the spin relaxation time for several donor concentration in the low fluence limit ($n_L \ll n_D$). This means that we used a laser induced electron concentration of 1×10^{15} cm^{-3}, much smaller than all the donor concentrations. Figure 2.5 shows the calculated spin relaxation times, as well as the time traces produced by the model in the inset. Comparison with Fig. 2.4b shows that indeed the same

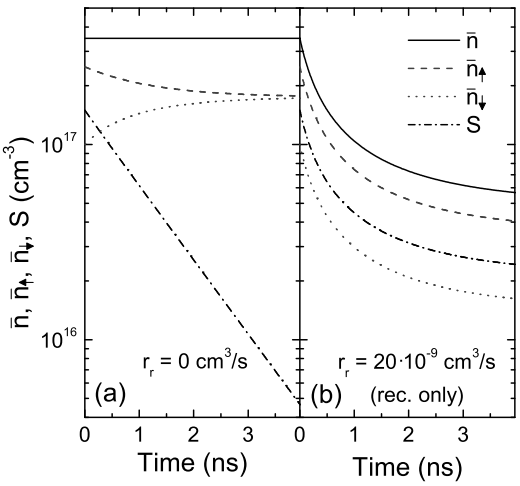

Figure 2.6: Calculated total spin S, the total carrier ($\bar{n}$), total spin up ($\bar{n}_\uparrow$), and total spin down ($\bar{n}_\downarrow$) density for the case of only spin relaxation (a) and only recombination (b). The input parameters of the model are $n_D = 5 \times 10^{16}$ cm^{-3}, $n_L = 3 \times 10^{17}$ cm^{-3}.

dependence of τ_s on n_D is reproduced.

A more interesting application of the model is to study the spin relaxation in the case of high fluence ($n_L > n_D$). First, we will focus on the effect on S of (i) only spin relaxation, and (ii) only recombination. We set $n_D = 5 \times 10^{16}$ cm^{-3}, $n_L = 3 \times 10^{17}$ cm^{-3}, so $\bar{n} = 3.5 \times 10^{17}$ cm^{-3} at $t = 0$. We choose this value for n_D, because this is the donor concentration of the device discussed in Section 3.3.3. Figure 2.6 shows the total spin S, the total carrier ($\bar{n}$), total spin up ($\bar{n}_\uparrow$), and total spin down ($\bar{n}_\downarrow$) density for the two cases. If only spin relaxation is present, and no recombination, Fig. 2.6a shows that $\bar{n}$ is constant. $\bar{n}_\uparrow$ decreases while $\bar{n}_\downarrow$ increases due to spin flips, resulting in a decay of S, which can be well approximated with a single exponential decay with time constant $\tau_s = 1.13$ ns. This time constant is similar to the case of low excitation density, with $n_D = 3.5 \times 10^{17}$ cm^{-3}. Apparently, the spin relaxation time is determined by the total carrier density, and is only weakly changed by an initial large spin up and spin down imbalance. If only recombination is present, and no spin relaxation, Fig. 2.6b shows a non-exponential decay of the carrier density, which follows from Eq. 2.18 because $\bar{p}_\downarrow$ is time-dependent. Also, because at $t = 0$ $\bar{n}_\uparrow > \bar{n}_\downarrow$, unequal recombination rates for spin up and spin down electrons are observed. This leads to a net loss of spin polarization, and thus to a decrease of S.

When both spin relaxation and recombination are present, it is expected that the spin relaxation rate due to spin flips is time-dependent. This follows from the DP-

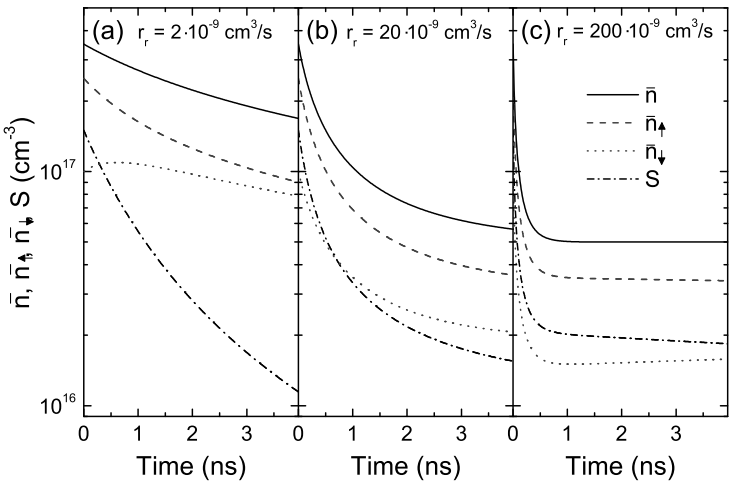

Figure 2.7: Calculated total spin S, the total carrier ($\bar{n}$), total spin up ($\bar{n}_\uparrow$), and total spin down ($\bar{n}_\downarrow$) density for three different recombination parameters. The input parameters of the model are $n_D = 5\times10^{16}$ cm^{-3}, $n_L = 3\times10^{17}$ cm^{-3}.

mechanism, according to which the spin flip rate depends on the spin up and spin down density. Due to recombination, these densities decrease, thereby decreasing the spin flip rate. In Figure 2.7 we show the results of calculations (S, $\bar{n}$, $\bar{n}_\uparrow$, and $\bar{n}_\downarrow$) with again $n_D = 5\times10^{16}$ cm^{-3}, and $n_L = 3\times10^{17}$ cm^{-3}, for three different values for the recombination parameter r_r.

We want to focus on a few aspects of these results. Firstly, the effect of the recombination parameter on $\bar{n}$ is clearly visible: the higher r_r the faster the decay of $\bar{n}$. Secondly, in Fig. 2.7a the relatively little loss of spin down electrons due to recombination is compensated by spin flips of spin up electrons during the first ns. In (b) and (c) recombination is initially the dominant process, leading to a decrease of $\bar{n}_\downarrow$ and a fast decrease of S. Finally, the spin polarization S after full recombination strongly depends on r_r. With a small r_r, the densities $\bar{n}_\uparrow$, and $\bar{n}_\downarrow$ remain relatively high for several ns, leading to fast spin relaxation at these high densities. When r_r is large, the laser excited carriers recombine quickly, leaving only a short time-interval with a high spin flip rate, and a marginal loss of S due to spin flip events. After full recombination, S is larger when r_r is large, as can be seen in Fig. 2.7.

The model presented above enables the calculation of the relaxation of an optically induced spin polarization in $n-$GaAs in the moderate to high fluence regime, where the optically induced carrier density is comparable or higher than the donor concentration. In the next Section, we will address spin precession and dephasing in

$n-$GaAs, which is the result of application of a transverse external magnetic field.

2.5 Spin precession and dephasing

When a single electron is placed in a magnetic field, its energy depends on the orientation of its spin with respect to the direction of the magnetic field. The energy difference between spin up (parallel to the field) and spin down (anti-parallel to the field) electrons is the Zeeman-energy and is given by

$$\Delta E_Z = E_{Z,\uparrow} - E_{Z,\downarrow} = -g\mu_B B, \tag{2.20}$$

with $E_{Z,\uparrow(\downarrow)}$ the energy of the spin up (down) electron, g the electronic g factor, μ_B the Bohr-magneton, and B the magnetic induction. The eigenstates of the spin part of the electron wavefunction are $\psi_\uparrow$ (spin up) and $\psi_\downarrow$ (spin down), with respect the quantization axis in the $\hat{z}$ direction when the magnetic field is $B = (0, 0, B_z)$. A spin orientated parallel to the $\hat{x}$ direction can then be represented as a superposition of these eigenstates, according to

$$\psi(t) = \frac{\psi_\uparrow}{2} \exp\left(-\frac{\imath E_{Z,\uparrow}}{h} t\right) + \frac{\psi_\downarrow}{2} \exp\left(-\frac{\imath E_{Z,\downarrow}}{h} t\right), \tag{2.21}$$

For this spin wavefunction, the expectation value of the $x-$component of the spin is

$$S_x(t) = \langle \psi(t)^* | \sigma_x | \psi(t) \rangle = \frac{\hbar}{2} \cos\left(\frac{\Delta E_Z}{h} t\right), \tag{2.22}$$

with σ_x the Pauli spin operator for the $\hat{x}$ direction. A similar analysis for the $\hat{y}$ and $\hat{z}$ direction reveals that the spin evolves according to a precessional motion around the magnetic field. In the case of optical orientation in a solid, the orientation of the spin polarization is parallel to the direction of light propagation (or anti-parallel, depending on the helicity of the photons), and usually normal to the sample surface. In the presence of a transverse magnetic field, this means that the spins are created in a coherent superposition of the spin up and spin down states with respect to the transverse magnetic field. The whole spin density will then undergo a precessional motion with a frequency given by $\omega = \Delta E_Z/\hbar$. The frequency is thus proportional to the g factor.

In solids, the g factor depends on the electron energy [22–24]. For GaAs e.g. the g factor is given by $g = g_0 + \beta E$, with $g_0 = -0.44$ and $\beta = 6.3$ eV^{-1}. This means that under optical orientation in the high fluence regime, the g factor of electron spins is time-dependent due to carrier recombination, because recombination lowers the (average) energy of the electrons. In the presence of a transverse magnetic field, and if the carrier recombination time τ_r is much shorter than the spin relaxation time τ_s, this leads to a precession frequency that changes in time.

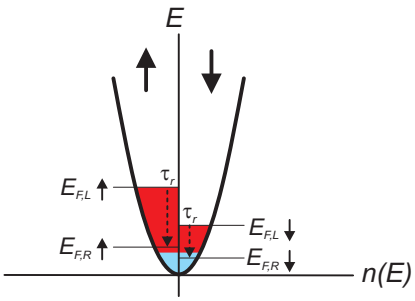

Figure 2.8: Schematic representation of the spin dependent density of states in the conduction band after laser excitation in $n-$GaAs. The electron quasi-Fermi levels after excitation (index L), and after recombination (index R), are indicated. τ_r represents the recombination time.

In view of the example presented in Chapter 3, we will analyze the consequences of an energy dependent g factor in more detail. For simplicity, and in contrast to the model of the previous paragraph, we will neglect spin relaxation due to spin flips, and simulate the recombination process by an exponentially decreasing electron quasi-Fermi level, as indicated in Fig. 2.8. Using Eq. 2.14, the electron quasi-Fermi levels of spin up and spin down after excitation are

$$E_{F,L\uparrow} = \left[\frac{3}{2n_0}\left(\frac{1}{2}n_D + \frac{3}{4}n_L\right)\right]^{2/3}, E_{F,L\downarrow} = \left[\frac{3}{2n_0}\left(\frac{1}{2}n_D + \frac{1}{4}n_L\right)\right]^{2/3}, \quad (2.23)$$

respectively, while the electron quasi-Fermi levels after recombination ($E_{F,R\uparrow}$, and $E_{F,R\downarrow}$) can be fixed in order to have a finite remaining spin polarization. We model the precession of spin up and spin down electrons separately, and keep track of the precession phase of electrons not lost in the recombination process. The precession phase as a function of time is given by

$$\phi(t) = \int_0^t \omega(t')dt' = \int_0^t -g(E(t'))\frac{\mu_B B}{\hbar}dt' = \int_0^t -(g_0 + \beta E(t'))\frac{\mu_B B}{\hbar}dt'. \quad (2.24)$$

We calculate the time-dependent projection of the spin moment on the initial orientation direction for each energy, and integrating over the full energy range between E_g and $E_g + E_{F\uparrow(\downarrow)}$ gives the total projection of spin up (down) electrons as a function of time. The net spin projection is equal to the difference between the spin up and spin down projections. As an example, we plot in Fig. 2.9 the calculated result for the initial parameters $n_D = 5\cdot 10^{16}$ cm^{-3}, $n_L = 2.5\cdot 10^{17}$ cm^{-3}, a recombination time $\tau_r = 300$ ps, and a magnetic field of $B = 1$ T. We fix the final spin polarization after recombination at $2.0\cdot 10^{16}$ cm^{-3}, similar to the result of Fig. 2.7c.

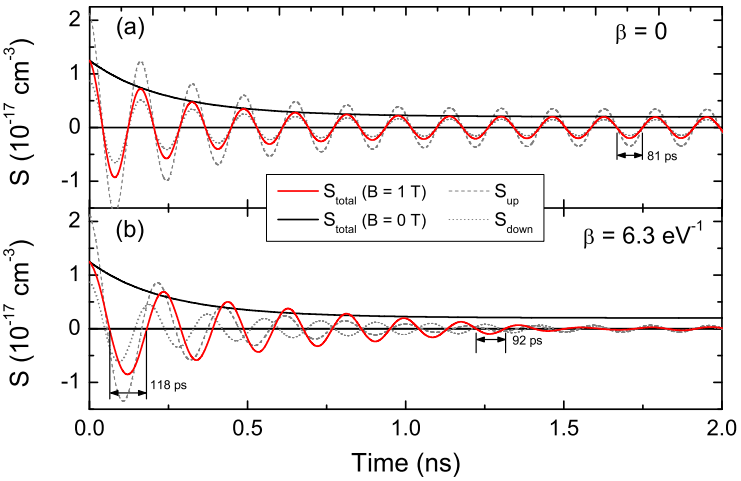

Figure 2.9: Calculated total spin S, the total carrier ($\bar{n}$), total spin up ($\bar{n}_\uparrow$), and total spin down ($\bar{n}_\downarrow$) density for the case of (a) no energy dependent g factor ($\beta = 0$), and (b) an energy dependent g factor ($\beta = 6.3$ eV^{-1}). The input parameters of the model are $n_D = 5 \times 10^{16}$ cm^{-3}, $n_L = 2.5 \times 10^{17}$ cm^{-3}, and $\tau_r = 300$ ps.

Fig. 2.9a shows the net spin precession if we do not include an energy-dependent g factor (i.e. $\beta = 0$). A constant precession period of 162 ps is observed, which follows from a g factor of -0.44. Also the separate contributions for spin up and spin down are shown, as well as the evolution of the spin density in the absence of an applied magnetic field. We note that the phase of the spin up and spin down contributions is equal, and that the curve with $B = 0$ T nicely forms the envelope of the curve with $B = 1$ T. Taking the energy dependence of the g factor into account, thus $\beta = 6.3$ eV^{-1}, yields the result plotted in Fig. 2.9b. Several differences with Fig. 2.9a can be observed. Firstly, the precession period is not constant in time, changing gradually from an initial 236 ps ($g = -0.302$) to 184 ps ($g = -0.387$). We thus observe the effect of an energy dependent g factor on the net precession, which result in a decrease of precession period with time due to a decreasing carrier density. After full recombination, the total carrier density is equal to the donor density ($n_D = 5 \cdot 10^{16}$ cm^{-3}). At this carrier density, the absolute value of the g factor is expected to be slightly smaller than 0.44. Secondly, the separate contributions of spin up and spin down electrons are no longer in phase. Because the average energy of spin up and spin down is different due to the large initial spin polarization (which results from optical orientation), the precession period is different for spin up and spin down electrons, leading to a phase shift. Finally, the evolution of the spin density in the absence of an applied magnetic field no longer forms the envelope of the net spin

precession. For $0.15 < t < 0.85$ ns, the maxima of the net spin precession are larger than the zero field curve, whereas for $t > 1$ ns, the maxima are smaller than the zero field data. The former aspect results from the phase difference between spin up and spin down electrons, which enhances the net spin precession amplitude. The latter aspect is a result of spin dephasing due to a distribution in g factors. The effective spin lifetime resulting from dephasing due to a Gaussian distribution of g factors is given by [21]

$$T_{eff} = \frac{\hbar\sqrt{2}}{\Delta g \mu_B B}. \tag{2.25}$$

With a final spin polarization after recombination of $2.0 \cdot 10^{16}$ cm^{-3}, this means that the net spin precession occurs within a carrier energy width of ≈ 4.2 meV. This energy width corresponds to a Δg of 0.026. Using this Δg as a measure of the width of a Gaussian distribution, Eq. 2.25 yields a spin dephasing time of $T_{eff} = 0.6$ ns, which is of the same order as the decrease of the precession amplitude observed in Fig. 2.9b.

These results show that spin precession in the moderate to high fluence regime can result in a time-dependent precession frequency due to an energy dependence of the electron g factor. Also, a relative large energy window of spin polarized electrons after recombination strongly increases the dephasing of electron spins, thereby reducing the effective spin lifetime.

Bibliography

[1] L. Landau and E. Lifshitz, *On the theory of the dispersion of magnetic permeability in ferromagnetic bodies*, Phys. Z. Sowjetunion **8**, 153 (1953). 2.1

[2] T. L. Gilbert, *A Lagrangian formulation of the gyromagnetic equation of the magnetic field*, Phys. Rev. **100**, 1243 (1955). 2.1

[3] T. L. Gilbert, *A phenomenological theory of damping in ferromagnetic metals*, IEEE Trans. Magn. **40**, 3443-3449 (2004). 2.1, 2.1

[4] B. A. Kalinikos, and A. N. Slavin, *Theory of dipole-exchange spin wave spectrum for ferromagnetic films with mixed exchange boundary conditions*, J. Phys. C: Solid State Phys. **19**, 7013-7033 (1986) 2.1

[5] R. W. Damon, J. R. Eshbach, *Magnetostatic modes of a ferromagnet slab*, J. Phys. Chem. Solids **19**, 308-320 (1961). 2.1

[6] S. O. Demokritov, *Dynamic eigen-modes in magnetic stripes and dots*, J. Phys.: Condens. Matter **15**,S2575-S2598 (2003). 2.1

[7] C. Mathieu, J. Jorzick, A. Frank, S. O. Demokritov, B. Hillebrands, B. Bartenlian, C. Chappert, D. Decanini, F. Rousseaux, and E. Cambril, *Lateral Quantization of Spin Waves in Micron Size Magnetic Wires*, Phys. Rev. Lett. **81** 3968-3971 (1998). 2.1

[8] J. Jorzick, S. O. Demokritov, B. Hillebrands, M. Bailleul, C. Fermon, K. Y. Guslienko, A. N. Slavin, D. V. Berkov, and N. L. Gorn, *Spin Wave Wells in Nonellipsoidal Micrometer Size Magnetic Elements*, Phys. Rev. Lett. **88**, 047204 (2002). 2.1

[9] J. P. Park, P. Eames, D. M. Engebretson, J. Berezovksy, and P. A. Crowell, *Spatially Resolved Dynamics of Localized Spin-Wave Modes in Ferromagnetic Wires*, Phys. Rev. Lett. **89**, 277201 (2002). 2.1

[10] *Optical Orientation* (Modern Problems in Condensed Matter Sciences, Vol. 8), edited by F. Meier, and B. P. Zachachrenya (North-Holland, Amsterdam, 1984). 2.2, 2.3

[11] M. R. Brozel, and G. E. Stillman, *Properties of Gallium Arsenide* (3rd Edition), (London: INSPEC, 1996). 2.2

[12] P. H. Song, and K. W. Kim, *Spin relaxation of conduction electrons in bulk III-V semiconductors*, Phys. Rev. B **66**, 035207 (2002). 2.3

[13] R. J. Elliott, *Theory of the effect of spin-orbit coupling on magnetic resonance in some semiconductors*, Phys. Rev. **96**, 266-279 (1954). 2.3

[14] Y. Yafet, in *Solid State Physics*, Vol. 14, edited by F. Seitz and D. Turnbull (Academic, New York, 1963), p. 2. 2.3

[15] J.-N. Chazalviel, *Spin relaxation of conduction electrons in n-type indium antimonide at low temperature*, Phys. Rev. B **11**, 1555-1562 (1975). 2.3

[16] A. G. Aronov, G. E. Pikus, and A. N. Titkov, *Spin relaxation of conduction electrons in p-type III-V compounds*, Zh. Eksp. Teor. Fiz. **84**, 1170-1184 (1983) [Sov. Phys. JETP **57**, 680-687 (1983)]. 2.3, 2.3, 2.3

[17] M. I. D'yakonov, and V. I. Perel', *Spin orientation of electrons associated with the interband absorption of light in semiconductors*, Zh. Eksp. Teor. Fiz. **60**, 1954-1965 (1971) [Sov. Phys. JETP **33**, 1053-1059 (1971)]. 2.3

[18] R. I. Dzhioev, K. V. Kavokin, V. L. Korenev, M. V. Lazarev, B. Y. Meltser, M. N. Stepanova, B. P. Zakharchenya, D. Gammon, and D. S. Katzer, *Low-temperature spin relaxation in n-type GaAs*, Phys. Rev. B **66**, 245204 (2002). 2.3, 2.4, 2.4, 2.4

[19] G. L. Bir, A. G. Aronov, and G. E. Pikus, *Spin relaxation of electrons due to scattering by holes*, Zh. Eksp. Teor. Fiz. **69**, 1382-1397 (1975) [Sov. Phys. JETP **42**, 705-712 (1976)]. 2.3

[20] K. Zerrouati, F. Fabre, G. Bacquet, J. B. J. Frandon, G. Lampel, and D. Paget, *Spin-lattice relaxation in p-type gallium arsenide single crystals*, Phys. Rev. B **37**, 1334-1341 (1988). 2.3

[21] J. M. Kikkawa, and D. D. Awschalom, *Resonant spin amplification in n-type GaAs*, Phys. Rev. Lett. **80**, 4313- 4316 (1998). 2.4, 2.5

[22] M. A. Hopkins, R. J. Nicholas, P. Pfeffer, W. Zawadzki, D. Gauthier, J. C. Portal, and M. A. DiForte-Poisson, *A study of the conduction band non-parobolicity, anisotropy, and spin splitting in GaAs and InP*, Semicond. Sci. Technol. **2**, 568 (1987). 2.5

[23] H. Mayer, and U. Rössler, *Spin splitting and anisotropy of cyclotron resonance in the conduction band of GaAs*, Phys. Rev. B **44**, 9048 (1991).

[24] M. Oestreich, S. Hallstein, A. P. Heberle, K. Eberl, E. Bauser, and W. W. Rühle, *Temperature and density dependence of the electron Landé g factor in semiconductors*, Phys. Rev. B **53**, 7911 (1996). 2.5

Chapter 3

Magneto-optical techniques

This Chapter discusses the experimental tools, which are used throughout this Thesis to study magnetization and spin dynamics in spintronic devices and semiconductor nanostructures. These experimental tools all employ magneto-optical techniques and are referred to as: Magneto-optical Kerr-effect (MOKE), Time-resolved magneto-optical Kerr-effect (TR-MOKE) and Time-resolved magnetization modulation spectroscopy (TiMMS). This Chapter discusses in detail the magneto-optical techniques, and the experimental implementation. Also, unpublished experimental results obtained with these techniques will be presented in order to demonstrate the power of these techniques. Finally, this Chapter contains simulation results which facilitate the interpretation of data obtained on complicated multilayer systems.[1]

[1]Part of Section 1.5 of this Chapter is published as G. Malinowski, F. Dalla Longa, J. H. H. Rietjens, P. V. Paluskar, R. Huijink, H. J. M Swagten, and B. Koopmans, *Control of speed and efficiency of ultrafast demagnetization by direct transfer of spin angular momentum*, Nat. Phys. **4**, 855 (2008).

3.1 MOKE

In this Thesis, most experimental techniques used to probe magnetism and spin related processes rely on the magneto-optical Kerr-effect (MOKE). This effect is used to determine static magnetic properties of magnetic multilayers, such as coercivity, remanence, and switching behavior. Also, time-resolved techniques such as TR-MOKE and TiMMS, to be discussed in following sections, probe the dynamic behavior of the magnetization, and an optically induced spin distribution respectively, via MOKE. In this Section, we will give a basic description of MOKE, present an experimental setup for measuring static magnetic properties, and discuss an illustrative example. Also, we will outline a procedure for calculating the MOKE originating from an arbitrary system of magnetic multilayers, and present an important application of this procedure.

3.1.1 Basics of MOKE

The basis of the Kerr-effect is a change in polarization state of incident light upon reflection from a medium with an unequal population of spin up and spin down electrons, such as a ferromagnetic material or a semiconductor with a non-equilibrium spin distribution. Microscopically, the Kerr-effect results from spin-orbit coupling, the coupling of spin angular momentum with the orbital angular momentum. The dipole selection rules are governed by the orbital angular momentum. Spin-orbit coupling induces a correlation between the orbital and spin angular momenta, which allows one to optically probe the spin system via the dipole selection rules. However, because the orbital momentum in 3d transition metals is largely quenched by crystal field effects, the Kerr-effect is generally small. For a detailed theoretical description, the reader is referred to Ref. [1].

In a phenomenological picture, the response of a medium to an incident electromagnetic wave is given by the dielectric tensor $\vec{\vec{\epsilon}}$, via $\vec{D} = \vec{\vec{\epsilon}}\vec{E}$. Here, $\vec{E}$ is the electric field, and $\vec{D}$ is the electric displacement. In general, for an isotropic medium it follows from symmetry arguments that the non-diagonal elements ϵ_{ij} vanish, and the diagonal elements ϵ_{ii} are equal, so that $\vec{\vec{\epsilon}}$ reduces to a scaler. However, in anisotropic media the non-diagonal elements of $\vec{\vec{\epsilon}}$ do not necessarily vanish. In the special case of an isotropic medium with a finite magnetization $\vec{M} = (m_x, m_y, m_z)$, $\vec{\vec{\epsilon}}$ is given by

$$\vec{\vec{\epsilon}} = \begin{pmatrix} \epsilon_{xx} & \epsilon_{xy}(m_z) & \epsilon_{xz}(m_y) \\ -\epsilon_{xy}(m_z) & \epsilon_{xx} & \epsilon_{yz}(m_x) \\ -\epsilon_{xz}(m_y) & -\epsilon_{yz}(m_x) & \epsilon_{xx} \end{pmatrix}. \tag{3.1}$$

To first order, the diagonal elements are independent of $\vec{M}$, and the off-diagonal elements ϵ_{ij} depend linearly on $\vec{M}$ in the direction $\hat{i} \times \hat{j}$. Also, $\epsilon_{ij}(\vec{M}) = -\epsilon_{ij}(-\vec{M})$. The off-diagonal elements ϵ_{ij} are sometimes expressed as $\epsilon_{ij} = \imath Q m_{\hat{i}\times\hat{j}} \cdot \epsilon_{xx}$, with $Q = \imath\epsilon_{xy}/\epsilon_{xx}$ the magneto-optical Voigt parameter, or simply the magneto-optical

constant. Q is a complex parameter, and is a measure for the magnitude of the Kerr-effect. When $\vec{M} = (0, 0, m_z)$, Eq. 3.1 can be diagonalized by changing to cylindrical coordinates (i.e. $\hat{c}_- = 1/\sqrt{2}(\hat{x} - \imath\hat{y})$, $\hat{c}_+ = 1/\sqrt{2}(\hat{x} + \imath\hat{y})$, and $\hat{c}_z = \hat{z}$) obtaining

$$\vec{\vec{\epsilon}} = \begin{pmatrix} \epsilon_{xx} - \imath\epsilon_{xy}(m_z) & 0 & 0 \\ 0 & \epsilon_{xx} + \imath\epsilon_{xy}(m_z) & 0 \\ 0 & 0 & \epsilon_{xx} \end{pmatrix}. \tag{3.2}$$

From this, we see that the eigenmodes of propagating electromagnetic waves in magnetic media are left- and right-circularly polarized light, and that their corresponding dielectric (complex) tensor elements ϵ_{--} and ϵ_{++} (and thereby their complex indices of refraction, n_- and n_+) are different. A linearly polarized wave, which can be viewed as the sum of left- and right-circularly polarized waves, will thus experience a change in polarization state after reflection from a magnetic medium. This change manifests itself in a rotation of the polarization axis, and an increase in ellipticity, and is schematically shown in Fig. 3.1a. The complex Kerr-rotation can then be defined as

$$\Theta_K = \theta_K + \imath\varepsilon_K = \frac{r_+ - r_-}{1/2(r_+ + r_-)}, \tag{3.3}$$

with r_+ and r_- the reflection coefficients for left- and right circularly polarized light. For the case of normal incidence, Eq. 3.3 can be expressed in terms of the dielectric tensor elements as

$$\Theta_K = \frac{2(n_+ - n_-)}{(n_+ n_- - 1)} = \frac{2(\epsilon_{++} - \epsilon_{--})}{(\sqrt{\epsilon_{++}\epsilon_{--}} - 1)(\sqrt{\epsilon_{++}} + \sqrt{\epsilon_{--}})} = \frac{\imath\epsilon_{xy}}{(\epsilon_{xx} - 1)\sqrt{\epsilon_{xx}}}. \tag{3.4}$$

When using the Jones-formalism to describe the polarization state of light before and after reflection from a sample, the components of the Jones-vector represent the electric field perpendicular (s) and parallel (p) to the plane of incidence [2]. The sample is represented by a Jones-matrix of the form

$$\begin{pmatrix} r_{ss} & r_{sp} \\ r_{ps} & r_{pp} \end{pmatrix}, \tag{3.5}$$

and the complex Kerr-rotation can be expressed as $\Theta_K^s = r_{ps}/r_{ss}$ and $\Theta_K^p = r_{sp}/r_{pp}$ for the case of incident $s-$ and $p-$polarized light, respectively. We note that three types of Kerr-effect can be distinguished, depending on the relative orientation of the magnetization with respect to the plane of incidence, and the sample surface: polar, longitudinal, and transversal. The geometries of these three types are sketched in Fig. 3.1b. The magnitude of the Kerr-effect is different for each geometry, and depends on the angle of incidence of the probing light. In general, the polar geometry gives rise to the largest Kerr-effect. At angles of incidence close to 60°, the longitudinal Kerr-effect is maximal, with values close to the polar Kerr-effect at normal incidence. The transversal Kerr-effect is generally an order of magnitude smaller than the other two. We note that in this Thesis, we will employ only the polar geometry, that is, the experiments are sensitive only to out-of-plane magnetization (or to a density of spins aligned normal to the sample surface).

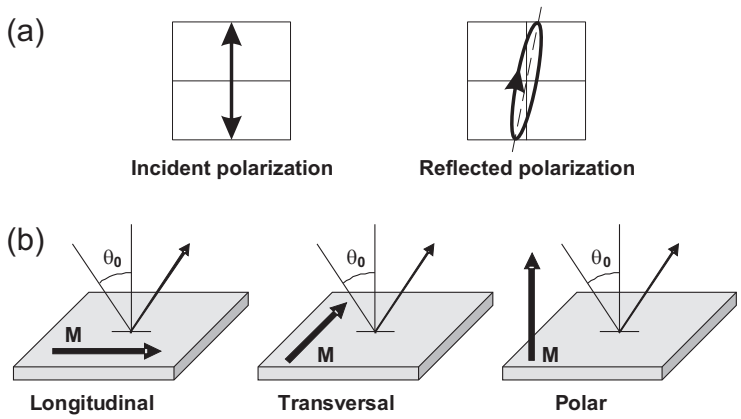

Figure 3.1: (a) Schematic illustration of the change in polarization state of linearly polarized incident light upon reflection from a magnetized surface. (b) Geometries of the three different types of Kerr-effect: longitudinal, transversal, and polar.

3.1.2 Measuring MOKE

In order to measure the magneto-optical Kerr-effect, a very polarization sensitive technique should be used. One such technique is employed in the experimental setup schematically depicted in Fig. 3.2. This setup measures the Kerr-effect as a function of an applied magnetic field. As the magnetization of the sample under investigation changes its direction due to the external magnetic field, a change in the Kerr-signal is observed. This way, hysteresis loops of the sample can be measured, from which static magnetic properties such as coercivity, remanence, and switching behavior can be extracted. In the experimental setup of Fig. 3.2, a linearly polarized laser beam passes a photo-elastic modulator (PEM), with its main axis 45° with respect to the laser polarization. The PEM retards one of the polarization components of the laser beam, thereby producing alternatingly left- and right-circularly polarized light at a frequency of $f = 50$ kHz. The reflected laser beam from the sample passes a second polarizer and is focused on a Si-photodiode. Due to the polarization modulation by the PEM, the intensity on the detector contains components both at $1f$ (50 kHz) and $2f$ (100 kHz). It can be shown that these components are given by [3]

$$\frac{V_{1f}}{V_{dc}} = 4J_1(A)\varepsilon_K \tag{3.6}$$

$$\frac{V_{2f}}{V_{dc}} = 4J_2(A)\theta_K \tag{3.7}$$

with J_n the n^{th} Bessel-function of the first kind, and A the maximum retardation setting of the PEM, which can be chosen to maximize $J_n(A)$. Thus, by setting

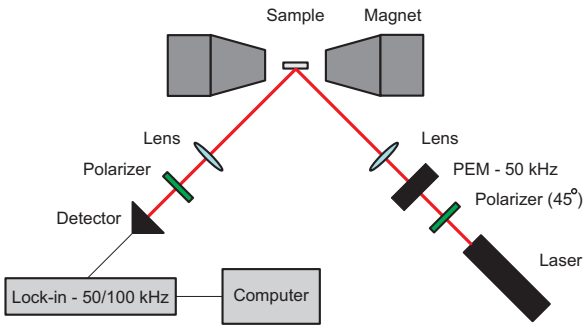

Figure 3.2: Schematic picture of an experimental setup that measures the MOKE in the longitudinal configuration, which is used to measure static magnetic properties of magnetic multilayers.

the reference frequency of the lock-in amplifier either to $1f$ or $2f$, either the Kerr-ellipticity or the Kerr-rotation can be measured, respectively.

3.1.3 An example: the AlOx / CoFeB / Pd system

As an example of a MOKE measurement let us consider the AlOx / FM / Pd system, which is of interest because of its potential application as perpendicularly magnetized electrodes for electrical spin injection into semiconductors [4–6]. As we have seen in the Introduction, electrical spin injection into semiconductors can be achieved by using an oxidic tunnel barrier in combination with a ferromagnetic electrode [7]. The advantage of using electrodes with perpendicular magnetic anisotropy, in contrast to conventional electrodes with in-plane magnetic anisotropy, is that these electrodes enable optical spin detection without application of a (strong) external magnetic field. When using a LED system for spin detection, the orientation of the spins are inherently aligned normal to the sample surface, and the degree of circular polarization of the emitted light can be directly measured. When using MOKE for spin detection, a polar configuration with maximum sensitivity can be applied, also enabling lateral detection of spin transport. Co / Pd multilayers (as well as Co / Pt multilayers) are known to exhibit perpendicular magnetic anisotropy [8–10], when the individual layers are thin enough, such that the (perpendicular) surface anisotropy is larger than the (in-plane) volume anisotropy [11].

We have studied the AlOx / $Co_{60}Fe_{20}B_{20}$ / Pd system, since $Co_{60}Fe_{20}B_{20}$ layers are known to grow amorphous with a low coercive field [12]. Figure 3.3a shows the particular sample which has been studied by MOKE in the polar geometry. By using a wedge of $Co_{60}Fe_{20}B_{20}$, and scanning the laser spot of the MOKE-setup along the sample, we can study the dependence of the magnetic properties of this system on the thickness of the $Co_{60}Fe_{20}B_{20}$-layer, d_{FM}.

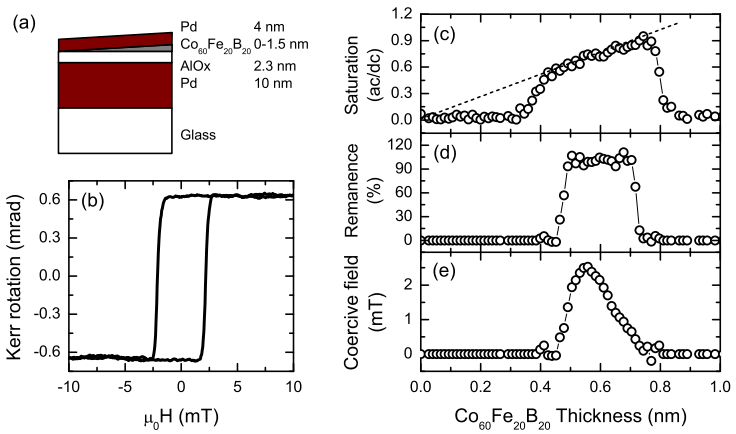

Figure 3.3: MOKE measurements on a wedge-sample consisting of Pd (100 nm) / AlOx (2.3 nm) / $Co_{60}Fe_{20}B_{20}$ (0-1.5 nm) / Pd (4 nm). (a) Schematic layout of the multilayer. (b) MOKE hysteresis curve measured at a $Co_{60}Fe_{20}B_{20}$-thickness of 0.6 nm. (c-e) Saturation, remanence, and coercive field as a function of $Co_{60}Fe_{20}B_{20}$-thickness.

A typical MOKE measurement at $d_{FM} = 0.6$ nm is shown in Fig. 3.3b. A clear rectangular hysteresis loop is observed, indicating that at this thickness the $Co_{60}Fe_{20}B_{20}$ has a perpendicular magnetic anisotropy, with near 100% remanence, and a low coercive field of 2 mT. Figures 3.3c, d, and e show the amplitude of the MOKE-signal at saturation, the remanence, and the coercive field as a function of d_{FM}. We observe that the amplitude of the MOKE-signal starts to increase from zero at $d_{FM} = 0.3$ nm. This implies that the deposited $Co_{60}Fe_{20}B_{20}$ is not ferromagnetic below a thickness of 0.3 nm, possibly due to island growth of $Co_{60}Fe_{20}B_{20}$ on the AlOx. Between 0.4 and 0.75 nm, the MOKE signal increases linearly with d_{FM}. The linear trend can be extrapolated to zero signal at zero thickness, as indicated in Fig. 3.3c. This shows that between 0.4 and 0.75 nm, the saturation signal is a direct measure of the amount of ferromagnetic material, and that the $Co_{60}Fe_{20}B_{20}$-layer is fully ferromagnetic in this region. The linear trend results from the very low d_{FM}, compared to the penetration depth of the laser light. In this regime the Kerr-effect is linearly proportional to the magnetization. For 0.5 nm $< d_{FM} <$ 0.7 nm, the $Co_{60}Fe_{20}B_{20}$ has a perpendicular magnetic anisotropy with near 100% remanence, and a maximum coercive field of 2.5 mT.

This example shows that MOKE enables systematic studies of magnetic properties as a function of layer thicknesses, and that perpendicularly magnetized electrodes can be grown on AlOx, with various coercive fields.

3.1.4 MOKE in a general multilayer system

In the previous example we have seen that the Kerr-effect was linearly proportional to the total magnetization of the system, as a result of the very thin layers used. In the case of thicker layers or multilayer systems, however, this linear proportionality is no longer valid. In general, the magnitude of the Kerr-effect depends on the wavelength, angle of incidence, and initial polarization of the light wave, and on the direction of the magnetization with respect to the plane of incidence. Also, it is dependent on the complex refractive index, and complex magneto-optical constants of each layer. In case of a multilayer system with magnetic and non-magnetic layers, also multiple internal reflections of the light wave have to be taken into account. A useful approach for tackling the general problem of an arbitrary magnetic multilayer is given by Zak *et al.* [13, 14]. This approach is based on the so-called medium boundary matrix **A**, and medium propagation matrix **D**, which we shall briefly explain here.

The boundary matrix **A** facilitates the problem of fulfilling the boundary conditions of the electromagnetic field at each interface. Consider two media separated by the $\hat{x} - \hat{y}$ plane as shown in Fig. 3.4. An electro-magnetic wave $\vec{E}_1^{(i)}$ is incident on medium 1 at an angle θ with the $\hat{z}$ axis, and has components $E_{1s}^{(i)}$ (perpendicular) and $E_{1p}^{(i)}$ (parallel) to the plane of incidence. Part of the wave is reflected at the interface, denoted by $\vec{E}_1^{(r)}$, and a part is transmitted, denoted by $\vec{E}_2^{(i)}$. At the boundary ($z = 0$), the components of the electric field, $\vec{E}$, and magnetic field, $\vec{H}$, parallel to the boundary are continuous. Defining the vector $\vec{F}_m$ for medium m as

$$\vec{F}_m = \begin{pmatrix} E_{m,x} \\ E_{m,y} \\ H_{m,x} \\ H_{m,y} \end{pmatrix}, \tag{3.8}$$

the boundary conditions can be expressed as $\vec{F}_1 = \vec{F}_2$. In order to express the boundary conditions in terms of the electro-magnetic wave components E_m^n, the vector $\vec{P}$ is defined as

$$\vec{P}_m = \begin{pmatrix} E_{m,s}^{(i)} \\ E_{m,p}^{(i)} \\ E_{m,s}^{(r)} \\ E_{m,p}^{(r)} \end{pmatrix}. \tag{3.9}$$

The medium boundary matrix **A** connects $\vec{F}$ to $\vec{P}$ via $\vec{F} = \mathbf{A}\vec{P}$, and the boundary conditions can be expressed as

$$\mathbf{A}_1\vec{P}_1 = \mathbf{A}_2\vec{P}_2. \tag{3.10}$$

This is a set of four linear equations with the unknowns $E_{1s}^{(r)}$, $E_{1p}^{(r)}$, $E_{2s}^{(i)}$, and $E_{2p}^{(i)}$, which can be solved once the medium boundary matrix **A** is known. In case of

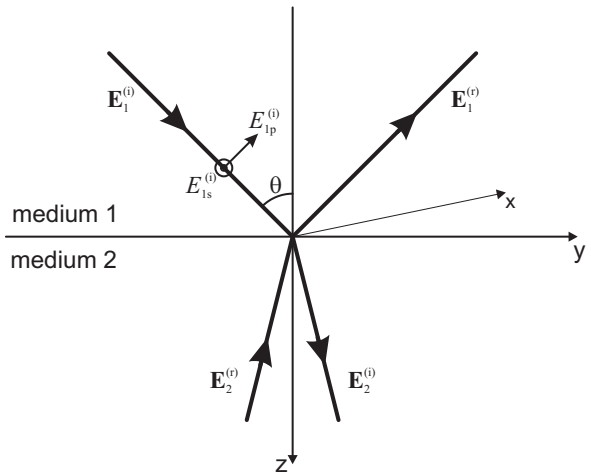

Figure 3.4: Two media separated by the $\hat{x} - \hat{y}$ plane. Light is incident (i) from medium 1, and at the interface between medium 1 and 2 it is partly reflected (r) back to medium 1, and partly transmitted to medium 2. The angle of incidence is θ, E_s and E_p are the electric field components perpendicular (s), and parallel (p), to the plane of incidence ($\hat{y}-\hat{z}$ plane).

more than one boundary (as in multilayers systems) the propagation of the electromagnetic wave inside the medium has to be taken into account. This propagation is expressed by the medium propagation matrix $\mathbf{D}_m$. It connects $\vec{P}_m^t$ at the top interface to $\vec{P}_m^b$ at the bottom interface via

$$\vec{P}_m^t = \mathbf{D}_m(d)\vec{P}_m^b, \tag{3.11}$$

with d the thickness of medium m. Using the matrices $\mathbf{A}_m$ and $\mathbf{D}_m$, we can now relate the vector $\vec{P}_i$ of the initial medium to the vector $\vec{P}_f$ of the final medium by repeatedly using Eqs. 3.10 and 3.11:

$$\begin{aligned} \vec{P}_i &= \mathbf{A}_i^{-1}\mathbf{A}_2\vec{P}_2^t = \mathbf{A}_i^{-1}\mathbf{A}_2\mathbf{D}_2\vec{P}_2^b = \mathbf{A}_i^{-1}(\mathbf{A}_2\mathbf{D}_2\mathbf{A}_2^{-1})\mathbf{A}_3\vec{P}_3^t \\ &= \mathbf{A}_i^{-1}\prod_{m=1}^{l}(\mathbf{A}_m\mathbf{D}_m\mathbf{A}_m^{-1})\mathbf{A}_f\vec{P}_f = \mathbf{M}\vec{P}_f. \end{aligned} \tag{3.12}$$

Here, the matrix $\mathbf{M}$ can be viewed as the full reflection-transmission matrix of the problem. In order to calculate $\mathbf{M}$ and solve Eq. 3.12, the matrices $\mathbf{A}_m$ and $\mathbf{D}_m$ need to be calculated for every layer. Analytical expressions exist for these matrices for arbitrary direction of the magnetization. However, we will not write down the full form here, and refer the interested reader to the papers of Zak *et al.* [13, 14]. We note that $\mathbf{A}_m$ and $\mathbf{D}_m$ depend on the photon energy, the angle of incidence on layer m, and on layer specific parameters, such as the orientation of the magnetization, the

thickness d_m, the complex refractive index N_m, and the so-called magneto-optical Voigt parameter Q_m. This (complex) parameter is a measure of the strength of the Kerr-effect and is related to the element of the dielectric tensor via $Q = -\imath\epsilon_{xy}/\epsilon_{xx}$. N and Q are generally dependent on the photon energy. If all these parameters are known for each layer of the system of interest, the matrix $\mathbf{M}$ can be calculated for arbitrary angle of incidence. Since there is no light incident from the bottom, $E_{f,s}^{(r)} = E_{f,p}^{(r)} = 0$, and Eq. 3.12 can be written as

$$\begin{pmatrix} E_{i,s}^{(i)} \\ E_{i,p}^{(i)} \\ E_{i,s}^{(r)} \\ E_{i,p}^{(r)} \end{pmatrix} = \begin{pmatrix} \mathbf{G} & \mathbf{H} \\ \mathbf{I} & \mathbf{J} \end{pmatrix} \begin{pmatrix} E_{f,s}^{(i)} \\ E_{f,p}^{(i)} \\ 0 \\ 0 \end{pmatrix}. \tag{3.13}$$

From this equation it follows that

$$\begin{pmatrix} E_{i,s}^{(r)} \\ E_{i,p}^{(r)} \end{pmatrix} = \mathbf{IG}^{-1} \begin{pmatrix} E_{i,s}^{(i)} \\ E_{i,p}^{(i)} \end{pmatrix} = \begin{pmatrix} r_{ss} & r_{sp} \\ r_{ps} & r_{pp} \end{pmatrix} \begin{pmatrix} E_{i,s}^{(i)} \\ E_{i,p}^{(i)} \end{pmatrix}. \tag{3.14}$$

and we see that $\mathbf{IG}^{-1}$ is the reflection matrix from which the complex Kerr-rotation can be obtained as stated in Section 3.1.3. A computer code has been written to perform all the necessary calculations in order to extract the complex Kerr-rotation for an arbitrary multilayer.

Although the effect of absorption is included in the matrices $\mathbf{A}$, and $\mathbf{D}$, the absorption profile is not part of the program output. The absorption profile is, however, of interest in many systems, and can be calculated in the following way, employing the so-called transfer matrix approach [15]. Assuming normal incidence of the light, the Fresnel coefficients at each interface i are given by

$$r_i = \frac{N_{i-1} - N_i}{N_{i-1} - N_i}, \qquad \text{and} \qquad t_i = \frac{2N_{i-1}}{N_{i-1} - N_i}, \tag{3.15}$$

with r_i the reflection coefficient, t_i the transmission coefficient, and N_i the (complex) refractive index of the layer i. With these coefficients, the electric field at each interface can be calculated for an arbitrary multilayer using the transfer matrix. The transfer matrix links the electric field (propagating in the direction parallel (+), and anti-parallel (−) to the normal of the multilayer) at interface $i-1$ to the one at interface i, and takes the following form:

$$\begin{pmatrix} E_{i-1}^{(+)} \\ E_{i-1}^{(-)} \end{pmatrix} = \frac{1}{t_i} \begin{pmatrix} \exp(-\imath\delta_{i-1}) & \exp(-\imath\delta_{i-1}) \\ r_i \exp(\imath\delta_{i-1}) & \exp(\imath\delta_{i-1}) \end{pmatrix} \begin{pmatrix} E_i^{(+)} \\ E_i^{(-)} \end{pmatrix}. \tag{3.16}$$

Here, $\delta_i = 2\pi d_i N_i/\lambda$ is the phase-shift upon traversing layer i, with d_i the thickness of layer i, and λ the wavelength of the light. Next, using the same transfer matrix, the total electric and magnetic field at each depth z within the multilayer

is evaluated, from which the Poynting vector ($S = E^*H \propto E^2$) can be obtained. Finally, differentiating the Poynting vector with respect to z gives the absorption profile $A(z)$.

As an example of the application of the above theory to a physical system, we will present an important case study regarding Co/Pt multilayers in the next section.

3.1.5 A case study: Co/Pt multilayers

Co/Pt multilayers are a useful system from magnetic point of view, since these multilayers exhibit out-of-plane magnetization [10], as we have seen in Section 3.1.2. More importantly, a system consisting of two blocks of Co/Pt multilayers, separated by a non-magnetic spacer, can be used to study spin angular momentum transfer between these two multilayer blocks on a sub-picosecond time-scale by performing laser-induced demagnetization experiments [3]. Here, we will not discuss the details of the experiment, and refer the interested reader to Ref. [16]. However, as in these experiments the absorption of a laser pulse is used to heat the system, and MOKE is used to study the demagnetization of both multilayer blocks, it is important to know how much of the laser light is absorbed in each block, and what information of each block is contained in the Kerr-rotation or Kerr-ellipticity. Therefore, we have applied the methods of the previous section in order to calculate the absorption profile of the system, and the complex Kerr-rotation and -ellipticity in the polar geometry.

Before doing so, we like to point out that for very thin layers, the absorption should scale the same way as the Kerr-effect with increasing depth z in the multilayer. Due to a finite complex part of the refractive index, k (also called extinction coefficient), the amplitude of the electromagnetic (EM) wave will decrease as $\exp(-2\pi kz/\lambda)$ while propagating in the medium in the direction z. The Kerr-effect is proportional to the electric field, and in order to measure the Kerr-effect, the light has to travel backwards through the medium. The magnitude of the Kerr-effect originating from depth z scales thus as $\exp(-4\pi kz/\lambda)$. The absorption is proportional the intensity of the EM wave (thus to the electric field squared), and decreases also as $\exp(-4\pi kz/\lambda)$ with increasing z. The absorption thus scales the same way as the Kerr-effect, and therefore one expects that the ratio of absorption in the top and bottom blocks is equal to the ratio of the Kerr-effect in the top and bottom blocks.

Let us now turn to the actual calculation. We consider the following system: 10 Pt / [0.4 Co / 0.7 Pt]$_4$ / 0.4 Co / t S / 0.4 Co / [0.7 Pt / 0.4 Co]$_4$ / 2 Pt (units in nanometer), with S being either Ru or NiO of thickness t. First, we focus on the absorption profile, and the ratio of total absorption in each Co/Pt-block. In order to calculate the absorption profile of these samples, we used the transfer matrix approach as explained in the previous Section. We used literature values for the complex refractive indices N of each layer: N_{Pt}, N_{Ru}, and N_{Si} are taken from [17], N_{SiOx} is taken from [18]. The CoPt multilayer is treated as a single entity with the

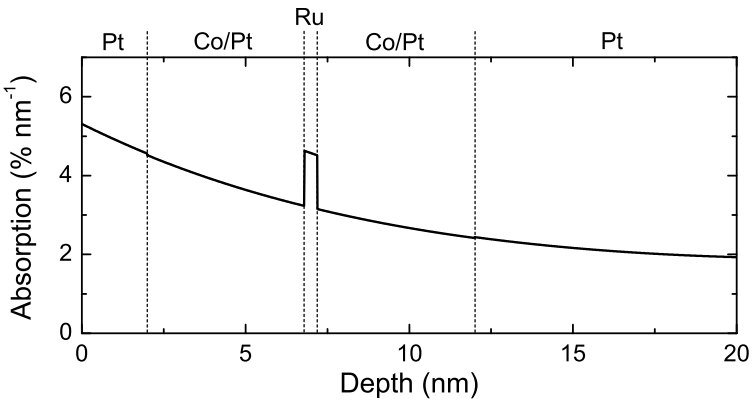

Figure 3.5: Calculated absorption profile for a sample composition of SiOx 3 / Pt 10 / CoPt 4.8 / Ru 0.4 / CoPt 4.8 / Pt 2 (units in nanometer). Absorption is calculated as a fraction of the transmitted light through the top interface, and with a wavelength of $\lambda = 785.0$ nm.

complex refractive index taken from [19].

The absorption profile of the Co/Pt-system is shown in Fig. 3.5, for the case with S = Ru, t = 0.4 nm, and $\lambda = 785.0$ nm, which is the laser wavelength used in the experiment. The much larger absorption coefficient of Ru with respect to both Pt and CoPt clearly shows up in Fig. 3.5. Integrating the absorption-profile for the two CoPt-blocks, yields the total absorption in each CoPt-block (A^{Ru}_{top}, and A^{Ru}_{bottom}). From Fig. 3.5 we find that the ratio of the absorption in the top and bottom CoPt-block is $A^{Ru}_{top}/A^{Ru}_{bottom} = 1.39$ ($A^{Ru}_{top} = 58.2\%$ and $A^{Ru}_{bottom} = 41.8\%$).

The calculation of the Kerr-rotation and -ellipticity originating from each of the two CoPt-blocks is performed using the model of Zak *et al.* [14], as explained in the previous Section. By artificially setting the magneto-optic Voigt parameter for one of the two CoPt-blocks (obtained from ref. [19]) to zero, we can calculate the Kerr-effect for each block separately. We have performed the calculation for both a Ru as well as a NiO spacer, for various spacer thicknesses, and with $\lambda = 785.0$ nm. Figure 3.6 shows the result of this calculation. We will refer to the Kerr-rotation (ellipticity) originating from the top Co/Pt-block with NiO spacer as θ^{NiO}_{top} (ε^{NiO}_{top}), and use a similar notation for the bottom Co/Pt-block and Ru spacer. Let us first focus on the Kerr-rotation data. For both NiO and Ru spacers, we see that θ_{top} is larger than θ_{bottom}. For the NiO spacer, θ^{NiO}_{top} increases slowly with increasing thickness, most likely due to multiple reflections between the two Co/Pt-blocks, which contributions to the total Kerr-rotation increase with increasing spacer thickness. θ^{NiO}_{bottom} remains fairly constant, because of the transparency of the NiO spacer. For the Ru spacer, the situation is different. θ^{Ru}_{top} remains fairly constant is this case, which can be explained by the strong attenuation of the multiple reflections between the Co/Pt-

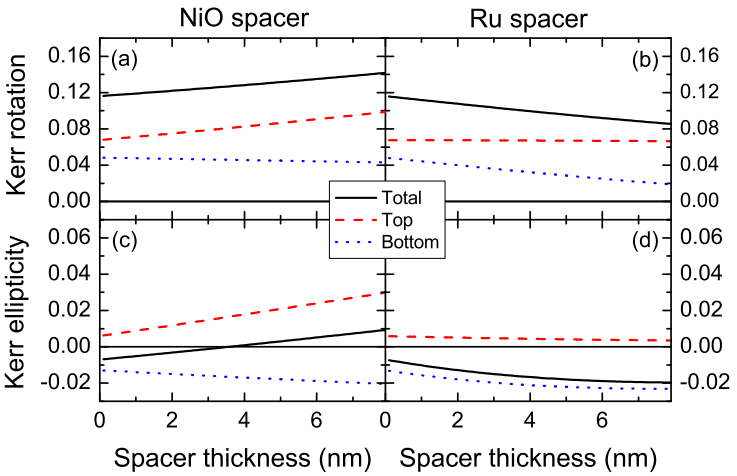

Figure 3.6: The Kerr-rotation and Kerr-ellipticity originating from a SiOx 3/ Pt 10/ CoPt 4.8/ Ru 0.4/ CoPt 4.8/ Pt 2 (units in nanometer) multilayer system, as a function of the thickness of both a NiO-spacer, and a Ru-spacer. Also the separate contributions from the top and bottom CoPt layer are shown.

blocks due to the high absorption coefficient of Ru. The strong absorption in the Ru spacer also results in a strongly decreasing θ_{bottom}^{Ru} with increasing spacer thickness. For the small spacer thicknesses used in the actual demagnetization experiment (i.e. $d_{Ru} = 0.4$ nm), the ratios A_{top}/A_{bottom}, and $\theta_{top}/\theta_{top}$, are indeed equal within a few percent, confirming the validity of our previous statement.

However, the ellipticity data shows that this statement is not generally applicable. In contrast to the Kerr-rotation, ε_{bottom} is larger than ε_{top} for a wide range of NiO- and Ru-spacer thicknesses. Also, ε_{top} is of opposite sign than ε_{bottom}, leading even to zero total ellipticity signal at a NiO-spacer of 3.6 nm. Clearly, in these cases the ratio $\varepsilon_{top}/\varepsilon_{top}$ is very different from A_{top}/A_{bottom}.

For comparison, we plot in Fig. 3.7 the ratios A_{top}/A_{bottom}, $\theta_{top}/\theta_{top}$, and $\varepsilon_{top}/\varepsilon_{top}$, all as a function of the spacer thickness. We see that for spacer thicknesses below 2 nm, within 5% the absorption ratio and Kerr-rotation ratio between the top and bottom Co/Pt-blocks are identical. For larger thicknesses, especially with a Ru spacer, large deviations occur. The ellipticity ratio is over the full range of opposite sign compared to the absorption ratio, indicating the opposite sign of the Kerr-ellipticity signal originating from top and bottom blocks. The magnitude of the Kerr-ellipticity ratio is over the full range less than half of the absorption ratio. Both observations indicate that one has to take care when interpreting the Kerr-ellipticity data for this particular system.

We conclude this case study with the remark that the procedure outlined above

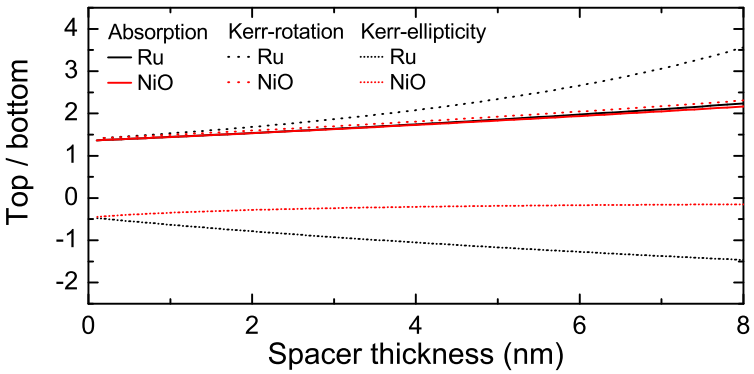

Figure 3.7: Comparison between the ratio of the absorption in the top and bottom Co/Pt multilayers blocks, and the ratio of their Kerr-rotation and Kerr-ellipticity signal.

gives useful information about the Kerr-effect and absorption in any (complicated) metallic multilayer, and also that it can be extended to semiconductor heterostructures, as we will show in Section 3.4.

3.2 TR-MOKE

The Time-Resolved Magneto-Optical Kerr-Effect (TR-MOKE) [3, 20] technique is used in Chapter 4 of this Thesis to study magnetic field pulse induced precessional magnetization dynamics in a ferromagnetic element. It is a stroboscopic measurement technique in which a current-induced magnetic field pulse acts as a pump, and a short laser pulse is used to detect the response of a magnetic system to this pump pulse via MOKE. Each reflected laser pulse thus gives information on the magnetization state at the momentary time delay between the arrival at the sample of the pump pulse and probe laser pulse.

The experimental setup for this measurement scheme is shown schematically in Fig. 3.8. A commercial AVTECH AVN-1-C-P electronic pulse generator is used as a pump to excite precessional magnetization dynamics in a micron sized ferromagnetic element. Voltage pulses (rise time $\approx$ 200 ps, duration $\approx$ 600 ps) are applied to a current line on which the ferromagnetic element is deposited. The resulting current pulses induce an in-plane magnetic field pulse at the sample, triggering a precessional motion via the Landau-Lifshitz-Gilbert-equation, introduced in Section 2.1.

A commercial Spectra-Physics pulsed laser system is used as a probe. It consists of solid state laser diodes, a Millennia unit, and a Tsunami unit. The two solid state continuous wave (cw) laser diodes (λ = 809 nm) pump a Nd:YVO_4 crystal in the Millennia unit, which emits at a wavelength of λ = 1064 nm. A non-linear

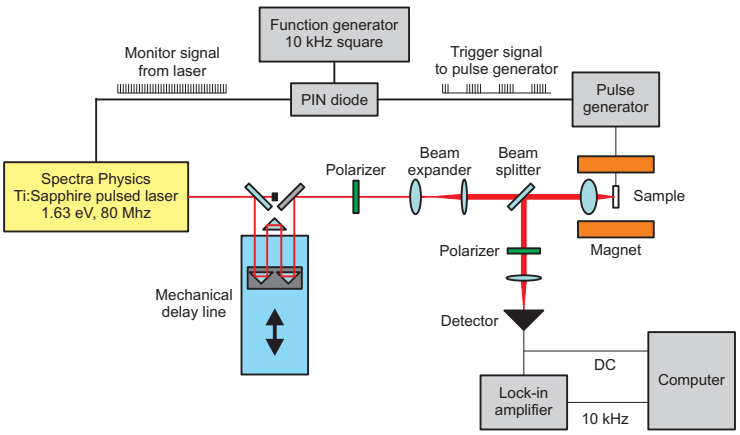

Figure 3.8: Schematic picture of the TR-MOKE setup, which is used to detect optically the magnetization dynamics induced by short magnetic field pulses.

crystal (LBO) converts the Nd:YVO_4-emission via second harmonic generation to a cw laser output ($\lambda = 532$ nm) of up tot 10 W. The Millennia output is focused on a Ti:Sapphire crystal in the Tsunami unit, which has a very broad emission spectrum, and enables laser operation at photon energies between typically 1.3 and 1.72 eV (720-950 nm). In order to produce a pulsed laser output, the phases of all longitudinal laser modes must be locked. This leads to constructive interference at one point in the laser cavity, and destructive interference at all other points, thereby creating a single circulating pulse in the cavity. This so-called mode-locking is achieved in the Tsunami-cavity, and the repetition rate of the laser (80 MHz) is determined by the cavity length.

From the main output of the Tsunami a weak probe beam (photon energy 760 nm, average power 70 mW) is extracted with a beam splitter. In the stroboscopic measurement scheme, the pulse generator is triggered by the monitor signal from the Tsunami, such that to each magnetic field pulse corresponds exactly one laser pulse. The probe beam is directed to an optical delay line, which allows for adjusting the time delay between the arrival of the pump pulse and probe beam at the sample. It has a length of 30 cm and consists of three retro-reflectors, so that the optical path can be extended with 1.20 m, corresponding to 4 ns. This is roughly one third of the total time between two pulses (80 MHz $\equiv$ 12.5 ns). The zero delay between pump and probe can be put into the time window of the delay line by choosing the proper length of the coax cable between the Tsunami and the pulse generator that carries the monitor signal. After the delay line, the polarization of the laser beam is set parallel to the plane of incidence, since that polarization state has the highest transmission when using a beam splitter. The waist of the laser beam is increased

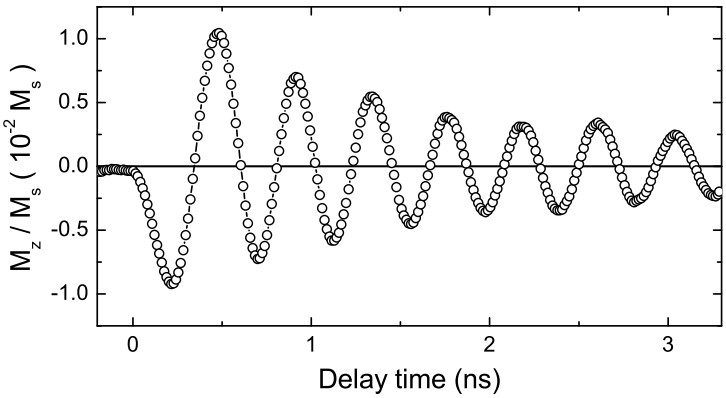

Figure 3.9: Example of a TR-MOKE measurement obtained on a 13×9 μm magnetic ($Ni_{80}Fe_{20}$) element. The precessional motion is triggered by a magnetic field pulse induced by a current line. The external magnetic field was set to 2.5 mT.

with the use of a beam expander in order to cover the full aperture of a 0.65 NA (numerical aperture) microscope objective, which focuses the probe beam on the sample. With this objective, the theoretical diffraction limited spot size is 1.5 μm. The sample holder is mounted on a $\hat{x}-\hat{y}-\hat{z}$ motorized translation stage for accurate positioning and focusing. A magnetic bias field up to 8 kA/m can be applied parallel to the current line with a homemade electromagnet. The reflected probe beam from the sample travels backwards into the objective, and is directed to the detector by the beam splitter. It passes a second polarizer with its axis 45° relative to that of the first polarizer, and is finally focused on the Si-photodiode. Due to the normal incidence of the probe beam, the setup is only sensitive to the polar Kerr-effect, and thus to out-of-plane magnetization. We note that in this configuration preferably the Kerr-rotation is measured, since its sensitivity to out-of-plane magnetization is higher than for Kerr-ellipticity.

However, the Kerr-effect is still very small, and in order to detect it, a modulation scheme is used. The 80 MHz monitor signal from the Ti-sapphire laser system, that functions as the trigger signal for the pulse generator, is sent through a PIN-diode, to which a 10 kHz square wave gate signal is supplied. The monitor signal is thus modulated with 10 kHz, and as a result, the magnetic pulses that induce the fast magnetization dynamics are modulated into 10 kHz pulse trains, see Fig. 3.8. The detector signal will then contain a 10 kHz component, which is extracted with the use of a Stanford Research Systems Digital Signal Processing (DSP) lock-in amplifier (model SR830). Signal-to-noise ratios up to 200:1 can be achieved this way. It is important to stress that the lock-in signal is linearly proportional to the change in Kerr-rotation of the reflected probe beam due to the output current of the pulse

generator. The intensity signal was measured simultaneously with the lock-in signal, by extracting the DC-signal with a low-pass filter.

A typical example of a TR-MOKE measurement, taken on a micron sized magnetic ($Ni_{80}Fe_{20}$) element using magnetic field pulses, is shown in Fig. 3.9. At $t = 0$ ns a precessional motion is launched, which shows similar characteristics as the modeled response presented in Fig. 2.2a. The response after ≈ 0.6 ns, when the magnetic field pulse has ended, can be well described by a damped sine wave with a frequency of 2.4 GHz and a decay time of 2.1 ns. This decay time corresponds to a damping parameter of $\alpha \approx 0.008$ (see Eq. 2.2), which is characteristic for $Ni_{80}Fe_{20}$ [21]. In Chapter 4 we will explore this precessional motion in more detail, and study its spatial and magnetic field dependence.

3.3 TiMMS

Time-resolved Magnetization Modulation Spectroscopy (TiMMS) [22] is a very versatile technique to study spin dynamics in semiconductors, and is the main experimental tool in Chapters 5, 6, and 7. It is a stroboscopic measurement technique according to an all-optical pump-probe scheme. In short, a strong circularly polarized laser pulse excites an electron and hole spin population in a semiconductor via the optical selection rules of the zinc-blende crystal structure. A second, much weaker probe laser pulse measures the evolution of the spin population via the magneto-optical Kerr-effect. The time-difference between arrival of the pump and probe pulse on the semiconductor is controlled by a mechanical translation stage, thereby enabling time-resolved measurements of the excited spin population. By tuning the laser photon energy, full spectroscopic data of the semiconductor under investigation can be obtained. In this Section, we will present the details of the experimental TiMMS-setup, present the signal analysis, and show some illustrative examples of TiMMS-measurements on a spin injection device.

3.3.1 TiMMS-setup

The TiMMS measurements shown in this Thesis are obtained with the experimental setup as schematically shown in Fig. 3.10. The same Spectra-Physics laser system as used in the TR-MOKE setup is employed as a pulsed laser source. It is extended with Lock-to-Clock electronics, which enables synchronization of this laser system with another pulsed laser. This allows two-color experiments with independently tunable laser photon energies for pump and probe beam, even for small differences in laser photon energies (e.g. by locking two Tsunami laser systems).

The output beam of the Tsunami is divided into a strong pump and a much weaker probe pulse with a beamsplitter. The pump beam passes two cube polarizers and a photo-elastic modulator (PEM) before being directed towards a magneto-optical cryostat by a second beam splitter. By tuning the relative angle between

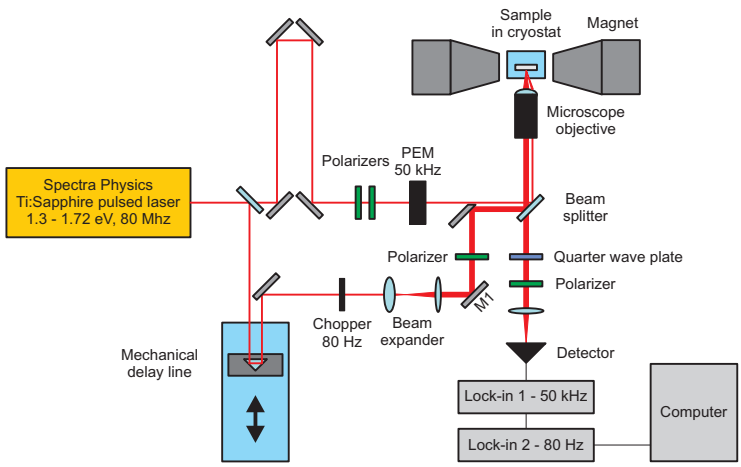

Figure 3.10: Schematic picture of the all-optical TiMMS setup, which is used to detect spin dynamics in semiconductors.

the two cube polarizers, the intensity of the pump beam can be accurately tuned via Malus' law. The second cube polarizer is set at 90° ($p-$polarization) and has a 45° relative orientation to the main axis of the PEM. The PEM retards one of the polarization components of the pump beam at a frequency of 50 kHz, thereby alternatingly producing left- and right-circularly polarized light. Thus the pump beam induces at a frequency of 50 kHz alternatingly an electron spin up and spin down (and a hole spin down and spin up) population in a semiconductor via the optical selection rules of the zinc-blende crystal structure (see Section 2.2).

The probe beam is directed towards a computer controlled mechanical translation stage with a length of 30 cm, which can increase the optical path length corresponding to a maximum time delay of 2 ns. The retroreflector mounted on the translation stage ensures that the probe beam is directed backwards parallel to the incident beam, and that it follows the same path independent of the position of the translation stage. The probe beam then passes a mechanical chopper and polarizer, and is finally directed towards the cryostat by the same beamsplitter as the pump beam.

A high aperture laser objective focuses both pump and probe beam to an overlapping spot on the sample in the cryostat. We used objectives with numerical apertures (NA) of 0.38, and 0.6. In combination with the standard laser beam waist (which is much smaller than the physical aperture of the objectives), these lead to spot sizes of ≈ 19 μm, and ≈ 7 μm, respectively. Since both the incident and reflected pump and probe beam have to fit in the physical aperture (see Fig. 3.11), it is not possible to cover the full physical aperture of the objectives and thereby achieve the theoretical minimum spotsize. However, by placing a beam expander

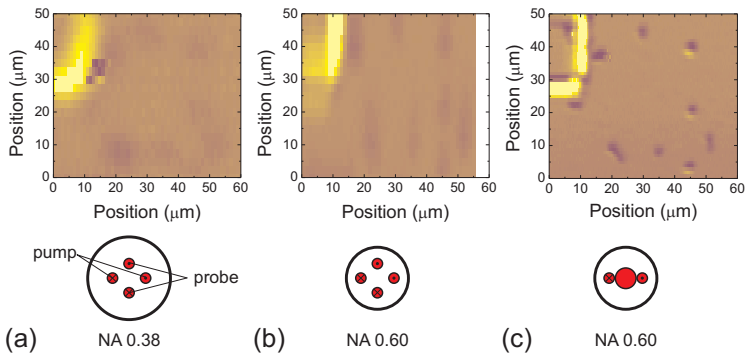

Figure 3.11: Raster scans of the same part of a marker sample with semiconductor nanowires, taken with different objectives, laser beam waists, and position of incidence, as indicated by the schematic illustrations of objective and probe beam. The effect on the spatial resolution is immediate.

in the path of the probe beam, thereby increasing the laser beam waist by a factor of 2, the spot size of the probe beam on the sample could be reduced by the same factor to ≈ 9.5 μm, and ≈ 3.5 μm, respectively. We note that only when the probe beam is incident on the optical axis of the objective (thus through the center of the objective), a minimum spot size in the two lateral directions can be obtained. Figure 3.11 shows the effect of both the laser beam waist, and the position of incidence relative to the optical axis, on the final resolution of a raster scan on a marker sample containing semiconductor nanowires.

The reflected probe beam passes the beamsplitter, followed by a quarter-wave plate, a polarizer (the so-called analyzer), and is finally incident on the detector. The signal from the detector (a silicon photo-diode with amplification electronics) is sent to a first lock-in amplifier (Stanford Research Systems model SR830) locked to the reference frequency of the PEM (50 kHz). The output of the first lock-in amplifier serves as the input of a second lock-in amplifier, locked to the reference frequency of the chopper (typically 80 Hz). This double modulation scheme allows the detection of the generally small magneto-optical Kerr-effect, and ensures that only pump induced changes of the dielectric tensor of the sample are detected. One has to take care that the inverse time-constant of the first lock-in amplifier is much smaller than the reference frequency of the second lock-in amplifier, see Table 3.1.

The resulting signal output of the second lock-in amplifier depends on the settings of the quarter-wave plate and analyzer. In the following Section the signal analysis of the TiMMS technique using the Jones-formalism will be outlined.

Returning to the setup shown in Fig. 3.10, we note that the objective is mounted to a $\hat{x}-\hat{y}-\hat{z}-$motorized translation stage system, facilitating accurate positioning of

Table 3.1: Lock-in amplifier settings for the TiMMS-setup.

Lock-in	f_{ref}	$1/f_{ref}$ (ms)	t_c (ms)	cycles
1 (PEM)	50 kHz	0.02	1	50
2 (chopper)	80 Hz	12.5	300	24

the objective with respect to the sample. Positioning of the laser spot on the sample is achieved by moving the objective in the $\hat{y} - \hat{z}$ plane. Because the beamsplitter moves together with the objective in the $\hat{y}$ direction, the relative position of the laser beam to the optical axis is unchanged. In the $\hat{z}$ direction, however, only the objective moves, which can lead to a reduced resolution when the probe beam is displaced from the optical axis. The motorized $\hat{x}$ axis facilitates accurate focusing of the laser beams, as the depth of focus is only several micrometers for the 0.6 NA objective. Furthermore, the probe spot on the sample can be accurately and independently moved with respect to the pump spot by adjusting the angle of incidence via the differential micrometer screws on mirror M1 (see Fig. 3.10).

As mentioned, the sample is placed in a magneto-optical flow-cryostat (Oxford MicrostatHe), that allows optical access via glass windows on all four sides. The sample can be glued directly on one side of the cold finger, or can be glued on a chip carrier which can be mounted on the other side of the cold finger in a chip foot. Electrodes or bondpads on the sample can be connected to the chip carrier by wire-bonding. The pins of the chip carrier are in turn connected to the output connector of the cryostat via the chip foot and inner wiring. This way, ten connections to a sample can be accessed from outside, which allows for $I - V-$measurement, photocurrent measurement, or simply applying a bias at variable temperatures. The cryostat is cooled with liquid helium. The temperature can be accurately controlled between 4.2 K and room temperature by an automated $p-i-d-$controller (Oxford ITC503S) that sets the helium flow rate and the heater voltage. A magnetic field can be applied using a homemade water-cooled electromagnet. The maximum field strength between the poles of the magnet strongly depends on the air-gap. When the cryostat is inserted between the poles this air-gap is ≈ 4 cm. The field strength at the maximum current of the current source (10 A) is ≈ 0.35 T. The poles can be rotated by $\approx 30°$ in order to change from an in-plane magnetic field to a canted orientation with an out-of-plane component.

3.3.2 Signal analysis

The TiMMS-signal detected by the Si-photodiode can be calculated using the Jones-calculus. We can describe the pump and probe beam by Jones vectors containing the orthogonal transverse components of the electric field. The optically active elements in the experimental setup, such as the PEM, the sample under investigation,

polarizers, and quarter wave-plates, are described by Jones-matrices. Let us start with the pump beam. The polarization of the pump beam at the sample is given by its initial polarization vector, $\vec{E}^0_{pu}$, multiplied with the Jones-matrix of the PEM, $\mathbf{M}_{PEM}$. Following the setup of Fig. 3.10, the polarization vector at the sample position, $\vec{E}^{sam}_{pu}$, is given as

$$\vec{E}^{sam}_{pu} = \mathbf{M}_{rot(-45)} \cdot \mathbf{M}_{PEM} \cdot \mathbf{M}_{rot(45)} \cdot \vec{E}^0_{pu} \tag{3.17}$$

with $\mathbf{M}_{rot(\alpha)}$ the Jones-matrix for a rotation over α degrees. Writing down the full matrices, we have

$$\vec{E}^{sam}_{pu} = \frac{1}{\sqrt{2}} \begin{pmatrix} 1 & 1 \\ -1 & 1 \end{pmatrix} \cdot \begin{pmatrix} 1 & 0 \\ 0 & \exp[\imath A(t)] \end{pmatrix} \cdot \frac{1}{\sqrt{2}} \begin{pmatrix} 1 & -1 \\ 1 & 1 \end{pmatrix} \cdot E^0_{pu} \begin{pmatrix} 0 \\ 1 \end{pmatrix} \tag{3.18}$$

with E^0_{pu} the amplitude of the pump beam, $A(t) = A_0 \cos(2\pi f t)$, A_0 the PEM retardation, and f the operating frequency of the PEM. Equation 3.18 results after some algebra in

$$\vec{E}^{sam}_{pu} = E^0_{pu} \left[A_+(t) \frac{1}{\sqrt{2}} \begin{pmatrix} 1 \\ \imath \end{pmatrix} + A_-(t) \frac{1}{\sqrt{2}} \begin{pmatrix} 1 \\ -\imath \end{pmatrix} \right] \tag{3.19}$$

with $A_\pm(t) = (1 \pm \imath)(\pm\imath + \exp[\imath A(t)])/2\sqrt{2}$. From 3.19 it follows that the polarization of the pump beam at the sample alternates between left- and right-circularly polarized light at a frequency f. Via the optical selection rules a net spin population is induced, proportional to $|A_+|^2 - |A_-|^2 = \sin[A(t)]$, which leads to non-vanishing off-diagonal elements of the dielectric tensor of the sample. This in turn leads to a complex Kerr-rotation of the probe beam, whose polarization state at the detector, $\vec{E}^{det}_{pr}$ (following again Fig. 3.10) can be written as

$$\vec{E}^{det}_{pr} = \mathbf{M}_{POL} \cdot \mathbf{M}_{QWP(45)} \cdot \mathbf{M}_{sam} \cdot \vec{E}^0_{pr} \tag{3.20}$$

with $\vec{E}^0_{pr}$ the $s-$polarization of the incident probe beam, $\mathbf{M}_{sam}$, $\mathbf{M}_{QWP(45)}$, and $\mathbf{M}_{POL}$ the Jones-matrices of the sample, quarter-wave plate and polarizer, respectively. Writing again the full matrices, we obtain

$$\vec{E}^{det}_{pr} = \begin{pmatrix} 1 & 0 \\ 0 & 0 \end{pmatrix} \cdot \frac{(1+\imath)}{2} \begin{pmatrix} 1 & \imath \\ \imath & 1 \end{pmatrix} \cdot \begin{pmatrix} r_{ss} & r_{sp}\theta(t) \\ r_{ps}\theta(t) & r_{pp} \end{pmatrix} \cdot E^0_{pr} \begin{pmatrix} 1 \\ 0 \end{pmatrix} \tag{3.21}$$

with E^0_{pr} the amplitude of the probe beam, and $\theta(t) = \sin[A(t)]$. After some algebra, Eq. 3.21 can be simplified to

$$\vec{E}^{det}_{pr} = \frac{E_{pr}}{2}(1+\imath) \begin{pmatrix} r_{ss} - \imath r_{ps}\theta(t) \\ 0 \end{pmatrix}. \tag{3.22}$$

From Eq. 3.23 it follows that the complex Kerr-rotation of the probe beam oscillates with the frequency of the PEM, as expected. The voltage-output of the detector is

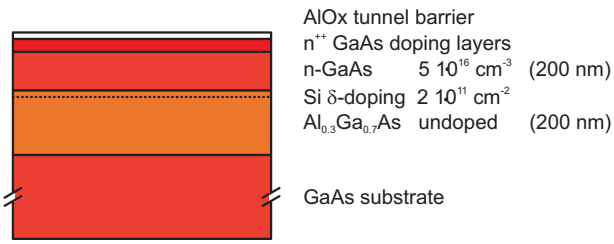

Figure 3.12: Schematic layout of the semiconductor heterostructure, which is the basis for an all-electrical spin injection and detection device, proposed by and fabricated at IMEC Leuven [23].

then given by

$$V_{det} \propto (\vec{E}^0_{pr})^* \vec{E}^0_{pr} = \left(\frac{E^0_{pr} r_{ss}}{2}\right)^2 \times$$
$$\left(2 + \frac{r^2_{ps}}{r^2_{ss}} + 4\frac{\Re(r_{ss})\Im(r_{ps}) - \Im(r_{ss})\Re(r_{ps})}{r^2_{ss}} \sin[A(t)] - \frac{r^2_{ps}}{r^2_{ss}} \cos[A(t)]\right). \quad (3.23)$$

Expanding the terms $\sin[A(t)] = \sin[A_0 \cos(2\pi f t)]$ and $\cos[A(t)] = \cos[A_0 \cos(2\pi f t)]$ in Bessel-function of the first kind, we find for the ratio of the $1f$ and dc components of the detector signal

$$\frac{V_{1f}}{V_{dc}} = 4J_1(A_0)\epsilon_K. \quad (3.24)$$

V_{1f} is thus proportional to the Kerr-ellipticity. If the angle of the final polarizer is set to 45°, it can be shown that V_{1f} is proportional to the Kerr-rotation.

3.3.3 An example: TiMMS on a spin injection device

As an example of the capabilities of the TiMMS-setup, we show results of spin relaxation and spin diffusion measurements on samples originally designed for all-electrical spin injection and detection in GaAs. The samples were grown at IMEC Leuven [23], and the common layout is schematically shown in Fig. 3.12. All samples consist of a AlOx tunnel barrier, a 200-nm GaAs spin transport channel, with high doping layers near the top surface, and an $Al_{0.3}Ga_{0.7}As$ blocking layer at the bottom. The $Al_{0.3}Ga_{0.7}As$ blocking layer facilitates a confined current flow in the lateral directions, by prohibiting current flow in the vertical direction. The Si δ-doping in the $Al_{0.3}Ga_{0.7}As$ layer is inserted to render the device insensitive to surface depletion and variations in the etching process. The heterostructure is grown on a semi-insulating GaAs substrate. Ferromagnetic contacts and the tunnel injector are not

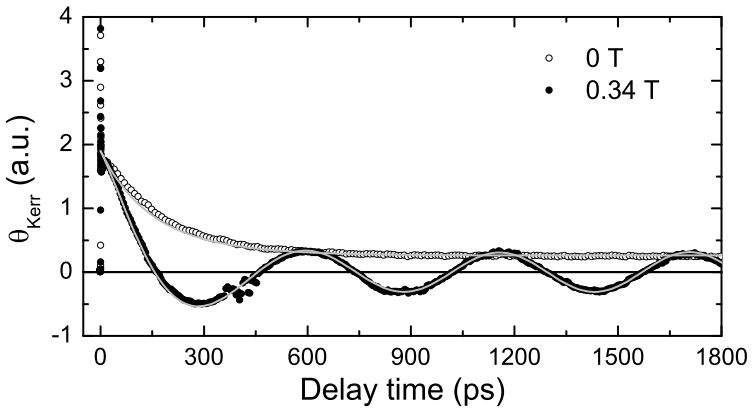

Figure 3.13: TiMMS-measurement on an IMEC spin injection device, taken with a laser fluence of 40 μJ/cm^2, and with an external magnetic field of $B = 0$ T and $B = 0.34$ T. Solid lines are results of the model of Section 2.5.

shown. The precise doping profile near the top interface is different for different samples, as well as the technique used for the definition of the structures (wet etching or ion-milling). These details are, however, not relevant for the present example. Below, we show three examples of TiMMS-measurements: as a function of pump-probe delay time, as a function of an external magnetic field, and as a function of pump-probe spatial distance.

First, we present time-resolved measurements on an IMEC spin injection device with the external transverse magnetic field $B = 0$ T, and $B = 0.34 \pm 0.01$ T, as shown in Fig. 3.13. The error in the magnetic field results from the fact that the position of the sample in the cryostat is not exactly at the position of the field calibration. At $\Delta t = 0$ ps a sharp increase in the TiMMS-signal is observed as a result of optical spin orientation due to the pump pulse. During the first few ps the TiMMS-signal decays rapidly to approximately half the initial value, which can be attributed to carrier redistribution, thermalization processes, and hole spin relaxation. After the first few ps the signal decays in a two-step process, the first on a timescale of several hundreds of picoseconds, and the second on a multi-nanosecond timescale, since the signal lasts longer than the time-window of the measurement. For the measurement at $B = 0.34$ T this decay forms the envelope of an oscillation, which is the signature of spin precession due to application of the transverse magnetic field (as discussed in Section 2.5). The decay of the signal represents a decrease of the spin density in the heterostructure, which can have several origins. First, the signal might originate from either the transport channel, or from the substrate. Second, the decrease of the spin density might result from spin relaxation mechanisms, or from carrier recombination. It will become clear that the dominant part of the signal originates

from the transport channel, and that the first (0-400 ps) decay-process is due to carrier recombination, and the second (> ns) is due to spin relaxation.

A closer look on the measurement at $B = 0.34$ T reveals that the period of the oscillation starting from the first maximum at $\Delta t = 603$ ps is constant and equal to 554 ps. Clearly, this shows that the period of the first full oscillation is longer by 48 ps (or $\approx 9\%$). As the phase of the precession at $\Delta t = 0$ is zero (i.e. all spins are aligned normal to the sample surface, and hence the TiMMS-signal is maximal), this means that during the first few hundred ps these spins precess with a lower frequency. A slower precession might be caused by a lower g factor. Also, it is known that the electron g factor decreases with higher electron energy, as stated in Section 2.5. With the laser fluence of the experiment, we expect an optically induced carrier density well above 10^{17} cm^{-3}. With this density, electrons at the electron quasi Fermi-level will have a lower g factor than those near the band edge. Recombination lowers the electron quasi Fermi-level, which increases the g factor. We thus conjecture that the phase shift is caused by a carrier density effect, via a time-dependent electron g factor.

This conjecture implies that recombination takes place during the first few hundred ps. We have already examined the effect of a relative high laser induced carrier density and recombination on the spin relaxation, with the model of Section 2.4. It was found that initially, recombination is the dominant source of decay of the spin density, and that after recombination the spin relaxation time is determined by the donor concentration, see Fig. 2.7c. Qualitatively, the model shows the main features of the experimental result with $B = 0$ T, in agreement with our conjecture. It is, however, not possible to simulate the exact measured time-trace with the model. One reason might be that the recombination parameter is not constant, as the precise band alignment in the transport channel depends on the free carrier density. At low carrier densities, a small internal electric field exists due to Fermi level pinning at the tunnel barrier. This internal electric field can separate free electrons and holes, leading to a lower recombination rate, and a different decay of the spin polarization. A second reason might be that the measurement data contains a weak signal originating from the substrate. Because the substrate consists of semi-insulating GaAs, this possible signal is only expected to be present during the first few hundred ps [24].

Using the model of Section 2.5 to simulate the spin precession data, we can achieve a very nice agreement with the experimental data when using an optically induced carrier density of $1.5 \cdot 10^{17}$ cm^{-3}, a recombination time of 180 ps, a magnetic field of $B = 0.333$ T, and a final spin polarization of $1.0 \cdot 10^{16}$ cm^{-3}. This result supports our conjecture that the main experimental features of Fig. 3.13 are the result of recombination and a carrier density dependent electron g factor.

We already mentioned that the second decay process is due to spin relaxation in the transport channel. From Fig. 3.13 it is, however, difficult to extract the spin relaxation time. From the donor concentration, a spin relaxation time of $30 - 40$

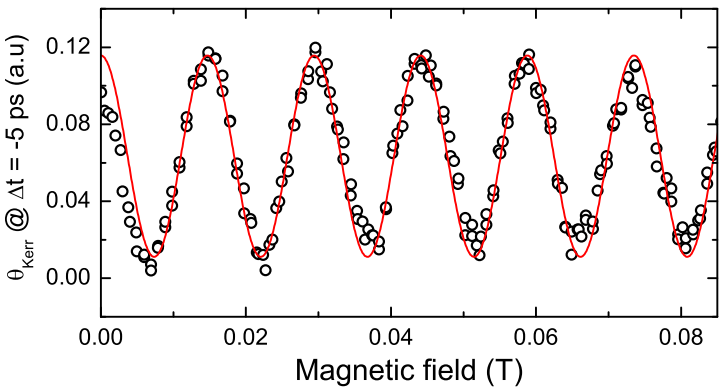

Figure 3.14: Measurement of the TiMMS-signal on an IMEC spin injection device, taken with a laser fluence of 40 μJ/cm^2, as a function of magnetic field at a fixed time delay of $\Delta t = -5$ ps.

ns is expected. However, we have seen in Section 2.5 that spin dephasing due to a distribution of g factors effectively limits the spin relaxation time, which can be reduced to a couple of ns. Using Eq. 2.25 with $B = 0.332$ T and $\Delta g = 0.005$, an effective spin lifetime of $T_{eff} \approx 9$ ns is obtained. The next example shows an effective way to determine the spin relaxation time.

The second example is a TiMMS measurements as a function of an externally applied magnetic field, taken at a pump-probe delay time of $\Delta t = -5$ ps, as shown in Fig. 3.14. At this delay time the probe pulse arrives ≈ 12.495 ns after the pump pulse (and 5 ps before the next pump pulse), because of the 80 MHz repetition rate of the laser. Due to the large spin lifetime already observed in Fig. 3.13, the TiMMS-signal is still detectable at this delay time (although this is not very clear from Fig. 3.13). The oscillatory signal is a result of spin precession. Increasing the external magnetic field increases the precession frequency. First, this leads to a decrease of the signal, which is minimal when the first minimum of the precession coincides with $\Delta t = 12.495$ ns. Increasing the magnetic field further leads to the successive coinciding of maxima and minima of the spin precession at this delay time. Comparing the amplitude of the oscillation with the amplitude of the TiMMS-signal at $\Delta t = +1.15$ ns (well after full recombination), we extract a spin lifetime of $T_s = 6.5 \pm 0.5$ ns. This spin relaxation time suggests that indeed spin dephasing limits the spin lifetime in the present examples. From the frequency of the oscillation we can also extract the g factor, via $g = \hbar\omega/\mu_B \Delta t$. Fitting the data to the function $\cos(\omega B)$ yields $\omega = 428 \pm 3$ T^{-1}. From this we extract a g factor of 0.39 ± 0.01. We estimate the error in the g factor somewhat higher than the one obtained from the fit, to include a small uncertainty in the magnetic field calibration. This g factor is lower than the literature value of 0.44, but consistent with an energy dependent g

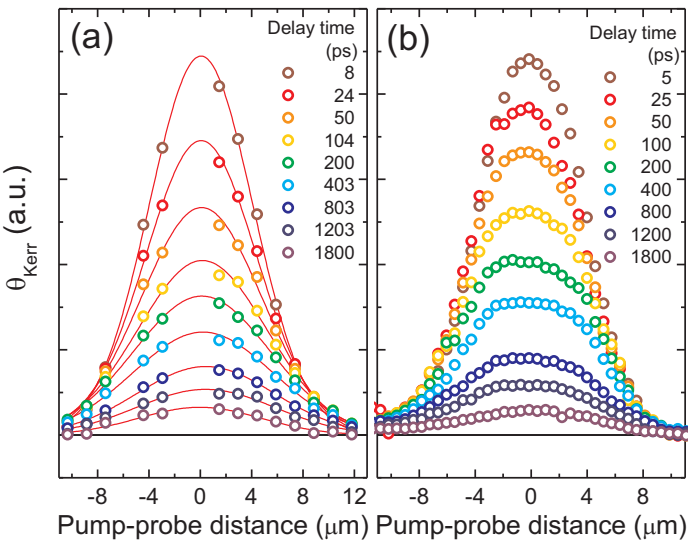

Figure 3.15: Measured spatial profiles of the pump-induced spin population on an IMEC spin injection device. (a) Measurement points are extracted from time-resolved measurements at different pump-probe spatial distance. (b) Measurement points are taken by scanning the probe beam over the pump spot at fixed time delays.

factor at a donor concentration of $5 \cdot 10^{16}$ cm^{-3}.

Finally, we show results from spatially resolved measurements, by changing the position of the probe beam with respect to the fixed position of the pump beam. This technique allows the study of spin diffusion and/or transport [25]. In Fig. 3.15 we present measurements of spin diffusion and relaxation. In Fig. 3.15a, data from time-resolved measurements at fixed pump-probe spatial distances is shown. Only data points for a few delay times are plotted. The data in Fig. 3.15b is obtained by scanning the probe beam over the pump spot at fixed time-delays. In both figures, we observe that data points belonging to the same delay time form a Gaussian profile, and that the amplitude of these profiles decreases with increasing delay time. In Fig. 3.15b it is more apparent that the Gaussian profile flattens at the center at longer delay times.

These data show the lateral spin density profile, which is expected to have a Gaussian shape as the spin density is induced by a laser pulse with a Gaussian spatial intensity profile. The solid lines in Fig. 3.15a are Gaussian fits to the data, from which the amplitude and width are extracted for each delay time. In Fig. 3.16 the square of the width, w^2, is plotted as a function of the delay time, Δt. In a diffusion process, w^2 should scale linearly with Δt. In Fig. 3.16 we observe two regimes. In

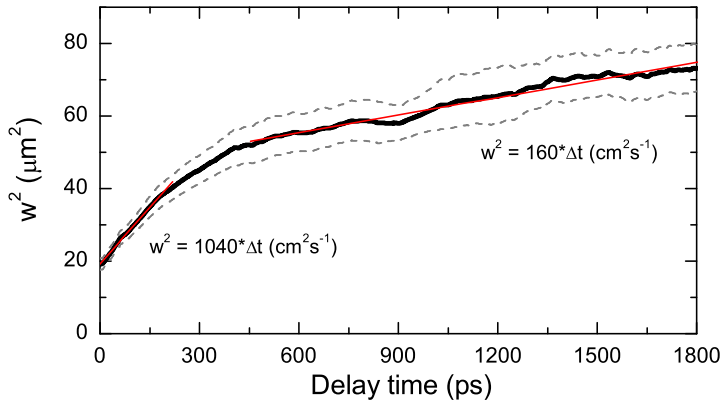

Figure 3.16: The square of the width of the Gaussian spin profile as a function of delay time.

the first regime, for $0 < \Delta t < 400$ ps, a fast increase of the width is observed. It is in this regime that the flattening of the Gaussian shape develops. This flattening is likely related to a carrier density effect, as in this regime carrier recombination is an important process. We have seen in Section 2.3 that carrier recombination can be different for spin up and spin down electrons, depending on their density. Because the optically induced lateral carrier density has a Gaussian shape, a spatially varying recombination rate of spin up and spin down electrons is expected when the excited carrier density is comparable or higher than the equilibrium carrier concentration. For such a case we show schematically in Fig. 3.17 the the evolution of the electron and hole spin up and spin down lateral densities after optical orientation. Because the recombination rate is proportional to both the electron and hole density, spin up electrons experience a higher recombination rate than spin down electrons. Thus, the spin polarization decreases faster at the center of the Gaussian than at its wings due to this recombination effect, thereby flattening the Gaussian profile.

The second regime in Fig. 3.16, for $600 < \Delta t < 1800$ ps, is thus related to the broadening of the (flattened) Gaussian profile after recombination. This broadening can be attributed to lateral spin diffusion, and from the slope of the curve we can extract the spin diffusion constant D_s via

$$D_s = \frac{1}{4}\frac{d(w^2)}{dt}. \tag{3.25}$$

From Fig. 3.16 we find $D_s = 40$ cm^{2}s^{-1}, which is of the same order compared to reported values of $D_s \approx 15$ cm^{2}s^{-1} with $n_D = 5 \cdot 10^{16}$ cm^{-3} [26]. This suggests that pure spin diffusion is the main contributor to the broadening of the Gaussian profiles, possibly as a result of a relatively high spin density compared to the donor concentrations, as shown in Fig. 3.17.

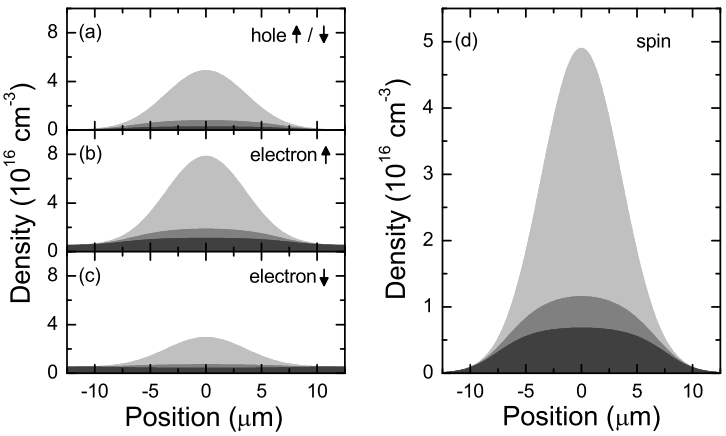

Figure 3.17: Schematic representations of the spatial distributions of (a) the spin up and spin down holes (b) spin up electrons (c) spin down electrons, and (d) the total spin. The curves in gray-scale correspond to three different times after optical orientation.

In summary, we have shown that microscopic TiMMS is a very powerful technique to study spin related phenomena in semiconductors, such as spin relaxation, spin precession and dephasing, and lateral spin transport and diffusion.

3.4 Modeling TiMMS for heterostructures

In the previous Section we have described the TiMMS setup, performed the signal analysis at the detector, and presented an illustrative example. In this Section we will describe a model to calculate the TiMMS signal amplitude as a function of photon energy for an arbitrary semiconductor heterostructure. The spectral dependence is modeled using the analysis of Koopmans *et al.* [27], and is combined with a calculation of the Kerr-effect for an arbitrary heterostructure, analogues to the calculation of the Kerr-effect from magnetic multilayers in Section 3.1.5.

The procedure of the calculation is schematically depicted in Fig. 3.18. First, the heterostructure, consisting of layers of different material, L_n, is divided in sublayers l_m of thickness Δz. Each sublayer l_m is assigned the appropriate photon energy (E_{ph}) dependent complex refractive index $N_{l_m}(E_{ph})$ and magneto-optical Voigt constant, using literature values. Second, the absorption profile as a function of depth z, $A(z)$, is calculated in the low fluence limit for each photon energy using the transfer matrix approach [15]. This yields $A(E_{ph}, z)$, which is convoluted with a Gaussian with full-width at half-maximum, Δ, to account for the finite spectral width of the laser pulse. Next, the complex Kerr-rotation, K, originating from each

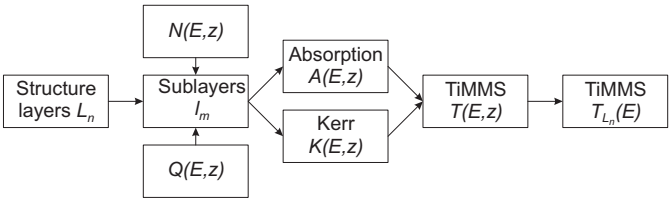

Figure 3.18: Modeling scheme for the TiMMS-signal originating from heterostructures.

l_m is calculated for each photon energy using the matrix approach of Zak *et al.* (see Section 3.1.4). This is done by calculating the complex Kerr-rotation of the full heterostructure, while artificially setting only for a single sublayer l_m a nonzero complex magneto-optical Voigt parameter, in a similar way as in Section 3.1.5 for the CoPt-multilayer. Finally, the calculation yields $K(E_{ph}, z)$. Using this $A(E_{ph}, z)$ and $K(E_{ph}, z)$ the TiMMS spectral response of each sublayer l_m, $T(E_{ph}, z)$, can be calculated following Koopmans *et al.* [27], which we shall briefly discuss in the following.

The pump and probe pulses from the Ti:Sapphire laser in the experiment have a Gaussian spectral shape, and can be written as

$$I_n(E_n) = A_n \exp\left(-\left[\frac{(E - E_n)}{\Delta}\right]^2\right), \tag{3.26}$$

with A_n the amplitude, and E_n the center photon energy, with $n = pu, pr$ for the pump and probe pulse, respectively. Absorption of a circularly polarized pump pulse leads, via the optical selection rules, to an excited spin polarized electron (hole) density in the conduction (valence) band, denoted as $n_{e,\sigma}(E)$, and $n_{h,\sigma}(E)$, respectively, with $\sigma = \pm$ for spin up and spin down. Since the hole spin relaxation rate is much faster than the electron spin relaxation rate for bulk III-V semiconductors, we will only consider the electron spin density. Also, we will consider a fully thermalized electron system, which is appropriate for delay times larger than the electron thermalization time of typically one ps. The spectral profile of the electron spin density is determined by the total amount of excited carriers, N_e, the density of states, and the temperature, T. In the model, we use the absorption profile $A(E_{pu}, z)$ of the pump pulse to determine N_e in every sublayer l_m for each E_{pu}. Using a 3D density of states (see Eq. 2.14, and a Fermi-Dirac-distribution of the electrons, the electron density can be written as

$$n_e(E) = 8\pi\sqrt{2}\left(\frac{m_e}{h^2}\right)^{3/2} \frac{\sqrt{E - E_g}}{\exp\frac{E - E_F(N_e)}{k_B T} + 1}, \tag{3.27}$$

with m_e the electron effective mass in the conduction band, E_g the bandgap of the material, $E_F(N_e)$ the electron quasi-Fermi level after laser excitation corresponding

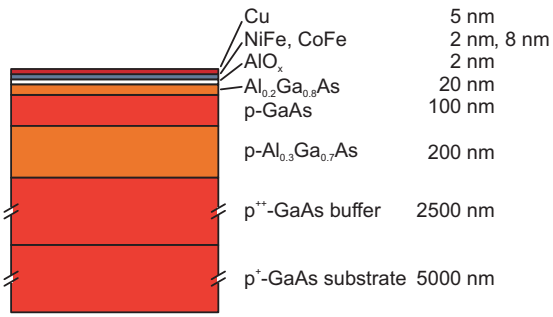

Figure 3.19: Schematic picture of the heterostructure at the optical window of the spin-LED.

to the total excited electrons N_e, and k_B Boltzmann's constant. The excited electron spin density induces a change in the oscillator strength for left- and right-handed circularly polarized light, and is given by the spin-polarized joined density of states profile

$$f_+ - f_- \propto n_{e,+}n_{h,-} - n_{e,-}n_{h,+} = (n_{e,+} - n_{e,-})n_h. \tag{3.28}$$

The pump-induced off-diagonal element of the dielectric tensor, ϵ_{xy}, is related to the induced difference in oscillator strength by

$$\epsilon_{xy}(E_{pu}) = \int_{-\infty}^{\infty} \frac{f_+(E) - f_-(E)}{E - E_{pu} - \imath\gamma} dE. \tag{3.29}$$

The complex Kerr-rotation of the probe beam due to the nonzero $\epsilon_{xy}(E_{pu})$, is obtained by weighing $\epsilon_{xy}(E_{pu})$ with the spectral shape of the probe beam, I_{pr}, and with $K(E_{pr}, z)$ to account for the depth and photon energy dependence of the complex Kerr-rotation

$$\theta_K(E_{pr}, z) = \int_{-\infty}^{\infty} \epsilon_{xy}(E_{pu}) I_{pr}(E_{pr}) K(E_{pr}, z) dE_{pu}. \tag{3.30}$$

$\theta_K(E_{pr}, z)$ is calculated for every sublayer l_m and probe photon energy E_{pr}, finally yielding $T(E_{pr}, z)$. By summing all $T(E_{pr}, z)$ for which z is within the same layer, the spectral shape of the TiMMS response originating from a full layer, $T_{L_n}(E_{pr})$, is obtained.

We will take the spin-LED, which is the subject of Chapter 5, as an example to exemplify all the steps in the calculation outlined above. The schematic layout of the spin-LED that we will use in the modeling is shown in Fig. 3.19. Note that we will only model 5 μm of the substrate, since the penetration depth of light with

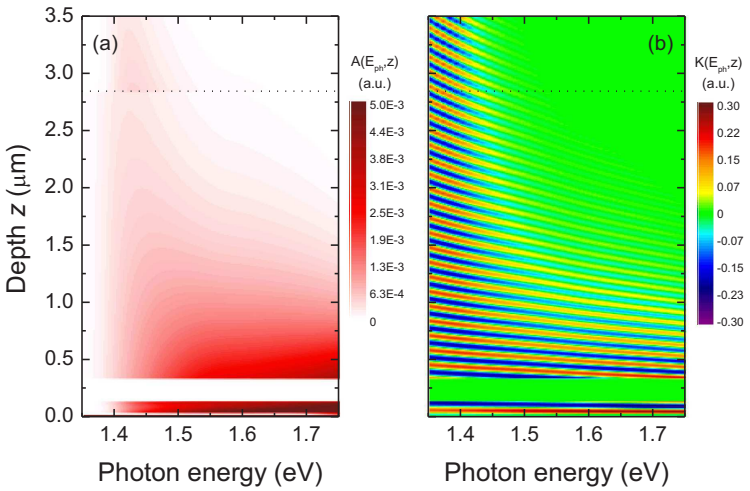

Figure 3.20: (a) Absorption profile $A(E_{ph}, z)$ of the spin-LED. (b) Kerr-ellipticity profile $K(E_{ph}, z)$ of the spin-LED. The dotted line marks the interface between the buffer layer and the substrate.

photon energies a few tens of meV above the bandgap is around 1 μm. We are especially interested in the contributions of the $p-$GaAs and buffer layer to the total TiMMS signal. We restrict ourselves to the energy window of 1.3 - 1.8 eV, as this covers the full range of the Tsunami laser system, and thereby the experimental results. Also, we consider the degenerate case in which the photon energy of both pump and probe beam are equal ($E_{pu} = E_{pr}$), and denote the photon energy as E_{ph}. The spin-LED is modeled at room temperature, with a bandgap for GaAs of $E_{g,GaAs} = 1.42$ eV, and for $Al_{0.2}Ga_{0.8}As$ of $E_{g,Al_{0.2}Ga_{0.8}As} = 1.67$ eV [28].

The first step is dividing the layers of the spin-LED in sublayers of thickness Δz. We have taken $\Delta z = 1$ nm, which yields 7838 sublayers including a top air layer, while still giving rise to a manageable computation time. After assigning the proper (magneto)-optical constants [17, 18], the absorption profile, $A(E_{ph}, z)$, in the spin-LED can be calculated. The result is shown in Fig. 3.20a, up to a depth of 3.5 μm. Above the GaAs-bandgap at 1.42 eV, the absorption increases strongly, such that only for photon energies close to the bandgap carriers are excited in the substrate. The buffer layer thus effectively blocks any signal from the substrate. Note that at energies slightly above the bandgap, the absorption oscillates in the $p-$GaAs layer as a function of depth z, as a result of multiple interface reflections with the $Al_{0.2}Ga_{0.8}As$ and $Al_{0.3}Ga_{0.7}As$ interfaces.

The calculation of the complex Kerr-rotation for the spin-LED yields information on both the Kerr-rotation, and the Kerr-ellipticity. Figure 3.20a shows $K(E_{ph}, z)$ for the case of ellipticity. Several aspects of this Figure deserve further attention. First,

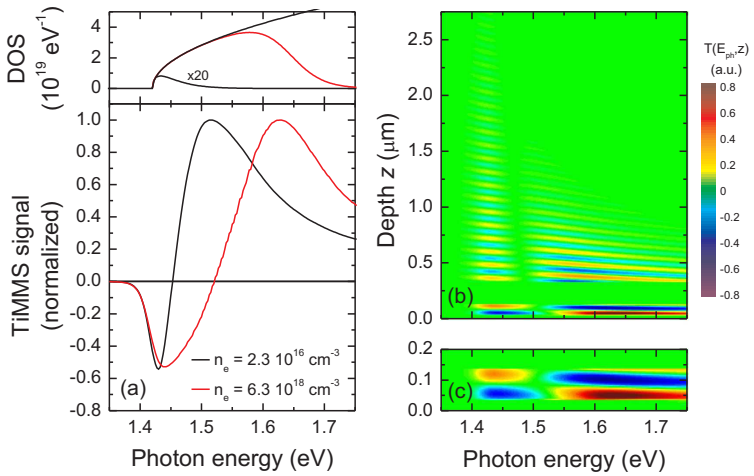

Figure 3.21: (a) TiMMS-spectrum originating from $z = 60$ nm (20 nm below the $Al_{20}Ga_{80}As$ / $p-$GaAs interface), for carrier densities of $n_e = 2.3 \cdot 10^{16}$ cm^{-3} and $n_e = 6.3 \cdot 10^{18}$ cm^{-3}. The top part of (a) shows the density of states for these two carrier densities (b) TiMMS-spectral profile $T(E_{ph}, z)$ of the spin-LED for $n_e = 6.3 \cdot 10^{18}$ cm^{-3}. (c) Magnification of $T(E_{ph}, z)$ for the $p-$GaAs part of (b).

an oscillatory dependence of the Kerr-ellipticity is observed as a function of depth z. This reflects the alternating phase of the electromagnetic wave in the $\hat{y}$ direction (due to a finite ϵ_{xy}), with respect to the main reflection at the air/copper interface. The oscillation period is simply half the wavelength of the light in the material, as the light travels back and forth in the spin-LED. For $E_{ph} = 1.5$ eV e.g., the oscillation period is 113.7 nm, only slightly larger than the thickness of the $p-$GaAs active layer. This implies that the total signal originating from the $p-$GaAs active layer will be relatively low, as the positive and negative contributions tend to cancel each other. Second, the amplitude of the Kerr-ellipticity-oscillation is high over the full depth range for $E_{ph} < E_g$, but decreases with depth for $E_{ph} > E_g$. This behavior results from the effect of zero absorption for $E_{ph} < E_g$, and increasing absorption for higher $E_{ph} > E_g$, thereby diminishing $K(E_{ph}, z)$ at large z. This calculation clearly takes not into account the number of excited carriers in each layer l_m, otherwise $K(E_{ph}, z)$ would be zero for $E_{ph} < E_g$, because no carriers are excited when the photon energy is below the bandgap.

The next step is the calculation of the TiMMS spectral profile for each sublayer. Figure 3.21a shows the normalized TiMMS-spectral profile for low ($n_e = 2.3 \cdot 10^{16}$ cm^{-3}), and high ($n_e = 6.3 \cdot 10^{18}$ cm^{-3}) carrier densities at the first maximum of $K(E_{ph}, z)$ in the the $p-$GaAs active layer, at $z = 60$ nm. At this z we can compare the spectral shapes for low and high fluence without the modulation of $K(E_{ph}, z)$,

because $K(E_{ph}, z)$ is fairly constant as a function of E_{ph} due to its close proximity to the surface. The low fluence curve shows a negative peak around the band-gap, followed by a higher positive peak, which decreases to zero at higher energies. This behavior follows from the convolution of a Lorentzian curve with the spin polarized density of states in the conduction band. The curve is in qualitative agreement with the calculation of Koopmans *et al.* [27], although in that calculation a two-dimensional density of states was used. At high fluence, the zero crossing shifts to higher energies, which is caused by band-filling due to the higher carrier density (as indicated in the top part of Fig. 3.21a). We note that at this relatively high carrier density, several effects take place, which are not included in the model. Besides the already mentioned band-filling, also absorption bleaching near the bandgap (or shift of the absorption edge), and band-gap renormalization take place [29]. Absorption bleaching is the result of band-filling, as the occupied states at the bottom of the conduction band bleach the optical transitions with energies close to the bandgap. The absorption spectrum will thus experience a blue-shift. Band-gap renormalization is a consequence of many-particle interactions, resulting in screening of electrons (holes), thereby decreasing (increasing) the energy of the conduction (valence) band. The net result is a decrease of the band-gap, and a red-shift of the absorption spectrum. Both effects thus have opposite effects, which makes it difficult to predict the net change to the absorption spectrum, and thereby to the TiMMS spectral shape. The TiMMS-spectral shape calculated with the model at all depths z, $T(E_{ph}, z)$, and at $n_e = 6.3 \cdot 10^{18}$ cm^{-3}, is shown in Fig. 3.21b. Here, both the effects of absorption via $A(E_{ph}, z)$, and the depth dependent Kerr-ellipticity via $K(E_{ph}, z)$ are evident. At energies where there is no absorption, the TiMMS-signal is zero, and at energies with high absorption, the TiMMS-signal decreases significantly at higher z. Also, the sign of the TiMMS-signal oscillates, the same way as $K(E_{ph}, z)$.

With the information of Fig. 3.21, the TiMMS-spectrum originating from the $p-$GaAs and the buffer layer can be calculated by summing the different spectra at all z within each layer. We performed the calculation for a wide range of carrier densities, thereby obtaining the TiMMS-spectrum of the $p-$GaAs ($T_{p-GaAs}(E_{ph}, n_e)$), and the buffer layer ($T_{buffer}(E_{ph}, n_e)$) as a function of carrier density. In Fig. 3.22 we plot $T_{p-GaAs}(E_{ph}, n_e)$, and $T_{buffer}(E_{ph}, n_e)$ in a two-dimensional graph, and $T_{p-GaAs}(E_{ph})$, and $T_{buffer}(E_{ph})$, for three different carrier densities. An important observation is that the contributions of the $p-$GaAs and buffer layer are completely different for all carrier densities. Firstly, the maximum amplitude of T_{p-GaAs} is higher than that of T_{buffer} as a result of absorption. Secondly, T_{buffer} shows three peaks (two positive and one negative) of comparable amplitude for all carrier densities, while in the plot of T_{p-GaAs} only one peak at low carrier density, and two at high carrier density are observed. This difference originates from the z-dependence of $K(E_{ph}, z)$, and the summation of contributions for many different z's. Finally, the position of the zero-crossing between the main positive and negative peak in T_{p-GaAs} shifts to higher energy with increasing carrier density, as a result of band-

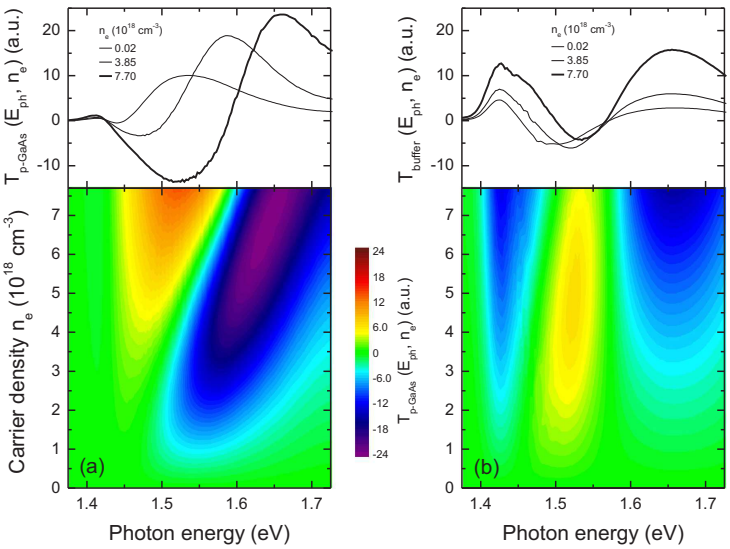

Figure 3.22: (a) Bottom: 2D-plot of the TiMMS-spectrum originating from the $p-$GaAs layer of the spin-LED as a function of carrier density, $T_{p-GaAs}(E_{ph}, n_e)$. Top: $T_{p-GaAs}(E_{ph})$ for three different carrier densities. (b) Bottom: 2D-plot of the TiMMS-spectrum originating from the buffer layer of the spin-LED as a function of carrier density, $T_{buffer}(E_{ph}, n_e)$. Top: $T_{buffer}(E_{ph})$ for three different carrier densities.

filling effects discussed above.

Comparing experimental TiMMS-spectra taken on the spin-LED with the ones calculated above, enables discrimination between contributions from different layers of the semiconductor heterostructure. Full time- and spectrally-resolved TiMMS-data thus allows us to study the electron spin relaxation mechanisms in the active $p-$GaAs layer of this spin-LED, which is the topic of Chapter 5.

To conclude, we have outlined an approach for calculating the TiMMS spectral profiles of arbitrary semiconductor heterostructures. Although a detailed analysis of the system in question is necessary, this approach shows that it is possible to extract information from different layers from the general complicated TiMMS-spectra. This way, studies of spin relaxation mechanisms, transport and diffusion can be extended from model systems to complicated spintronic devices.

Bibliography

[1] H. Ebert, *Magneto-optical effects in transition metal systems*, Rep. Prog. Phys. **59** 1665-1735 (1996). 3.1.1

[2] F.L. Pedrotti, S.J. and L.S. Pedrotti, *Introduction to optics*, (Prentice Hall International Inc., New Jersey, 1996). 3.1.1

[3] B. Koopmans, *Laser-induced Magnetization Dynamics*, in Topics in Applied Physics Vol 87, (Springer: Berlin, 2003), p. 253-320. 3.1.2, 3.1.5, 3.2

[4] N. C. Gerhardt, S. Hövel, C. Brenner, M. R. Hofmann, F.-Y. Lo, D. Reuter, A. D. Wieck, E. Schuster, W. Keune, and K. Westerholt, *Electron spin injection into GaAs from ferromagnetic contacts in remanence*, Appl. Phys. Lett. **87**, 032502 (2005). 3.1.3

[5] A. Sinsarp, T. Manago, F. Takano, and H. Akinaga, *Electrical Spin Injection from Out-of-Plane Magnetized FePt/MgO Tunneling Junction into GaAs at Room Temperature*, Jpn. J. Appl. Phys., Part 2 **46**, L4 (2006).

[6] S. Hövel,1, N. C. Gerhardt, M. R. Hofmann, F.-Y. Lo, D. Reuter, A. D. Wieck, E. Schuster, W. Keune, H. Wende, O. Petracic, and K. Westerholt, *Electrical detection of photoinduced spins both at room temperature and in remanence*, Appl. Phys. Lett. **92**, 242102 (2008). 3.1.3

[7] V. F. Motsnyi, V. I. Safarov, J. De Boeck, J. Das, W. Van Roy, E. Goovaerts, and G. Borghs, *Electrical spin injection in a ferromagnet/tunnel barrier/semiconductor heterostructure*, Appl. Phys. Lett. **81**, 265-267 (2002). 3.1.3

[8] P. F. Carcia, A. D. Meinhaldt, and A. Suna, *Perpendicular magnetic anisotropy in Pd/Co thin film layered structures*, Appl. Phys. Lett. **47**, 178 (1985). 3.1.3

[9] H. J. G. Draaisma, W. J. M. de Jonge, and F. J. A. den Broeder, *Magnetic interface anisotropy in Pd/Co and Pd/Fe multilayers*, J. Magn. Magn. Mater. **66**, 351-355 (1987).

[10] P. F. Carcia, *Perpendicular magnetic anisotropy in Pd/Co and Pt/Co thin-film layered structures*, J. Appl. Phys. **63**, 5066 (1988). 3.1.3, 3.1.5

[11] M. T. Johnson, P. J. H. Bloemen, F. J. A. den Broeder, and J. J. de Vries, *Magnetic anisotropy in metallic multilayers*, Rep. Prog. Phys. **59** 1409-1458 (1996). 3.1.3

[12] P. V. Paluskar, J. T. Kohlhepp, H. J. M. Swagten, and B. Koopmans, *$Co_{72}Fe_{20}B_8$: Structure, magnetism, and tunneling spin polarization*, J. Appl. Phys. **99**, 08E503 (2006). 3.1.3

[13] J. Zak, E. R. Moog, C. Liu, and S. D. Bader, *Universal approach to magneto-optics*, J. Magn. Magn. Mater. **89**, 107-123 (1990). 3.1.4, 3.1.4

[14] J. Zak, E. R. Moog, C. Liu, and S. D. Bader, *Magneto-optics of multilayers with arbitrary magnetization directions*, Phys. Rev. B **43**, 6423-6429 (1991). 3.1.4, 3.1.4, 3.1.5

[15] P. Yeh, *Optical waves in layered media*, (Wiley & Sons, Inc, New York, 1988). 3.1.4, 3.4

[16] G. Malinowski, F. Dalla Longa, J. H. H. Rietjens, P. V. Paluskar, R. Huijink, H. J. M Swagten, and B. Koopmans, *Control of speed and efficiency of ultrafast demagnetization by direct transfer of spin angular momentum*, Nat. Phys. **4**, 855 (2008). 3.1.5

[17] J. H. Weaver, and H. P. R. Frederikse, *Optical properties of selected elements*, in Handbook of Chemistry and Physics, 88^{th} Edition, p. 12-120 - 12-144. 3.1.5, 3.4

[18] L. I. Berger, *Optical properties of selected inorganica and organic solids*, in Handbook of Chemistry and Physics, 88th Edition, p. 12-144 - 12-159. 3.1.5, 3.4

[19] R. Atkinson, S. Pahirathan, I. W. Salter, P. J. Grundy, C. J. Tatnall, J. C. Lodder, and Q. Meng, *Fundamental optical and magneto-optical constants of Co/Pt and CoNi/Pt multilayered films*, J. Magn. Magn. Mat **162**, 131-138 (1996). 3.1.5, 3.1.5

[20] C. Józsa, *Optical detection of the magnetization precession - choreography on a sub-nanosecond timescale*, Pd.D. Thesis, Eindhoven University of Technology, Eindhoven, The Netherlands (2006). 3.2

[21] W. K. Hiebert, A. Stankiewicz, and M. R. Freeman, *Direct Observation of Magnetic Relaxation in a Small Permalloy Disk by Time-Resolved Scanning Kerr Microscopy*, Phys. Rev. Lett. **79**, 1134 (1997) 3.2

[22] B. Koopmans, J. E. M. Haverkort, W. J. M. de Jonge, and G. Karczewski, *Time-resolved magnetization modulation spectroscopy: A new probe of ultrafast spin dynamics*, J. Appl. Phys. **85**, 6763 (1999). 3.3

[23] P. Van Dorpe, R. Vanheertum, H. Boukari, W. Van Roy, and G. Borghs, *Design of the tunnel contacts and the transport region of all-electrical spin-injection-detection devices*, J. Appl. Phys. **99**, 08S702 (2006). 3.12, 3.3.3

[24] J. M. Kikkawa, and D. D. Awschalom, *Resonant spin amplification in n-type GaAs*, Phys. Rev. Lett. **80**, 4313-4316 (1998). 3.3.3

[25] M. E. Flatté , and J. M. Byers, *Spin diffusion in semiconductors*, Phys. Rev. Lett. **84**, 4220-4223 (2000). 3.3.3

[26] S. A. Crooker, and D. L. Smith, *Imaging spin flows in semiconductors subject to electric, magnetic, and strain fields*, Phys. Rev. Lett. **94**, 236601 (2005). 3.3.3

[27] B. Koopmans, and W. J. M. de Jonge, *Ultrafast spin dynamics in magnetic semiconductor quantum wells studied by magnetization modulation spectroscopy*, Appl. Phys. B **68**, 525 (1999). 3.4, 3.4, 3.4

[28] S. Adachi, *Properties of Aluminium Gallium Arsenide*, (London: IEE, 1993). 3.4

[29] B. R. Bennett, R. A. Soref, and J. A. Del Alamo, *Carrier-Induced Change in Refractive Index of InP, GaAs, and InGaAsP*, IEEE J. Quantum Electron. **26**, 113-122 (1990). 3.4

Chapter 4

Effect of stray field on local spin modes in exchange-biased magnetic tunnel junction elements

We report on the detection of localized spin modes in a multilayered spintronic device by means of time-resolved scanning Kerr microscopy. Measurements on this 13×9 μm^2 exchange-biased magnetic tunnel junction element at different applied bias fields indicate a strong effect of the stray field from the pinned CoFe layer on the magnetization dynamics in the free NiFe layer. This view is supported by micromagnetic simulations, which also show that the dynamics can be attributed to the specific shape of the internal magnetic field in the element.[1]

[1]This Chapter is published as J. H. H. Rietjens, C. Józsa, H. Boeve, W. J. M. de Jonge, and B. Koopmans, *Effect of stray field on local spin modes in exchange-biased magnetic tunnel junction elements*, Appl. Phys. Lett. **87**, 172508 (2005)

4.1 Introduction

Magnetic tunnel junction (MTJ) elements are currently being implemented in spintronic devices, such as magnetic random access memory [1, 2]. Switching of the magnetization in the free ferromagnetic (FM) layer of a MTJ can be achieved by applying an external magnetic field (pulse) [3], and has to be fast and stable. Understanding the response of the magnetization in the free layer to an applied magnetic field (pulse) is therefore crucial for obtaining an optimal performance of the device. In recent years, the magnetization dynamics in relatively thick NiFe stripes and elements has been the subject of many studies [4–8], but so far no measurements on MTJs have been reported. In this chapter, we present spatiotemporal measurements and micromagnetic simulations of the magnetization dynamics in the free FM layer of an exchange-biased MTJ element. We show that this dynamic is strongly influenced by the stray field, H_{stray}, from the pinned FM layer of the MTJ.

4.2 Experimental details

4.2.1 The MTJ element

The MTJ element studied in this work was grown by sputter deposition and structured by etching, see Figs. 4.1(a) and 4.1(b). The Cu strip line (width 30 μm, thickness 17 nm) with contact pads at each end was deposited on a Si/SiO_2 substrate. The 13×9 μm^2 MTJ element, located at the center of the Cu line, consists of Ta and NiFe wetting layers, followed by an (IrMn 10 nm / $Co_{90}Fe_{10}$ 4 nm / Al_2O_3 1 nm / $Ni_{80}Fe_{20}$ 5 nm) stack and a 5 nm Ta capping layer. Superconducting quantum interference device measurements showed an exchange bias field of 31 kA/m acting on the CoFe layer and a 5 kA/m net FM coupling field H_{FM} between the NiFe and the CoFe layer. The direction of the exchange bias field (and thus the direction of H_{FM}) was set along the Cu line ($\hat{x}$ direction) by an in-field anneal treatment.

4.2.2 Measurement technique

The magnetization dynamics is triggered by magnetic field pulses $H_{pulse}(t)$ of ≈ 0.6 ns with $H_{pulse,max} \approx 1.2$ kA/m. These pulses are generated with an electronic pulse generator that is connected to the Cu line. The response of the magnetization in the free FM layer to such field pulses is typically a damped precessional motion. The local out-of-plane component of this response, $m_z(\vec{x}, t)$, is probed with time-resolved scanning Kerr microscopy, which is described in detail in Ref. [9]. An example of a time-resolved measurement is shown in Fig. 4.2.

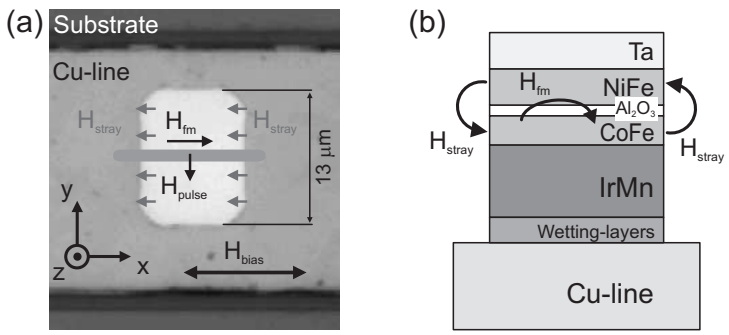

Figure 4.1: (a) Photograph of the 13×9 μm^2 MTJ studied in this work. Indicated are the coordinate system, the scanning line of Fig. 4.5 (gray), and the direction of H_{bias}, H_{pulse}, H_{FM}, and H_{stray}. (b) Schematic cross section of the MTJ.

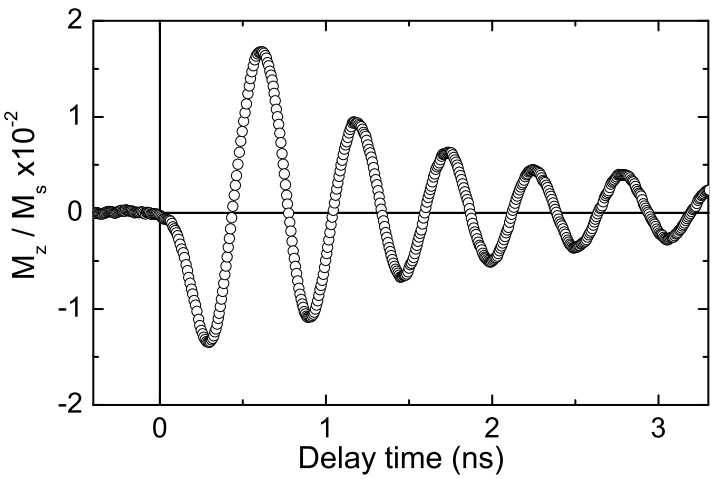

Figure 4.2: Typical measurement of $m_z(t)$ taken at the center of the MTJ at zero-bias field. A damped precessional motion with frequency 1.85 GHz can be observed.

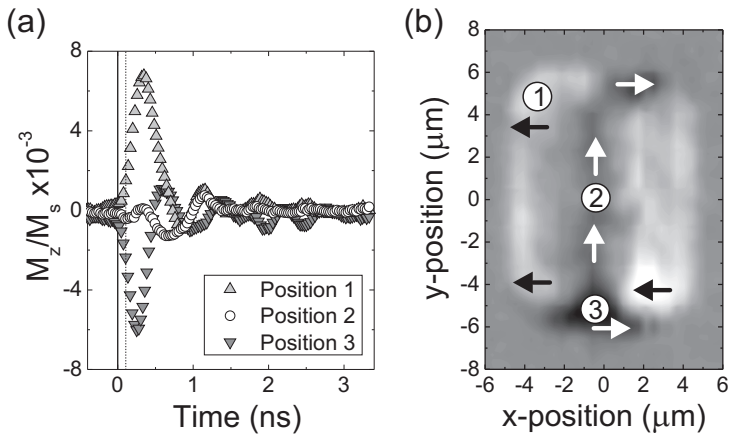

Figure 4.3: (a) Three measurements of the response of m_z to H_{pulse} at an external bias field of 5.0 kA/m. The numbered positions correspond to the positions indicated in (b). (b) Image of $m_z(\vec{x}, t = 0.1$ ns). The arrows indicate the main component of the local in-plane magnetization.

4.2.3 Micromagnetic simulations

Micromagnetic simulations of the magnetization dynamics were performed using the Object-Oriented MicroMagnetic Framework (OOMMF) [10]. The MTJ element is divided into a two-dimensional grid of 25 nm × 25 nm × 5 nm cells. Reduction of the cell size gave no different results. The material parameters used for the NiFe layer are $M_{s,NiFe} = 570$ kA/m, $\alpha = 0.01$, $A = 13 \times 10^{-12}$ J/m, where M_s is the saturation magnetization, α the Gilbert damping parameter, and A the exchange stiffness. The *dc* magnetic field in the simulation is the sum of the experimentally applied bias field H_{bias} and 5.0 kA/m representing H_{FM}. A magnetic field pulse with shape similar to the real pulse (rise/fall time 0.25 ns, plateau 0.1 ns) is used to excite the spin system. The response to this field pulse is calculated with a time step of 1 ps.

4.3 Results and discussion

4.3.1 Domain imaging

Let us first consider the experimental case with $H_{bias} = -5.0$ kA/m, i.e., the case when H_{FM} is fully compensated. The domain pattern in the free NiFe layer will then be the result of the interplay between the demagnetizing field H_{dem}, shape or crystalline anisotropy H_{ani}, and any remaining magnetic influence from the pinned layer. In this situation, no clear precessional motion of $\vec{m}(\vec{x}, t)$ could be observed in

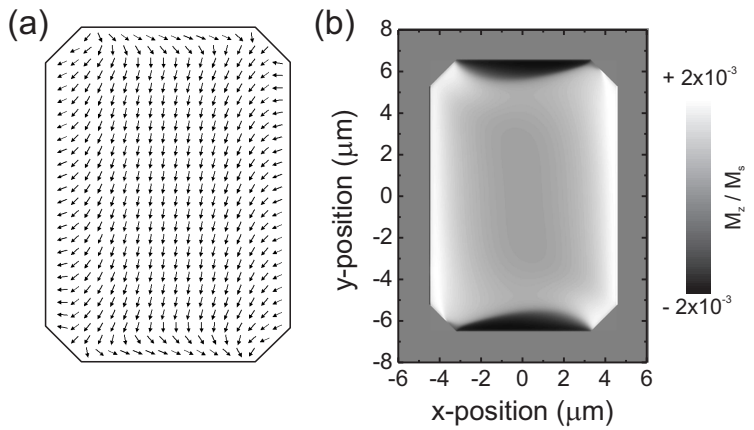

Figure 4.4: (a) Simulated equilibrium magnetization of the MTJ with $H_{bias} = 5.0$ kA/m. (b) Simulated image of $m_z(\vec{x}, t = 0.1$ ns).

time-resolved measurements [as can be seen in Fig. 4.3(a)], so no frequency analysis could be performed. Instead, we used the sign of $m_z(\vec{x})$ shortly after application of $H_{pulse}(t)$ to determine the static domain pattern $\vec{m}(\vec{x}, t = 0)$, as this sign is related to the orientation of $\vec{m}(\vec{x}, t = 0)$ by a torque equation, i.e., the well-known Landau-Lifshitz equation [11]. At Position 1, e.g., the sign of $m_z(t = 0.1$ ns) is positive, which implies that $\vec{m}(t = 0)$ at Position 1 has a large component in the negative $\hat{x}$ direction, since the effective field, $H_{eff} \approx H_{pulse}$, is in the $-\hat{y}$ direction. Similarly, a raster scan of the full element, taken at $t = 0.1$ ns after the onset of the magnetic field pulse, reveals the domain pattern in the free layer, as shown in Fig. 4.3(b). Notably, the magnetization is not aligned along the left- and right-hand side edges, in spite of the demagnetizing field. This suggests a contribution of the stray field H_{stray} from the pinned CoFe layer.

In order to investigate this, micromagnetic simulations of the experiment were performed with the incorporation of H_{stray}. For this purpose, at each cell, H_{stray} is calculated using the formula for the field of a uniformly magnetized element [12], with $M_{s,CoFe} = 1467$ kA/m, the bulk M_s value of CoFe [13]. The distance between the CoFe layer and the cells is set to 2.5 nm. The equilibrium magnetization of the free layer, after relaxing from a fully magnetized state, is shown in Fig. 4.4(a). The spins at the left/right-hand side edges are indeed oriented perpendicular to the edge, as a result of H_{stray}. Due to a small anisotropy present in the element (experimentally observed and included in the simulation), the magnetization is aligned along the $\hat{y}$ axis in the center of the element. Applying H_{pulse} to the initial magnetization state of Fig. 4.4(a), and calculating $m_z(\vec{x}, t = 0.1$ ns), results in the image shown in Fig. 4.4(b). A fair agreement between experiment and simulation can be observed,

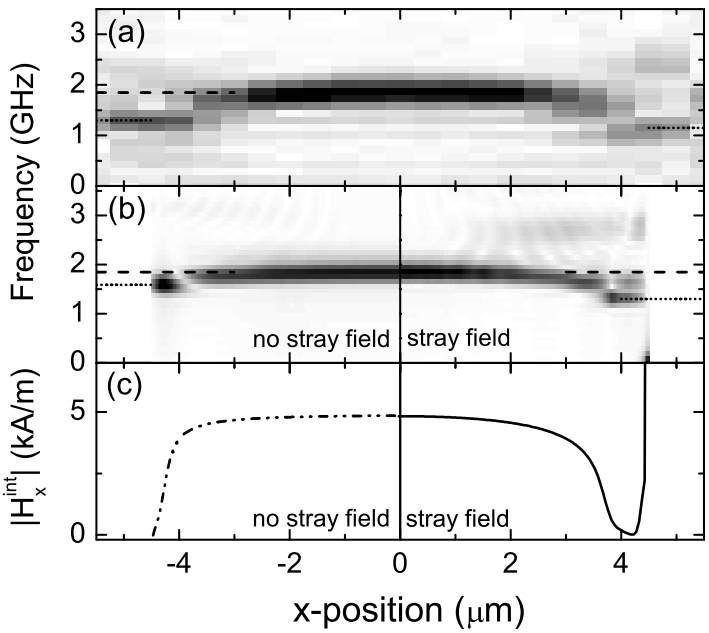

Figure 4.5: (a) Experimental spectral image of the line scan in the $\hat{x}$ direction with $H_{bias} = 0$ kA/m. (b) Simulated spectral image of the experiment of (a), without and with incorporation of a stray field. The gray scale in (a) and (b) represents the spectral power of the frequencies in $m_z(t)$, which is normalized at each position. The frequencies of the uniform (localized) modes are indicated with a dashed (dotted) line. (c) The magnitude of the internal magnetic field without and with stray field. The left- and right-hand side parts of (b) and (c) are symmetric in $\hat{x}$.

particularly with respect to the white (black) regions at the left/right (top/bottom) edges and the grey central region. These features are signs of the competition between the H_{stray}, H_{dem}, and H_{ani}. The difference in shape and position of the black regions between experiment and simulation is probably due to the absence of pinning centers in the simulation. These pinning centers are likely to be present in the real MTJ, e.g., due to edge roughness.

4.3.2 Local spin modes

When H_{bias} is set to 0 kA/m, the internal field at the center of the element is ≈ 5.0 kA/m. In this case, a precessional motion of $m_z(\vec{x}, t)$ can be observed, which allows for a frequency analysis. Therefore, $m_z(\vec{x}, t)$ has been measured locally along the $\hat{x}$ direction through the center of the element, see Fig. 4.1(a). Each measurement of

$m_z(t)$ is taken at fixed positions of the laser spot on the sample, in steps of 0.5 μm. The resulting Fourier transformation of $m_z(\vec{x}, t)$ at each position is shown in Fig. 4.5(a). A uniform precessional mode can be observed roughly from -3.5 to $+3.5$ μm, with a frequency, f_{uni}, that decreases from 1.85 GHz to 1.76 GHz when moving from 0 to ± 3.5 μm. At the edges of the element, a localized mode with $f_{loc} \approx 1.3$ GHz can be clearly seen. At $+4$ μm, a higher-order mode is also observed.

It has been shown [4, 5], that such remarkable localized modes can occur in a region where the internal magnetic field, H_{int}, is highly inhomogeneous. Such a region can arise near the edge of an element due to the demagnetization field, when an external field [or coupling field (H_{FM}) as in our experiment] is perpendicular to the edge. Spin waves propagating parallel to this field become confined in a potential well created by the inhomogeneous internal magnetic field, leading to a localized mode. The frequency of the localized mode depends on the precise shape of the potential well.

We performed micromagnetic simulations in order to calculate the frequency of the localized mode. The result of this simulation, without and with incorporation of H_{stray}, is shown in Fig. 4.5(b). The frequency of the uniform mode agrees well with the experiment in both simulations. However, both the gradual decrease of f_{uni} when moving from the center to the edge, and f_{loc} agree only in the case when H_{stray} is included. This can be understood by looking at the internal magnetic field in the element, see Fig. 4.5(c). The steep increase in H_{int} at ≈ 4.5 μm [Fig. 4.5(c) right-hand side part] is due to the strong stray field close to the magnetic pole of the CoFe layer. The gradual decrease of H_{int} between 0 and 3 μm is also due to the contribution of the stray field and results in the gradual decrease f_{uni}. Furthermore, H_{int} clearly behaves differently in the region where the localized mode is present, which results in a different shape of the potential well and a ≈ 0.3 GHz lower frequency of the localized mode. Around $+4$ μm, the simulated spectrum shows multiple peaks that do not correspond directly to the ones observed in the experiment. This fact, and the lack of symmetry in the experimental data (there is a 0.15 GHz difference between f_{loc} at the left- and right-hand side edge of the element) in contrast to the simulations, can be attributed to a slight difference in the internal magnetic field near the edges, as a result of sample imperfections.

We also measured and simulated f_{uni} and f_{loc} at different bias fields, as presented in Fig. 4.6. A good agreement between experiment, simulation, and theory can be observed for the uniform mode, which depends on H_{bias} according to

$$f_{uni} = \gamma \mu_0 \sqrt{(H_{bias} + H_{FM})(H_{bias} + H_{FM} + M_s)} \tag{4.1}$$

where γ is the gyromagnetic ratio and μ_0 is the magnetic permeability of vacuum. The dependence of f_{loc} on H_{bias} is similar to the one in the experimental case, but their absolute values are on average ≈ 0.16 GHz higher. This difference is comparable to the differences attributed to sample imperfections, so a satisfactory agreement between experiment and simulation is found when the stray field is included. More-

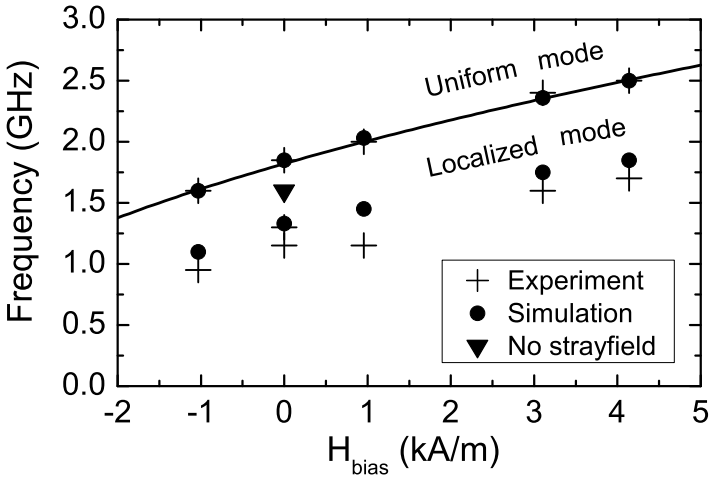

Figure 4.6: The frequency of the uniform and localized mode (experiment and simulation) as a function of the externally applied bias field. At 0 kA/m are shown the frequencies of the localized modes at both sides of the element (experimental) and from the simulation when no stray field is incorporated. The solid curve is the theoretical frequency of the uniform mode.

over, using a more realistic stray field, based on, e.g., a nonuniformly magnetized CoFe layer, might even improve these results.

4.4 Conclusion

The experimental data and the simulations indicate a strong effect of the stray field from the pinned CoFe layer on the magnetic behavior of the free NiFe layer. Most pronounced effects are the orientation of the magnetization at the edges when H_{FM} is compensated, and the low-frequency localized modes when H_{FM} is uncompensated. These observations can be explained by the specific shape of internal magnetic field in the element. In view of applications, it is necessary to reduce the effect of the stray field as much as possible. This will be specifically relevant when the size of the MTJ's is reduced to below 1 μm. Coherent precessional switching, e.g., may become impossible due to the presence of localized modes near the edges of the element.

Bibliography

[1] S. A. Wolf, D. D. Awschalom, R. A. Buhrman, J. M. Daughton, S. von Molnár, M. L. Roukes, A. Y. Chtchelkanova, and D. M. Treger, *Spintronics: A spin-based electronics vision for the future*, Science **294**, 1488-1495 (2001). 4.1

[2] B. N. Engel, J. Akerman, B. Butcher, R. W. Dave, M. DeHerrera, M. Durlam, G. Grynkewich, J. Janesky, S. V. Pietambaram, N. D. Rizzo, J. M. Slaughter, K. Smith, J. J. Sun, and S. Tehrani, *A 4-Mb toggle MRAM based on a novel bit and switching method*, IEEE Trans. Magn. **41**, 132 (2005). 4.1

[3] H. W. Schumacher, C. Chappert, R. C. Sousa, P. P. Freitas, and J. Miltat, *Quasiballistic magnetization reversal*, Phys. Rev. Lett. **90**, 017204 (2003). 4.1

[4] J. Jorzick, S. O. Demokritov, B. Hillebrands, M. Bailleul, C. Fermon, K. Y. Guslienko, A. N. Slavin, D. V. Berkov, and N. L. Gorn, *Spin Wave Wells in Nonellipsoidal Micrometer Size Magnetic Elements*, Phys. Rev. Lett. **88**, 047204 (2002). 4.1, 4.3.2

[5] J. P. Park, P. Eames, D. M. Engebretson, J. Berezovksy, and P. A. Crowell, *Spatially Resolved Dynamics of Localized Spin-Wave Modes in Ferromagnetic Wires*, Phys. Rev. Lett. **89**, 277201 (2002). 4.3.2

[6] A. Barman, V. V. Kruglyak, R. J. Hicken, and J. M. Rowe, *Imaging the dephasing of spin wave modes in a square thin film magnetic element*, Phys. Rev. B **69**, 174426 (2004).

[7] M. Buess, R. Höllinger, T. Haug, K. Perzlmaier, U. Krey, D. Pescia, M. R. Scheinfrein, D. Weiss, and C. H. Back, *Fourier Transform Imaging of Spin Vortex Eigenmodes*, Phys. Rev. Lett. **93**, 077207 (2004).

[8] K. Perzlmaier, M. Buess, C. H. Back, V. E. Edimov, B. Hillebrands, and S. O. Demokritov, *Spin-Wave Eigenmodes of Permalloy Squares with a Closure Domain Structure*, Phys. Rev. Lett. **94**, 057202 (2005). 4.1

[9] J. H. H. Rietjens, C. Józsa, H. Boeve, W. J. M. de Jonge, and B. Koopmans, *Probing local spin modes in exchange-biased MTJ elements*, J. Magn. Magn. Mater. **290**, 494-497 (2005). 4.2.2

[10] M. J. Donahue and D. G. Porter, *OOMMF User's Guide, version 1.0*, Interagency Report NISTIR 6376, NIST <http://math.nist.gov/oommf>. 4.2.3

[11] L. Landau and E. Lifshitz, *On the theory of the dispersion of magnetic permeability in ferromagnetic bodies*, Phys. Z. Sowjetunion **8**, 153 (1953). 4.3.1

[12] J. D. Jackson, *Classical Electrodynamics*, 3rd ed. (Wiley, New York, 1999), p. 196-197. 4.3.1

[13] Landolt-Börnstein, *Group III Condensed Matter* (Springer, Berlin, 1986), Vol. 19a, p. 189. 4.3.1

Chapter 5

Current-induced increase of the electron spin relaxation rate in a spin-LED

A microscopic time-resolved magneto-optical technique is used to investigate in detail the electron spin relaxation rate in a spin-LED under operational conditions. We have observed a current-induced decrease of the spin lifetime in the active region of the device, which scales linearly with the current and laser fluence. Device simulations and spectral measurements show that the main origin for this effect is an enhanced Bir-Aronov-Pikus (BAP) electron-hole spin flip scattering via an increased hole density and temperature in the active layer. We discuss the role of carrier recombination, and show that the effect persists outside the spin-LED, and scales roughly with the current and temperature distribution in the device.[1]

[1]A large part of this Chapter is in preparation for publication as J. H. H. Rietjens, C. A. C. Bosco, P. Van Dorpe, W. Van Roy, and B. Koopmans, *Current-induced increase of the electron spin relaxation rate in a spin-LED*

5.1 Introduction

Injection of spin-polarized electrons into semiconductors and their subsequent manipulation are essential ingredients for realizing functional semiconductor based spintronic devices [1]. One of the fundamental parameters influencing the device characteristics and efficiency is the spin relaxation time, τ_s. While most studies of τ_s have been performed on bulk or quantum semiconductor systems [2–8], detailed characterization of τ_s in the active part of real devices has received little attention so far. With the advance of spintronic devices, however, it has become of extreme relevance to understand the spin dynamics under variable operational conditions.

In this chapter, we study the spin relaxation rate of electrons in the active part of a spin-LED under operational conditions. We have performed detailed spectrally and spatially resolved experiments as a function of applied bias, laser fluence, and temperature. We have observed an enhanced spin relaxation rate, τ_s, of electrons at a current of 133 mA, which scales linearly with the injected current. We show that the main mechanism for this effect is an enhanced Bir-Aronov-Pikus electron-hole spin flip scattering as a result of an increased hole density and temperature in the active layer. This picture is supported by device simulations, which show that the increased hole density results from a band re-alignment in the device. Furthermore we discuss the role of laser photon energy, carrier recombination, and temperature on the observed effect. Finally, we show by detailed spatial scans that the enhanced spin relaxation rate persists outside the optical window, and scales roughly with a combined current and temperature distribution in the device.

5.2 Experimental details

5.2.1 Measurement technique

We have exploited a microscopic magneto-optical pump-probe technique, Time-resolved Magnetization Modulation Spectroscopy (TiMMS) (see Section 3.3) and Refs. [9] and [10]), to study the electron spin relaxation in the active region of a spin-LED. This technique measures the spin lifetime T_s, which is related to τ_s and the carrier recombination time τ_r via

$$T_s^{-1} = \tau_s^{-1} + \tau_r^{-1}. \tag{5.1}$$

In short, a circularly polarized pump pulse from a Ti:Sapphire laser (150 fs duration, 80 MHz repetition rate) is focused in the spin-LED (spot diameter ≈ 9 μm) and excites electron spins in the active region. A second, weaker probe beam is focused to an overlapping spot with a diameter of ≈ 4 μm, and probes the spin dynamics through the magneto-optical Kerr-effect. Due to the smaller spotsize of the probe compared to the pump, possible complications resulting from a spatially inhomogeneous carrier density are reduced. The relative time delay between pump

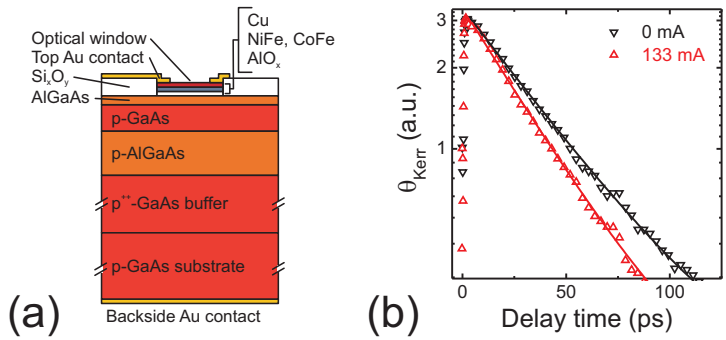

Figure 5.1: (a) Schematic cross-section of the spin-LED. (b) TiMMS time-scans for two different currents (0 and 133 mA) taken on LED1 at 292 K with a photon energy of 1.61 eV.

and probe pulse is controlled by a computer-interfaced variable delay line. We note that unlike electroluminescence [11–13], in which electrons and holes can only be detected upon recombination, and the spin relaxation rate is obtained in an indirect way, TiMMS allows for detailed temporal and spatial imaging of electron and hole spins separately.

5.2.2 The spin-LED

The spin-LEDs under investigation are similar to the one in Ref. [14] and have been shown to exhibit efficient electrical spin injection from a ferromagnetic (FM) metal into GaAs via an oxidic tunnel barrier [13, 15].

A schematic cross-section of the spin-LED is shown in Fig. 5.1a. The semiconductor heterostructure was grown on a (001) $p-$GaAs substrate and consists of a 2.75 μm $p-$GaAs buffer layer ($p = 2 \times 10^{19}$ cm^{-3}), 200 nm $p-$Al$_{0.30}$Ga$_{0.70}$As ($p = 1 \times 10^{18}$ cm^{-3}), 100 nm $p-$GaAs ($p = 1 \times 10^{18}$ cm^{-3}) active region and 20 nm Al$_{0.20}$Ga$_{0.80}$As (undoped). The highly doped buffer layer with short τ_r and τ_s was inserted to ensure that after $\approx$ 10 ps the only contribution to our measurements originates from the $p-$GaAs active region. This was confirmed by measurements on the buffer layer after removal of the top AlGaAs and $p-$GaAs layer from a separate sample by chemical wet etching, which showed $T_s \approx 6$ ps. A contribution of the substrate is only (weakly) present when the laser photon energy is close to the bandgap of GaAs (1.42 eV) [16], since in that case the penetration depth becomes very long due to the small absorption coefficient. The optical window consists of a 2 nm AlO_x tunnel barrier, a 2 nm $Co_{90}Fe_{10}$ and 8 nm $Ni_{80}Fe_{20}$ ferromagnetic layer and a 5 nm Cu top electrode. Au contacts enable application of a bias, while the 80 $\times$ 80 μm^2 window allows for optical access. More details of the fabrication

process can be found in Ref. [15].

During the TiMMS-measurements, part of the laser light is absorbed by the metallic layers, but any signal from optical spin injection or transient magneto-optics in the FM layer is absent since the magnetization of the FM layer is in-plane and perpendicular to the wave propagation. The $Al_{0.20}Ga_{0.80}As$ film (E_{gap} = 1.67 eV [17]) is transparent for most of our laser photon energies used, and does not interfere in our measurements. Also, we estimate that the local temperature rise of the $p-$GaAs active region due to absorption of a single pulse is less than 0.5 K, and that the DC heating of the $p-$GaAs active region due to laser absorption is less than 0.1 K.

5.3 Results and Discussion

5.3.1 Current-induced enhancement of the spin relaxation rate

Typical TiMMS-measurements, taken at room temperature on the optical window with a laser photon energy of 1.61 eV, a laser fluence of $F = 42$ μJ/cm^2, and a current of $I = 0$ mA and $I = 133$ mA are shown in Fig. 5.1. For further reference, we refer to this spin-LED as "LED1". Fitting this data starting at $\Delta t = 10$ ps with a single exponential decay yields T_s, and we obtain $T_{s,0mA} = 42$ ps and $T_{s,133mA} = 34$ ps. A decrease in T_s by 19 % is thus observed when the current is increased from $I = 0$ to $I = 133$ mA. We note that a decrease of T_s by $15 - 30\%$ has been observed for several spin-LEDs with typical laser fluences. Assuming for the moment that the carrier recombination time τ_r is much larger than the spin scattering time τ_s, it follows that $T_s = \tau_s$, and the results can be interpreted as a current induced decrease of τ_s.

To explore this current induced effect in more detail, we have performed measurements of the electron spin relaxation rate T_s^{-1} as a function of current (with constant laser fluence), and as a function of laser fluence (with constant current). These measurements were taken (again) with a laser photon energy of 1.61 eV, and are displayed in Fig. 5.2. We note that these measurement were taken on another, though similar spin-LED ("LED2"), but that the measured value of T_s^{-1} at $I = 0$ mA agrees very well with that from LED1 for the corresponding fluence. However, for this particular spin-LED, the enhancement in spin relaxation rate is higher (31% at a current of $I = 133$ mA, and a fluence of 42 μJ/cm^2) than with LED1 (19%). In Fig. 5.2 a linear dependence of T_s^{-1} on both current and laser fluence is observed. Because both the current and the laser fluence are expected to increase the hole density in the active region, Fig. 5.2 suggests that an increased hole density is responsible for the increased electron spin relaxation rate, and that T_s^{-1} scales linearly with the hole density in the active region. A mechanism which fits this behavior is the Bir-Aronov-Pikus electron-hole spin-flip scattering mechanism, since

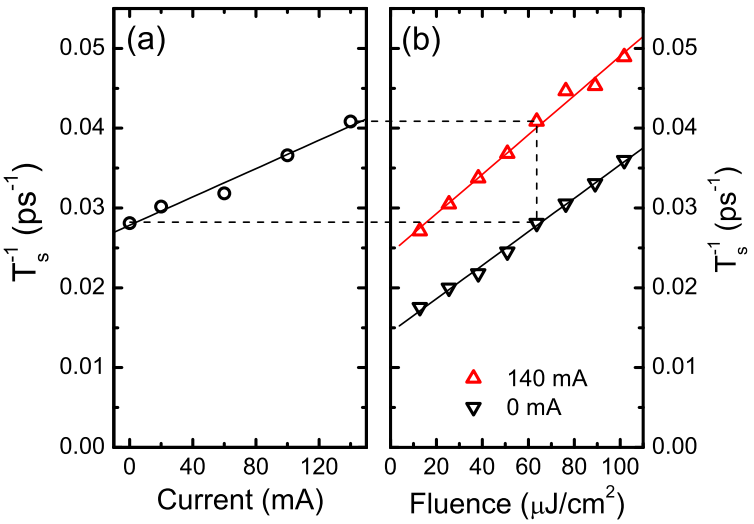

Figure 5.2: (a) Current dependence of the electron spin relaxation rate in the active region of LED2, taken at a laser fluence of 64 μJ/cm^2. (b) Laser-fluence dependence of the electron spin relaxation rate in the same region at current of 0 mA ($\bigtriangledown$) and 140 mA ($\bigtriangleup$). All data is taken at room temperature with a laser photon energy of 1.61 eV.

for this mechanism the spin relaxation rate scales linearly with the hole density for non-degenerate holes [3].

A simple model to correlate the current and fluence dependence

We can apply a simple model to estimate the increase in hole density in the active region of the spin-LED under operational and experimental conditions. Assuming a homogeneous electron and hole density (flat bands), and a linear increase of τ_s^{-1} with the hole density in the active region (only a BAP-contribution to the electron spin relaxation), it follows that

$$\begin{aligned} T_s^{-1} \approx \tau_s^{-1} &= (\tau_{s,0} p_0)^{-1} \left(p_0 + p_I(I) + p_F(F)\right) \\ &\approx (\tau_{s,0} p_0)^{-1} \left(p_0 + I\frac{dp_I(I)}{dI} + F\frac{dp_F(F)}{dF}\right) \end{aligned} \tag{5.2}$$

where p_0 is the intrinsic hole density due to doping (1×10^{18} cm^{-3}), p_I and p_F are the electrically and optically injected hole densities, respectively, I is the current, and F is the laser fluence. Without bias ($V = 0$ V, $I = 0$ mA) and laser fluence ($F = 0$), we extract from Fig. 5.2b $\tau_{s,0}^{-1} = 0.0144$ ps^{-1} ($\tau_{s,0} = 70$ ps). Using a linear fit of the data of Fig. 5.2a , and 5.2b, we find

$$\frac{dp_I(I)}{dI} \approx 4.9p_0 \text{ A}^{-1}, \qquad \text{and} \qquad \frac{dp_F(F)}{dF} \approx 0.015p_0 \text{ cm}^2\mu\text{J}^{-1},$$

respectively. We can compare these values with an estimation of the injected current- and laser-induced hole densities from experimental parameters:

$$\frac{dp_I(I)}{dI} \approx \frac{\tau_r}{Ad}, \qquad \text{and} \qquad \frac{dp_F(F)}{dF} \approx \frac{f_{abs}}{\hbar\omega d}.$$

Here, A is the surface area of the spin-LED, d is the thickness of the active region, f_{abs} is the fraction of the fluence that is absorbed in the active region, and $\hbar\omega$ is the laser photon energy. We assume that the induced hole density is equal to the induced electron density, which is certainly true for optical injection, but is less trivial for electrical injection because of possible hole tunneling from the semiconductor to the FM layer. With $\hbar\omega = 1.61$ eV we calculated $f_{abs} = 0.044$, and using $\tau_r = 273$ ps, we find

$$\frac{dp_I(I)}{dI} \approx 2.7p_0 \text{ A}^{-1} \qquad \text{and} \qquad \frac{dp_F(F)}{dF} \approx 0.017p_0 \text{ cm}^2\mu\text{J}^{-1}.$$

We observe a fair agreement for dp_F/dF with our simple model, which supports our assumption that the BAP-mechanism is responsible for the enhanced spin relaxation rate via an increased hole density. We shall discuss the somewhat higher discrepancy for dp_I/dp and our choice for the recombination time in due course. In this analysis we neglected the fact that the slopes in Fig. 5.2b at $I = 0$ mA and $I = 140$ mA are slightly different. This indicates a stronger fluence dependence of T_s^{-1} at higher current, and a weaker current dependence of T_s^{-1} at high fluence. We note that the relative current induced contribution to T_s^{-1} is highest at zero fluence, i.e. extrapolating the results of Fig. 5.2b to zero fluence yields a current induced effect of 40% at 140 mA.

Device simulation

In order to explore the physical picture of the enhanced electron spin relaxation rate in more detail, we performed simulations of the band alignment and the carrier profile in the spin-LED using the MEDICI software package [18] (see the Appendix for a comparison of the experimentally and simulated current-voltage characteristics). Figure 5.3 shows the band diagram, and carrier profiles at 0 V and 2.4 V (corresponding to $I = 0$ mA, and $I = 163$ mA). At zero bias, band bending near the $p-$GaAs/$Al_{0.20}Ga_{0.80}$As interface results in a sharp drop of the hole concentration near this interface, and in a strong local electric field. Optically injected electrons will reside near the $p-$GaAs/$Al_{0.20}Ga_{0.80}$As interface, and experience a low spin-flip scattering with holes due to the low local hole concentration. For high bias, the active region is pulled flat, and the hole concentration increases from 8.6×10^{17} cm^{-3} to approximately 9.8×10^{17} cm^{-3} throughout the whole device. This increase results mainly from an increase in electron density (1×10^{17} cm^{-3}) in the active region, where the additional hole density ensures charge neutrality. Since the electrons

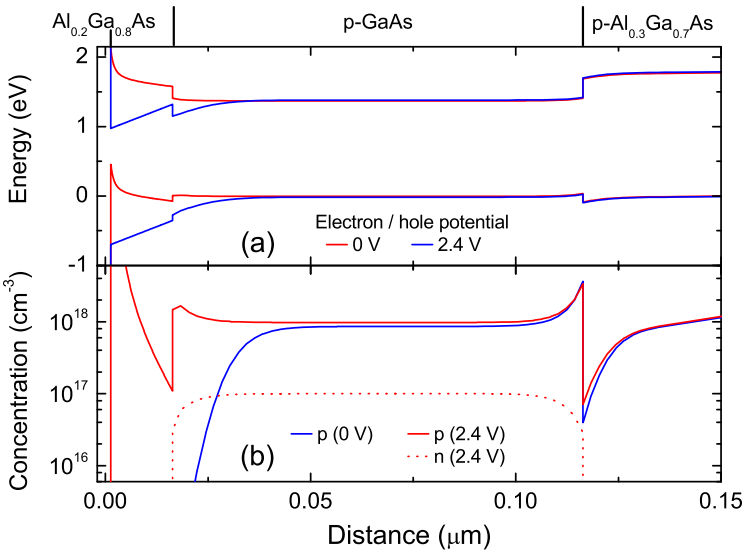

Figure 5.3: (a) Band diagram at 0 and 2.4 V in the spin-LED at 300 K. (b) Hole (p) and electron (n) concentration for 0 and 2.4 V in the spin-LED at 300 K. At 0 V, the electron concentration is below 10^{13} in the region shown.

and holes are not separated, the spin relaxation rate will increase as the electrons experience an increased hole density, in agreement with Fig. 5.2a.

These simulations also explain the fluence dependence of the electron spin relaxation rate. Laser induced free charges ($\approx 0.017 \times 10^{18}$ cm$^{-1}\mu$J^{-1}) can pull the active region flat by screening the built-in electric field, and increase the hole density accordingly. The electrons will experience a larger hole concentration, and their spin lifetime will decrease by the BAP mechanism. We note that at this current ($I = 163$ mA), the increase in hole density corresponds to $dp_I/dp = 1.85p_0$ A^{-1}, which is comparable to our simple estimation according to Eq. 5.2, but also lower than the value extracted from Fig. 5.2.

5.3.2 Other current induced effects

Up to now we have seen strong evidence that the current-induced enhancement of the spin relaxation rate results from an enhanced spin-flip scattering via the BAP mechanism due to an increased hole density. However, so far we have not discussed the potential influence on T_s of a current-induced change of the temperature, and recombination rate. If present, a current-induced decrease of τ_r leads via Eq. 5.1 to a current-induced decrease of T_s. A current-induced increase of the temperature of the spin-LED leads via the BAP-mechanism (see Eq. 2.10) to a current-induced

decrease of τ_s. According to Fig. 5.10b the dissipated power in the spin-LED is only weakly non-linear. As the increase in temperature scales linearly with the dissipated power, the signature of a current-induced temperature rise might be similar to that of a current-induced hole density.

In this Section we will discuss the role of recombination, and temperature in more detail. It will become clear that the BAP-mechanism also reduces the spin relaxation time via a temperature increase, and that only part of the current induced decrease of T_s can be attributed to a non-constant carrier recombination rate. We start with discussing spectral measurements of the current-induced effect.

Spectroscopic TiMMS data

The TiMMS-data presented so far have all been taken at a laser photon energy of 1.61 eV. Results from spectroscopic measurements, with laser photon energies between 1.47 and 1.69 eV, and taken at a current of both 0 mA and 133 mA, are presented in Fig. 5.4. We see that T_s depends strongly on the laser photon energy, when using a single exponential fit to the data starting at $\Delta t = 10$ ps. The divergence of T_s is related to a zero crossing of the amplitude of the TiMMS-signal, see Fig. 5.4(b), which displays the amplitude of the TiMMS-signal at $\Delta t = 5$ ps. The position of this zero crossing is very sensitive to the carrier density in the device, and therefore time-dependent in our experiment due to carrier recombination.

We performed simulations of the TiMMS-time traces versus photon energy following the approach of Koopmans *et al.* [10] taking into account this time-dependent zero-crossing, the absorption profile, and depth dependence of the magneto-optical Kerr-effect [19] (discussed in detail in Sections 3.1.4 and 3.4). The simulated time-traces are also fitted with a single exponential decay in order to extract $T_{s,sim}$, yielding the lines shown in Fig. 5.4. Using $\tau_s = 41$ ps, and $\tau_r = 390$ ps, we can nicely match the experimental data at $I = 0$ mA. The range in τ_s and τ_r which give a reasonable match are ($\tau_s = 39$ ps, $\tau_r = 480$ ps) to ($\tau_s = 43$ ps, $\tau_r = 300$ ps). In order to simulate the data at $I = 133$ mA, we have to take into account a decrease in τ_s and/or a decrease in τ_r, and also a spectral redshift of the TiMMS spectrum of 7.5 meV. This redshift is experimentally observed (see Fig. 5.4b), and is attributed to a shift of the band-gap due to current-induced heating of the device. The data at $I = 133$ mA is simulated for the cases of a decrease of (i) only τ_r (ii) only τ_s, and (iii) both τ_s and τ_r, as shown in Fig. 5.4. In each case, values for $\Delta\tau_r$ and $\Delta\tau_s$ are chosen such that ΔT_s is consistent with the experimental data at low and high photon energy. We see that the data can only be well matched at every photon energy if a decrease of τ_s is taken into account, but also that a decrease in τ_r cannot be excluded. We note that direct measurements of τ_r are in principle possible by measuring the carrier dynamics in the active layer via the transient reflectivity. However, the interpretation of such measurements performed on the optical window of the spin-LED proved less trivial. Due to complications related to the semiconductor heterostructure, such as contributions from other layers, heating

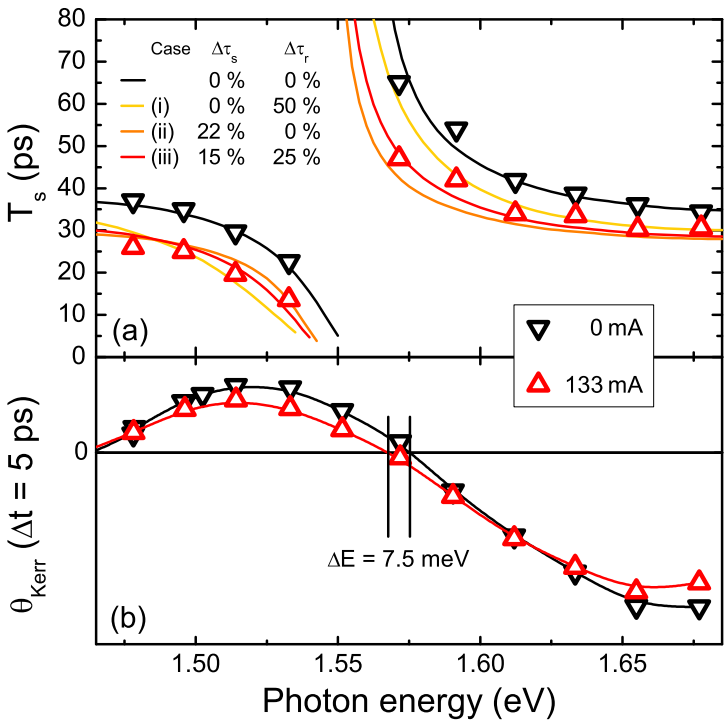

Figure 5.4: (a) Time constants T_s of a single exponential fit of the TiMMS measurements as a function of laser photon energy, taken at room temperature on LED1, with $F = 42$ μJ/cm^2, and $I = 0$ mA ($\bigtriangledown$) and $I = 140$ mA ($\bigtriangleup$). The solid lines are the results of a simulation of the measurement data and the fitting procedure. (b) The amplitude of the TiMMS-signal with $\Delta t = 5$ ps, taken at room temperature, with $F = 60$ μJ/cm^2, and $I = 0$ mA ($\bigtriangledown$) and $I = 140$ mA ($\bigtriangleup$). Solid lines are guides to the eye.

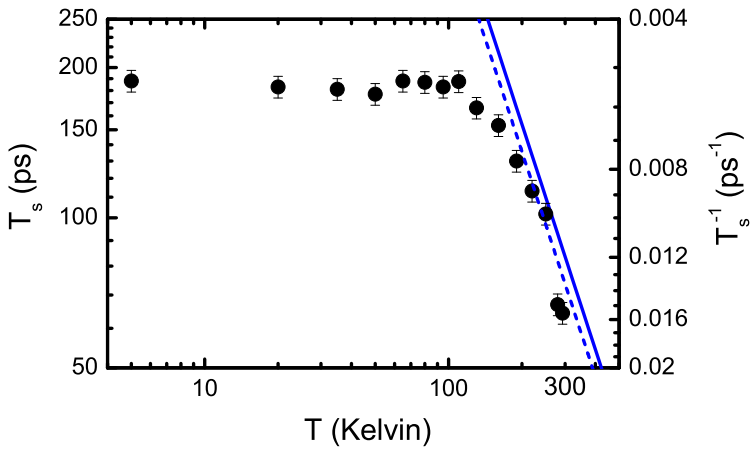

Figure 5.5: Temperature dependence of the spin lifetime T_s with $F = 27\ \mu\text{J/cm}^2$. The lines represent the theoretical predictions (no fit) according to $\tau_s = 1/(2.3 \cdot p^{1/3}T^{3/2})$ (equation 16a in ref. [3]) with $p = 1 \times 10^{18}\ \text{cm}^{-3}$ (solid line, without laser contribution), and $p = 1.46 \times 10^{18}\ \text{cm}^{-3}$ (dashed line, with laser contribution).

and corresponding time dependent thermal expansion of the layers, and a strong photon energy dependence, we could not unambiguously extract τ_r.

The role of recombination

Let us take a look at the implications of a current-induced decrease of τ_r. First of all, a current-induced decrease of τ_r fits well within the picture given by the device simulations, as a spatial separation of electron and holes should lead to a high τ_r at low current, and to a lower τ_r at high current when this separation vanishes. We note that in case (iii) $\tau_r = 273 \pm 63$ ps, which is in good agreement with values for τ_r above luminescence threshold obtained at IMEC [20]. A current-induced decrease of τ_r therefore seems reasonable. However, the effect of this decrease on T_s is very limited when $\tau_r \gg \tau_s$. If we take for example the values for τ_r for case (iii) of Fig. 5.4, we have $\Delta\tau_r = 30\%$. With $\tau_s = 42$ ps, this decrease of τ_r leads to a decrease of T_s of only $\Delta T = 3.9\%$. A much larger current-induced decrease of τ_s of 16% is then necessary in order to explain the full current-induced decrease of T_s. Thus although a current-induced decrease in τ_r is experimentally observed and in agreement with device simulations, it cannot explain the full current-induced decrease of T_s.

The role of temperature

We performed TiMMS measurements as a function of temperature on LED2, and extracted T_s as shown in Fig. 5.5. At low temperatures, the plateau most likely

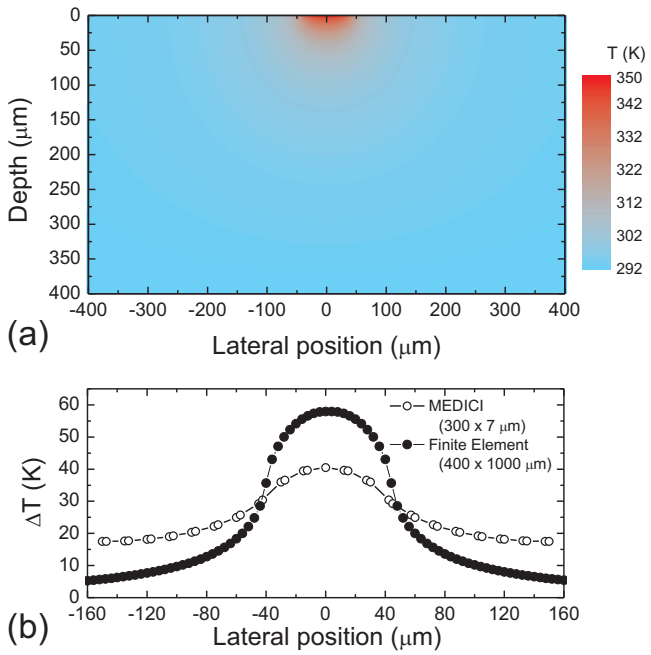

Figure 5.6: (a) Finite element calculation of the temperature distribution in the spin-LED when all energy is dissipated in the active region. (b) Profiles of the temperature rise in the active region according to the finite element calculation (solid circles), and the MEDICI simulation (open circles).

indicates a recombination limited spin lifetime, such that $T_s \approx \tau_r < \tau_s$. Above 150 K we have $T_s \approx \tau_s$, and a decreases of τ_s with temperature is observed. We can compare these data with the results of Aronov *et al.* [3], who found $\tau_s = 1/(2.3 \cdot p^{1/3}T^{3/2})$ (see Section 2.3), consistent with BAP-theory. Using $p = 1.46 \times 10^{18}$ cm^{-3}, and $p = 1 \times 10^{18}$ cm^{-3}, for the case with and without laser contribution, respectively, we obtain the lines as shown in Fig. 5.5. An excellent agreement with the experimental data is observed, confirming that BAP is the dominant spin relaxation mechanism in this device. Note that T_s at 292 K is different from T_s in Fig. 5.4, due to the lower fluence used. We can relate the observed shift of the TiMMS spectrum of 7.5 ± 0.5 meV, and corresponding band-gap shift of the same magnitude, to a temperature rise by using the Varshni-formula for the temperature dependence of the band-gap of GaAs [21]:

$$E_g = 1.519 - \frac{5.405 \cdot 10^{-4} T^2}{T + 204} \qquad (E_g \text{ in eV}, T \text{ in K}) \tag{5.3}$$

With $\Delta E_g = 7.5 \pm 0.5$ meV, Eq. 5.3 yields $\Delta T = 17 \pm 1$ K.

We can compare this ΔT with the results of the MEDICI-simulation (300 μm $\times$ 7 μm 2D-grid), and a simple finite element calculation (FEC) (cylindrical 2 mm $\times$ 400 μm quasi 3D-grid), of the temperature distribution in the spin-LED. In the FEC it is assumed that all electrical energy ($P = 0.32$ W with $V = 2.4$ V, and $I = 0.133$ A) is dissipated in the active layer under the optical window in the semiconductor. The boundary condition for the back-contact is $T = 292$ K, whereas all other boundaries have Neumann-conditions with no heat transfer. Therefore, the calculated ΔT can be regarded as an upper limit for the current-induced temperature rise. The values for the thermal conductivity of each layer were taken from literature [16, 17]. We used a cylindrical geometry and calculated the equilibrium temperature on an appropriate mesh of height 0.4 mm and radius 1 mm. The result is shown in Fig. 5.6, from which a maximum temperature rise under the optical window of several tens of Kelvin is observed. The differences between the MEDICI and the FEC calculation most likely originate from the different grid sizes used. These simulations indicate that experimentally observed temperature rise of ≈ 17 K is reasonable. According to Fig. 5.5, the increase in temperature of $\Delta T \approx 17$ K corresponds to a decrease of T_s of $\approx 8\%$. From this observation we conclude that a current-induced temperature rise also contributes to the decrease of T_s, however, it is too small to account for the full observed effect.

We now return to the apparent discrepancy between the measured dp_I/dp using our simple model and the estimation from experimental parameters. From Fig. 5.4 we have observed that the current-induced decrease of T_s is best described by a current-induced decrease of τ_s somewhere between 15% (case (iii)) and 22% (case (ii)). Of this $15 - 22\%$, we have seen that $\approx 8\%$ is due to the temperature rise. The estimation of dp_I/dp should thus also include the effect of temperature, which yields $4.2p_0 < dp_I/dp < 5.7p_0$. Now a good agreement with the simple model is observed. Summarizing, the observed current-induced decrease of T_s is mainly caused by a decrease of τ_s, and partly due to the effect of a reduced τ_r. The current-induced decrease of τ_s is mediated by the BAP-mechanism, partly via an increased hole density and partly via a temperature rise.

5.3.3 Spatially resolved measurements

We have determined the spatial extent of the current-induced effect by performing detailed spatially resolved measurements on LED1 at 0 A and 133 mA. Figure 5.7 shows the extracted current-induced decrease of T_s as a function of position on the line scan over the spin-LED (see right inset, showing a reflection image of the spin-LED). The left inset shows a camera picture of the same spin-LED at $I = 133$ mA with the luminescence clearly visible. The magnitude of the current-induced effect is on average constant in the optical window ($\approx 19\%$, the same as in Fig. 5.1(b)), but decreases in the surroundings with the distance to the optical window. As stated

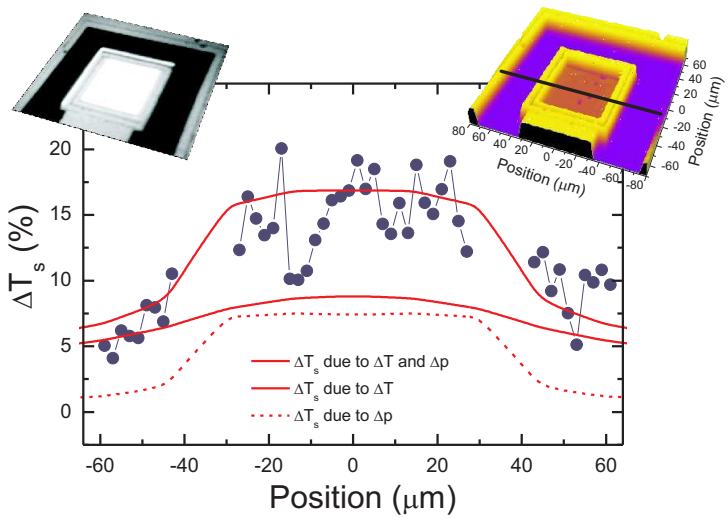

Figure 5.7: The current-induced effect ΔT_s versus position on a line scan across the spin-LED (see reflection image in right inset), extracted from measurements taken at 292 K, with a laser photon energy of 1.66 eV, and $F = 42$ μJ/cm^2. The left inset shows a camera picture of the light emitted by same spin-LED at $I = 133$ mA. The solid lines correspond to the calculated total ΔT_s, and the separate contribution to ΔT_s of the hole density and temperature.

above, the current-induced effect should scale with the hole density and temperature in the active region. From the 2D MEDICI simulation, we have extracted the lateral hole density and temperature profile. We have converted these profiles to a current-induced decrease of T_s, after accounting for the laser induced hole density, and scaling of the temperature profile to match the observed $\Delta T = 17$ K. In Fig. 5.7, the total, as well as the separate contributions of hole density, and temperature, are plotted. A fair agreement is observed with the experimental data, confirming the combined action of temperature and hole density on ΔT_s. This result also shows that the current-induced effect outside the spin-LED is dominated by the effect of a temperature rise.

5.4 Conclusion

In summary, we have used microscopic TiMMS to investigate the electron spin dynamics in the active region of a spin-LED under operational conditions. A current-induced decrease of the spin lifetime is observed that scales almost linearly with current and laser fluence. Detailed TiMMS measurements as a function of laser photon energy, temperature, and position suggest that the reduced spin lifetime

mainly originates from a current-induced decrease of the spin relaxation time, and partly from a current-induced reduction of the recombination time. The decrease of the spin relaxation time is mediated by an enhanced BAP electron-hole spin-flip scattering via an increased hole density and temperature. This view is supported by device simulations of the carrier, and temperature profile. These simulations show that the effective hole density in the active region increases due to a band realignment and increased electron density, and that the spatial extent of the effect is in good agreement with the lateral current-induced increase in hole density and temperature. These results show that the combination of time, spectrally, and spatially resolved experiments in realistic spintronic devices offers great opportunities for improving our understanding of spin dynamics phenomena under operational conditions. However, a detailed analysis of the data is needed in order to obtain valuable information from non-trivial semiconductor heterostructures.

5.5 Appendix

In this Appendix we show the actual measurement data from which some results in the main part of this chapter have been extracted. First, we focus on the spectral TiMMS-data, and we will discuss in more detail some of the modeling that has been performed in order to explain the data of Fig. 5.4. Second, we show the detailed spatially resolved TiMMS-data, from which the data in Fig. 5.7 was extracted. Finally, we compare the measured current-voltage characteristic of the spin-LED with the one obtained from the MEDICI-simulation.

5.5.1 Spectral measurements

In Fig. 5.8a we present the experimental TiMMS time-traces for different laser photon energies, obtained at room temperature, with $I = 0$ mA and $F = 42$ μJ/cm^2. A sign change of the TiMMS-signal is observed around 1.55 eV, similar to the data in Fig. 5.4b (the zero-crossing in Fig. 5.4b occurs at a slightly higher energy because the laser fluence is slightly higher). A peculiar time-trace we want to focus on, is the one indicated by the small arrow. This particular measurement shows an initial increase of the TiMMS-signal due to spin orientation by the pump pulse. However, instead of a single exponential decay towards zero signal, it shows a decrease of the signal to negative values within a few tens of ps. It reaches a maximum negative signal at $\Delta t = 35$ ps, which is followed by a decay back to zero signal at longer time delays. When such data are fitted with a single exponential decay, it can lead to either very short or very long decay times, resulting in the asymptotic behavior observed near the zero-crossing in Fig. 5.4a. This non-single exponential decay is the result of a summation of different contributions to the total signal from different parts (depth's) of the $p-$GaAs active region. Recalling Fig. 3.21c, we see that the TiMMS-signal originating from the first (last) ≈ 50 nm is negative (positive) for

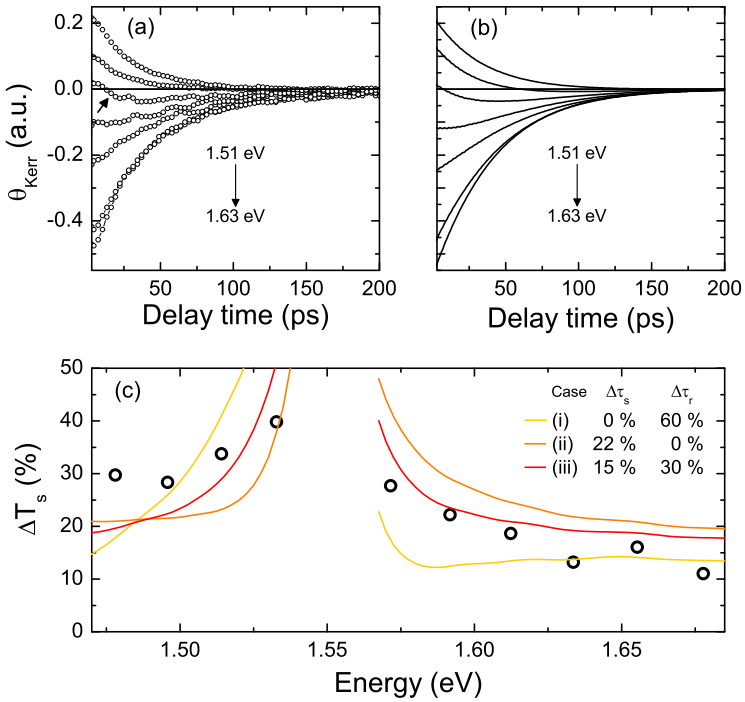

Figure 5.8: TiMMS time-scans versus laser photon energy, taken at 292 K, with $I = 0$ mA, $F = 42\ \mu$J/cm^2. (a) Time-scans from experiment. (b) Time-scans from simulation. (c) ΔT_s obtained from single exponential fits of the experimental (open circles) and simulated (solid lines) time-scans with $I = 0$ mA and $I = 133$ mA (see also Fig. 5.4a).

$E_{ph} < 1.51$ eV, and positive (negative) for $E_{ph} > 1.51$ eV. The total TiMMS-signal from the $p-$GaAs active region is thus effectively the sum of single exponential decays with different positive and negative amplitudes. However, a summation of single exponential decays with different amplitudes, but the same time-constant, will still be a single exponential decay, and not lead to the behavior observed in Fig. 5.8a. It is the finite recombination time of the excited carriers that leads to this behavior. Due to recombination, the carrier density in the $p-$GaAs active layer is time-dependent, and therefore also the TiMMS spectral shape is changing with the pump-probe delay time. In particular, the position of the zero-crossing will shift to lower energies, according to Fig. 3.22a. Starting e.g. with a carrier density of $n_e = 6.3 \cdot 10^{18}$ cm^{-3}, with a laser photon energy of 1.55 eV, the zero-crossing is at 1.56 eV, and the TiMMS-signal is positive. If at larger time-delays the carrier density has decreased due to recombination to e.g. $n_e = 5 \cdot 10^{18}$ cm^{-3}, the zero-crossing has shifted to 1.53 eV, and the TiMMS-signal is negative. Using the calculated

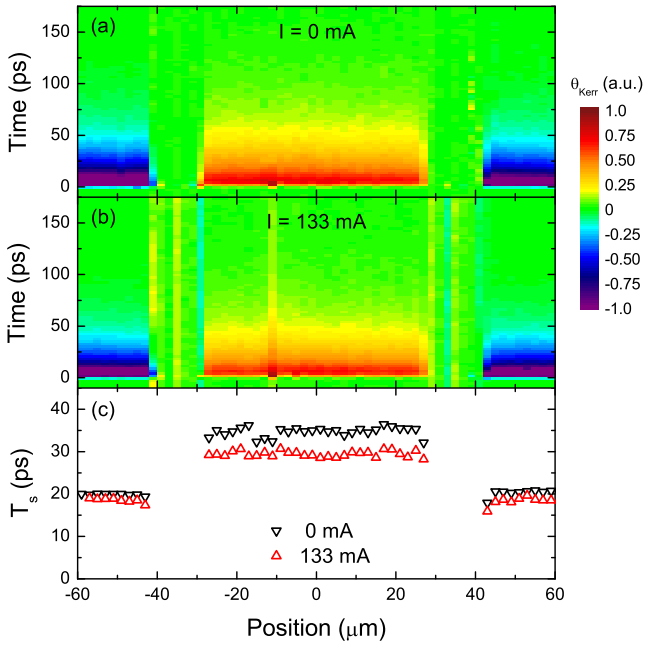

Figure 5.9: TiMMS time-scans versus position on a line scan across the spin-LED, taken at 292 K, with a laser photon energy of 1.66 eV, and $F = 42\ \mu\text{J/cm}^2$. (a) Time-scans taken with $I = 0$ mA. (b) Time-scans taken with $I = 0$ mA. (c) Time-constants of a single exponential fit of the data in (a) and (b).

TiMMS-spectrum as a function of carrier density, i.e. $T_{p-GaAs}(E_{ph}, n_e)$ from Fig. 3.22a, we can model the complete time-response for each laser photon energy, via

$$\theta_K(E_{ph}, t) = T_{p-GaAs}\left(E_{ph}, n_e(t)\right) \cdot \exp(-t/\tau_s) \tag{5.4}$$

$$n_e(t) = n_{e,0} \exp(-t/\tau_r). \tag{5.5}$$

Here, only the initial carrier density $n_{e,0}$, and a single (constant) value for τ_s and τ_r are the input parameters. Some of the calculated time-traces are shown in Fig. 5.8b. Indeed, an excellent agreement is observed with the experimental data of Fig. 5.8a, when using $\tau_s = 41$ ps, and $\tau_r = 390$ ps.

The current-induced change of the time-resolved signal as a function of laser photon energy is modeled the same way, with reduced values for τ_s and/or τ_r for three different cases as explained in Section 5.3.2. For completeness, we plot in Fig. 5.8c the current-induced decrease T_s for these three cases as a function of laser photon energy. Also from this Figure we can conclude that cases (ii), and (iii) are the most realistic ones.

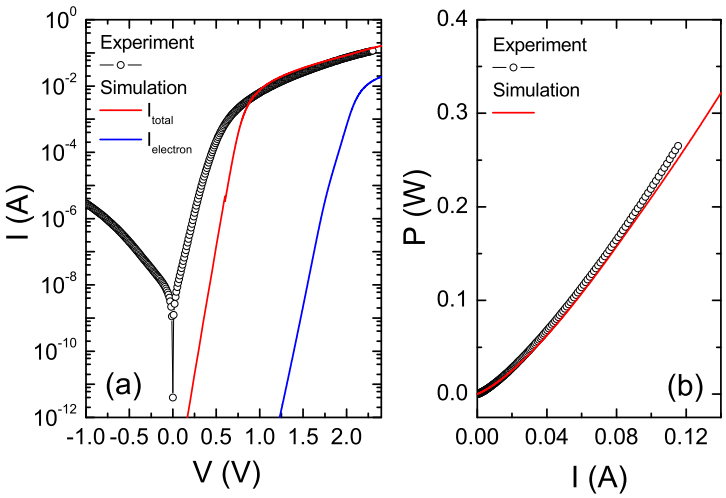

Figure 5.10: (a) Current-voltage characteristic of the spin-LED. Open circles are the experimentally measured data, the solid red (blue) line corresponds to the total (electron-only) current as extracted from the MEDICI simulations. (b) The electrical power dissipated in the spin-LED as a function of current. Open circles are obtained from the experimental $I-V-$curve, the solid red line is obtained from the simulated $I-V-$curve.

5.5.2 Spatially resolved data

In Fig. 5.9 we present the time-traces as a function of position on a line-scan over the spin-LED, with $I = 0$ mA (a), and $I = 133$ mA (b). We observe that the sign of the TiMMS-signal inside the optical window is opposite to the signal outside the optical window. This is the result of the presence of a SiOx-layer outside the optical window, which leads to an additional phase shift of the TiMMS-signal. The time-traces of Figs. 5.9a and 5.9b are fitted with a single exponential decay, starting at $\Delta t = 10$ ps, and the extracted time-constants are presented in Fig. 5.9c. We observe that T_s is larger inside the optical window than outside the optical window, which is likely due to a higher laser fluence outside the optical window, as a result of the absence of metallic layers (see Fig. 5.2b). From Fig. 5.9c the current-induced decrease of T_s can be extracted, via $\Delta T_s = \frac{T_{s,0}-T_{s,133}}{T_{s,0}}$, thereby obtaining the data of Fig. 5.7.

5.5.3 Current-voltage characteristic of the spin-LED

The experimentally measured, and with MEDICI simulated, current-voltage characteristic of the spin-LED is shown in Fig. 5.10a. The experimental data shows a

non-linear $I-V-$curve, characteristic for these spin-LEDs [15]. The $I-V-$curve obtained from the MEDICI simulation shows an almost quantitative agreement with the experimental curve for an applied bias larger than 1 V, which is the regime above luminescence threshold. This indicates that the MEDICI simulation is representative for the actual device. Below 1 V, the simulated current is lower than experimentally observed. The probable origin for this discrepancy is the fact that MEDICI does not take into account the filling of surface states at the AlGaAs interface by electrons tunneling from the electrode.

Figure 5.5.3b shows the dissipated power, P, in the spin-LED as a function of current extracted from both the experimental as well as the simulated $I-V-$curve. Again an good quantitative agreement between the experimental and simulated curve is observed. We note that for $I > 0.05$ mA, the dependence of P on I can be well described by a linear relationship.

Bibliography

[1] I. Žutić, J. Fabian, S. Das Sarma, *Spintronics: Fundamentals and applications*, Rev. Mod. Phys. **76**, 323-410 (2004). 5.1

[2] G. L. Bir, A. G. Aronov, and G. E. Pikus, *Spin relaxation of electrons due to scattering by holes*, Zh. Eksp. Teor. Fiz. **69**, 1382-1397 (1975) [Sov. Phys. JETP **42**, 705-712 (1976)]. 5.1

[3] A. G. Aronov, G. E. Pikus, and A. N. Titkov, *Spin relaxation of conduction electrons in p-type III-V compounds*, Zh. Eksp. Teor. Fiz. **84**, 1170-1184 (1983) [Sov. Phys. JETP **57**, 680-687 (1983)]. 5.3.1, 5.5, 5.3.2

[4] K. Zerrouati, F. Fabre, G. Bacquet, J. B. J. Frandon, G. Lampel, and D. Paget, *Spin-lattice relaxation in p-type gallium arsenide single crystals*, Phys. Rev. B **37**, 1334-1341 (1988).

[5] J. M. Kikkawa, and D. D. Awschalom, *Resonant spin amplification in n-type GaAs*, Phys. Rev. Lett. 80, 4313-4316 (1998).

[6] Y. Ohno, Y., R. Terauchi, F. Matsukura, and H. Ohno, *Spin relaxation in GaAs(110) quantum wells*, Phys. Rev. Lett. **83**, 4196-4199 (1999).

[7] A. Malinowski, R. S. Britton, T. Grevatt, R. T. Harley, D. A. Ritschie, and M. Y. Simmons, *Spin relaxation in $GaAs/Al_xGa_{1-x}As$ quantum wells*, Phys. Rev. B **62**, 13034-13039 (2000).

[8] P. H. Song, and K. W. Kim, *Spin relaxation of conduction electrons in bulk III-V semiconductors*, Phys. Rev. B **66**, 035207 (2002). 5.1

[9] B. Koopmans, J. E. M. Haverkort, W. J. M. de Jonge, and G. Karczewski, *Time-resolved magnetization modulation spectroscopy: A new probe of ultrafast spin dynamics*, J. Appl. Phys. **85**, 6763 (1999). 5.2.1

[10] B. Koopmans, and W. J. M. de Jonge, *Ultrafast spin dynamics in magnetic semiconductor quantum wells studied by magnetization modulation spectroscopy*, Appl. Phys. B **68**, 525 (1999). 5.2.1, 5.3.2

[11] R. Fiederling, M. Kleim, G. Reuscher, W. Ossau, G. Schmidt, A. Waag, and L. W. Molenkamp, *Injection and detection of a spin-polarized current in a light-emitting diode*, Nature (London) **402**, 787-790 (1999). 5.2.1

[12] A. T. Hanbicki, B. T. Jonker, G. Itskos, G. Kioseoglou, and A. Petrou, *Efficient electrical spin injection from a magnetic metal/tunnel barrier contact into a semiconductor*, Appl. Phys. Lett. **80**, 1240-1242 (2002).

[13] V. F. Motsnyi, V. I. Safarov, J. De Boeck, J. Das, W. Van Roy, E. Goovaerts, and G. Borghs, *Electrical spin injection in a ferromagnet/tunnel barrier/semiconductor heterostructure*, Appl. Phys. Lett. **81**, 265-267 (2002). 5.2.1, 5.2.2

[14] C. A. C. Bosco, D. Snouck, P. Van Dorpe, W. Van Roy, and B. Koopmans, *Bias-dependent spin relaxation in a spin-LED*, Mater. Sci. Eng. B **126**, 107 (2006). 5.2.2

[15] V. F. Motsnyi, P. Van Dorpe, W. Van Roy, E. Goovaerts, V. I. Safarov, G. Borghs, and J. De Boeck, *Optical investigation of electrical spin injection into semiconductors*, Phys. Rev. B **68**, 245319 (2003). 5.2.2, 5.5.3

[16] M. R. Brozel, and G. E. Stillman, *Properties of Gallium Arsenide* (3rd Edition), (London: INSPEC, 1996). 5.2.2, 5.3.2

[17] S. Adachi, *Properties of Aluminium Gallium Arsenide*, (London: IEE, 1993). 5.2.2, 5.3.2

[18] For details, see http://www.synopsys.com. 5.3.1

[19] J. Zak, E. R. Moog, C. Liu, and S. D. Bader, *Universal approach to magneto-optics*, J. Magn. Magn. Mater. **89**, 107-123 (1990). 5.3.2

[20] W. Van Roy, private communication. 5.3.2

[21] Y. P. Varshni, *Temperature dependence of the energy gap in semiconductors*, Physica **34**, 149-154 (1967). 5.3.2

Chapter 6

Probing carrier and spin dynamics in GaAs-based nanowires

We have studied the carrier and spin dynamics in multi-segmented GaP / GaAs nanowires, and in single GaP-capped GaP / GaAs / GaP nanowires using an all-optical technique. We have identified two different carrier relaxation processes, carrier thermalization and recombination. The recombination time ($\approx$ 10 ps) is short compared to bulk GaAs, and independent of temperature, for both the multi-segmented as well as the GaP-capped nanowires. This indicates a dominant non-radiative recombination channel via surface and defect states. We show that our two-color magneto-optical technique is capable of measuring spin dynamics within a single nanowire. These measurements suggests that for these GaP-capped nanowires the spin lifetime is recombination limited. This approach enables the study of carrier and spin dynamics in single nanowires, and is complementary to (time-resolved) photoluminescence.[1]

[1] A large part of this Chapter is in preparation for publication as J. H. H. Rietjens, C. A. C. Bosco, M. T. Borgström, E. P. A. M. Bakkers, and B. Koopmans, *Probing carrier and spin dynamics in GaAs-based nanowires*

6.1 Introduction

During the last decade the growth and use of semiconductor nanowires (NWs) has seen a tremendous development [1, 2]. Nowadays it is possible to grow NWs exhibiting a wide range of diameters, lengths, and types of semiconductors, with the possibility to combine segments of different materials in a single wire, including varying the doping profile [3–5]. It has been demonstrated that NWs can be used as light-emitting diodes [3], photo-detectors [6], field-effect transistors [7], and bio/chemical sensors [8, 9]. Moreover, NWs provide the possibility to integrate the superior optical and electrical properties of III/V semiconductors with the well-established Si-technology [10, 11]. Yet another promising application of semiconductor NWs could be their use as potential building blocks for spintronic devices, exploiting the spin degree of freedom. The one-dimensional nature and quantum confinement effects of NWs can be used to make e.g. spin-based transistors or spin-based qubits for quantum computation. For this purpose the electron spin decoherence time should be long enough to perform spin operations. It is therefore important to study and control the carrier and spin dynamics in individual NWs.

In this Chapter we report on the characterization of the carrier relaxation time, and electron spin dephasing time in GaAs-based NWs with a microscopic time- and spatially-resolved all-optical approach. We have chosen for the GaP/GaAs system, as GaAs is one of the main high performance III/V systems, and can have high radiative lifetimes and high spin dephasing times in bulk and quantum well systems under certain temperature and doping conditions. We have studied ensembles of multi-segmented GaP/GaAs NWs, and performed single wire experiments on GaP-capped GaP/GaAs/GaP-NWs. We will discuss the observed carrier relaxation processes in connection with the observed spin lifetime, and demonstrate that using this technique it is possible to address carrier and spin dynamics in single nanowires.

6.2 Experimental details

A microscopic all-optical time-resolved pump-probe technique is used in order to directly measure the carrier and spin dynamics in the NW after excitation. A mode-locked Ti:Sapphire laser produces laser pulses ($\approx$ 100 fs temporal width, 80 MHz repetition rate) with photon energies ranging from 1.45 to 1.67 eV. The laser pulses are divided in strong pump and weak probe pulses. Pump and probe beam are focused to an overlapping spot on the sample in an optical cryostat. In the transient reflectivity (TR) configuration, the pump beam is linearly polarized ($p-$polarization) and excites (non spin-polarized) electron-hole pairs in the NW, thereby changing the optical reflection and absorption constants. The time-dependent change in optical constant is measured via the TR of the $s-$polarized probe beam. In this way the setup is sensitive to the carrier dynamics, such as carrier thermalization and carrier recombination, but also detects other pump related changes to the dielectric tensor

such as heating. In the Magneto-Optical (MO) configuration, the pump beam is circularly polarized in order to excite electron spins via the optical selection rules of zinc-blende semiconductors. The excited spins are probed via the magneto-optical Kerr-effect (MOKE) experienced by the linearly polarized probe beam after reflection from the sample. In this configuration the MO-signal depends on the spin lifetime T_s, which is related to the spin relaxation time τ_s, and the carrier recombination time τ_r via $T_s^{-1} = \tau_s^{-1} + \tau_r^{-1}$. Time resolution is obtained by delaying the probe beam with respect to the pump beam with a mechanical translation stage. In order to study the ensemble wires, we used an objective resulting in a spot size of ≈ 20 μm for pump and probe. For single wire measurements we used a different objective, resulting in a spot size of ≈ 3 μm of the probe (and ≈ 7 μm pump spot size). Time-resolved measurements were performed at a temperature of 5 K and room temperature (RT).

6.3 Probing ensembles of multi-segmented GaP / GaAs nanowires

Let us first consider our measurements on an ensemble of multi-segmented GaP / GaAs NWs. Samples for the NW growth were prepared by dispersing 20 nm diameter Au colloids on a thermally oxidized (500 nm) Si substrate. The NWs were grown via the Vapor-Liquid-Solid growth technique by using Metallo-Organic-Vapor-Phase-Epitaxy (MOVPE) with trimethylgallium (TMG), phosphine (PH_3), and arsine (AsH_3) as precursors in a H_2 environment. The first segment of the wire is a GaP-segment, which is followed by alternating GaAs and GaP segments by switching the group V precursors in the growth chamber. Details of the growth technique have been described in reports on the growth kinetics [12], and interface chemical composition [5] of such wires. The diameter of the NWs is ≈ 20 nm, and the length of the smallest segment is ≈ 25 nm, so no quantum confinement effects are expected. A high-angle annular dark-field transmission microscope (HAADF-TEM) image of the resulting NW is shown in the inset of Fig. 6.1. The individual GaP and GaAs segments and the Au catalyst particle are clearly visible. The NW are oriented in random directions and we estimate the density to be $\approx 10^8$ cm^{-2}. A microscope picture of a part of the NW sample is also shown in the inset of Fig. 6.1.

6.3.1 Transient reflectivity measurements

We performed time resolved transient reflectivity (TR) measurements on these wires in order to study the carrier dynamics. With a ≈ 20 μm spot size, we estimate that we average over an ensemble of 10^2 to 10^3 wires. A typical TR measurement taken at a temperature of 5 K with a laser photon energy of 1.59 eV is shown in Fig. 6.1. After a fast decrease of the transient reflectivity at $\Delta t = 0$, the signal recovers to

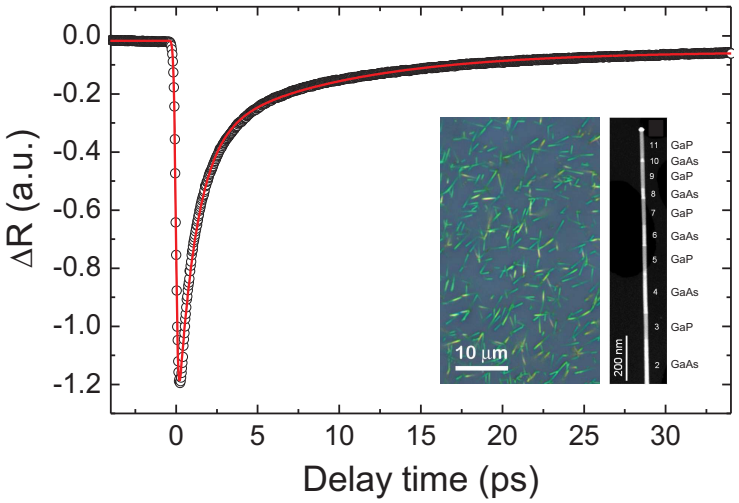

Figure 6.1: Time-resolved transient reflectivity measurement on the ensemble wires, taken at a temperature of 5 K, and a laser photon energy of 1.59 eV. The solid line represents a fit to the data using equation 6.1, yielding the time constants $\tau_1 = 1.1$ ps and $\tau_2 = 8.7$ ps. Insets are an optical microscope picture of the sample and a high-angle annular dark-field transmission microscope (HAADF-TEM) image, clearly showing the different segments.

a value slightly above the equilibrium value at $\Delta t < 0$. This apparent offset is due to a contribution from the substrate, as will be shown later on. As the bandgap of GaP is 2.26 eV at 5 K, no carriers are excited in the GaP. The time dependence of the TR-signal can be described according to

$$\Delta R = \int e^{-(t/d)^2} \Theta(t) dt \cdot \left[A_1 e^{-t/\tau_1} + A_2 e^{-t/\tau_2} + A_3 \right] \tag{6.1}$$

The integral is the convolution of the Gaussian laser pulse (full-width at half maximum $= d2\sqrt{\ln 2}$) with the unit step function, and represents the transient decrease in reflectivity due to excitation of carriers by the Gaussian laser pulse (in the GaAs of the NWs, and partly in the substrate). The part between the brackets describes two carrier relaxation processes with their time constants τ_1 and τ_2 and amplitudes A_1 and A_2. As the decay of the substrate contribution is much larger than the time window of the measurement, it is described by the constant A_3. Fitting the data of Fig. 6.1 with Eq. 6.1 yields for the two time constant $\tau_1 = 1.1$ ps and $\tau_2 = 8.7$ ps.

The physical processes related to these time scales can be identified by performing spectroscopy in the TR-configuration. In Fig. 6.2 we plot τ_1 and τ_2 and the corresponding amplitudes A_1 and A_2 vs. photon energy. We see that between 1.50 and 1.59 eV $\tau_1 \approx 1.2$ ps, and that τ_1 decreases to ≈ 0.5 ps at higher energy.

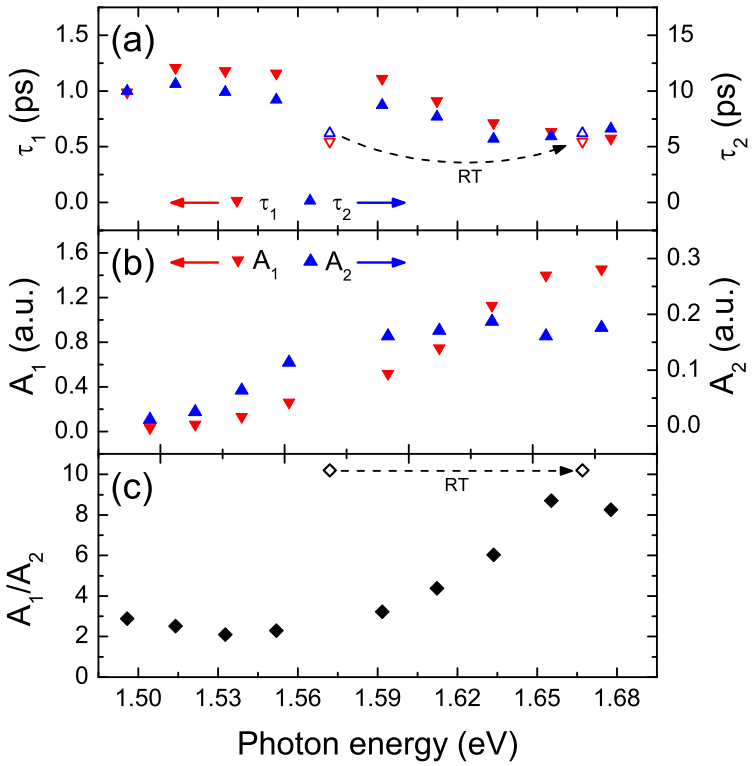

Figure 6.2: Results of transient reflectivity measurements as a function of laser photon energy on an ensemble of multi-segmented GaP/GaAs nanowires. (a) Time-scales τ_1 and τ_2 obtained from a fit of the measurement data to Eq. 6.1. (b) The amplitudes A_1 and A_2 corresponding to the time-scales τ_1 and τ_2 of (a) respectively. (c) Ratio of the amplitudes A_1 and A_2. The open symbols represent a transient reflectivity measurement taken at room temperature with a laser photon energy 1.57 eV (0.15 eV above the room temperature bandgap), and are also positioned at 1.67 eV (0.15 eV above the 5 K bandgap).

This decrease is likely to be associated with LO-phonon emission. τ_2 is roughly constant between 1.5 eV and 1.6 eV and also decreases at higher photon energy. The amplitudes A_1 and A_2 both decrease when the laser photon energy approaches the bandgap of GaAs around 1.52 eV. This is a signature that less carriers are excited (and thus the TR-signal is reduced) due to the lower absorption close to the bandgap. However, the ratio of A_1 and A_2 decreases with decreasing photon energy. This decreasing ratio indicates that the physical process related to τ_1 becomes relatively less important when the photon energy approaches the bandgap of GaAs. This observation suggests that τ_1 is the timescale of thermalization of excited electrons to the bottom of the conduction band, which is expected to be less important when the excess energy of electrons in the conduction band is reduced. The process related to τ_2 is ascribed to a carrier recombination process, thereby reducing ΔR from the NWs back to zero, when no excited carriers are present anymore.

The observed recombination time of ≈ 10 ps is low compared to values of bulk GaAs [13], and surface passivated GaAs-based nanowires [14]. One reason can be recombination from defect states at the GaAs/GaP or GaAs/air interface, as a result of the relatively large surface-to-volume ratio due to the small size of the NWs. A dominating surface recombination has been observed in other nanowire systems [15]. An estimation of the time-scale associated with such a process can be obtained by calculating the average time it takes for an excited electron to reach the interface. From the cylindrical geometry of the nanowire it follows that, assuming a random momentum distribution of the excited electrons, the average distance of an excited electron to the interface is given by

$$d \approx (1 + \log 2l_{ave}/r_{ave})\, r_{ave}. \tag{6.2}$$

Here, $r_{ave} = 8r/3\pi$ is the average distance in the radial direction, and $l_{ave} = l/2$ is the average distance in the parallel direction. This expression is accurate within 0.5% for $l/d > 5$. If we take $r = 10$ nm and $l = 100$ nm for the present NWs, we have $d = 23$ nm. Using the Einstein relation for the diffusion coefficient, $D = \mu k_B T$, we can estimate the recombination time via $d = \sqrt{D\tau_r}$. Taking a moderate value for the electron mobility in GaAs, $\mu = 1000$ cm^2/Vs, we estimate $\tau_r = 12$ ps, which is in reasonable agreement with our experimental data. Another indication that non-radiative decay via defects is dominating is given by a room-temperature TR-measurement with a laser photon energy of 1.57 eV. We note that this energy is 0.15 eV above the GaAs band-gap at room temperature (1.42 eV). This measurement yields $\tau_1 = 0.55$ ps, $\tau_2 = 6.2$ ps, $A_1/A_2 = 10.2$. If we compare these values with those of Fig. 6.2 at a photon energy of 1.67 eV (which is also 0.15 eV above the GaAs band-gap at 5 K), we see that the room temperature measurement nicely follows the trend at 5 K. From this we conclude that non-thermally activated processes dominate the carrier recombination.

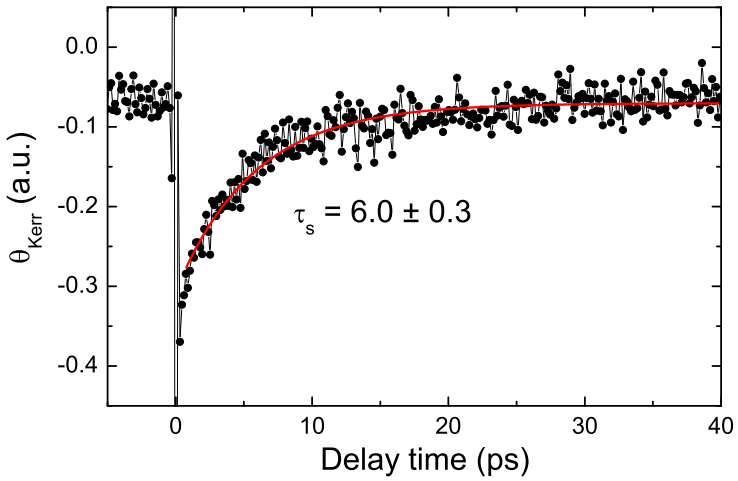

Figure 6.3: Time-resolved magneto-optical measurement on the ensemble wires, taken at a temperature of 5 K, and a laser photon energy of 1.57 eV. The solid line represents a single exponential fit to the data, yielding a time constant of 6.0 ps.

6.3.2 Magneto-optical measurements

The short recombination time determined above implies that the timescale of the spin signal we might detect in a MO experiment is at most of the order of 10 ps, even when the spin relaxation time is much higher. The carrier lifetime determines in this case the spin lifetime, and thus the decrease of the MO-signal, via $T_s^{-1} = \tau_s^{-1} + \tau_r^{-1}$. We performed MO measurements on the ensemble of nanowires, of which a representative result, taken at a laser photon energy of 1.57 eV, is shown in Fig. 6.3. The signal-to-noise ratio for this measurement is a factor $\approx 10^3$ lower than for the TR-measurement. We attribute this to the effect of a strong polarization anisotropy [6] exhibited by these NWs. Due to the polarization anisotropy, the NW effectively acts as a polarizer, limiting the penetration of circularly polarized light. This leads to a strongly reduced efficiency of excitation of spins via the optical selection rules, and also to a strongly reduced detection sensitivity of electron spins via the MOKE, which decreases the efficiency of optical spin injection and detection. The sharp increase of the MO-signal at $\Delta t = 0$ is a signature of optical spin orientation due to the pump pulse, and is followed by a fast decay to its equilibrium value. In order to extract the time-scale of this decay, we can again use Eq. 6.1 to fit the data. Setting A_2 to zero (single exponential decay) yields for the spin lifetime $\tau_1 = T_s = 6.0$ ps. Although an effect of carrier thermalization on the MO-signal is not observed, we note that the extracted T_s is close to the recombination time τ_2, which might indicate a recombination limited spin lifetime.

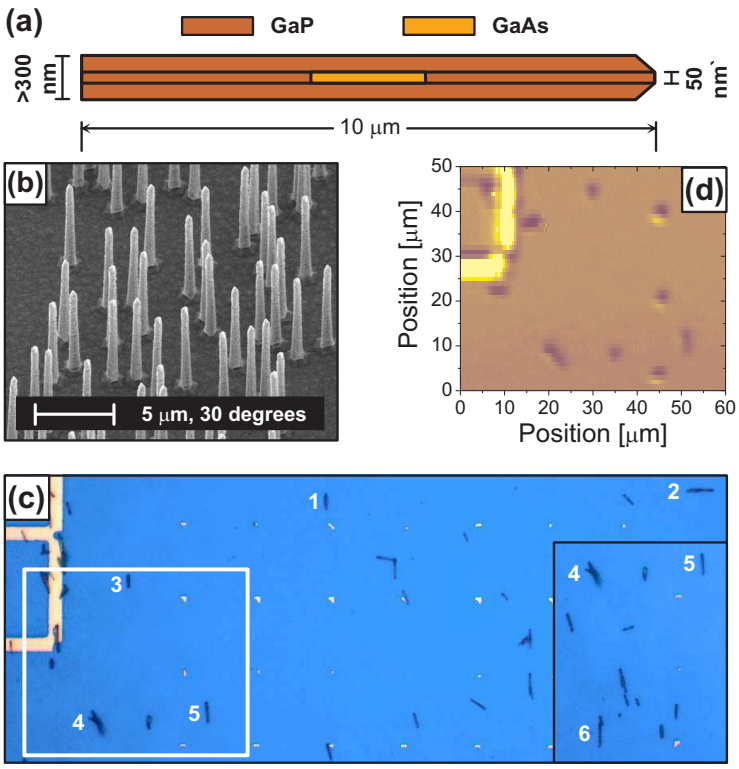

Figure 6.4: (a) Schematic picture of the capped GaP-GaAs-GaP NWs. (b) Scanning electron microscope image of the vertically grown NWs. (c) Optical microscope image of a marker sample onto which several NWs are transferred, with several NWs labeled. (d) Raster scan of the area indicated by the white box in (c), showing the spatial resolution of the setup.

6.4 Probing single capped GaP / GaAs / GaP nanowires

We now turn to the single wire experiments on especially engineered NWs. In order to reduce the polarization anisotropy we have grown NWs consisting of a single GaAs segment sandwiched between two GaP segments on a GaP(111) substrate. After the perpendicular growth via the VLS growth technique using Au catalyst particles and MOVPE at 500 °C, the NWs are capped with GaP via side-wall deposition at elevated temperatures. The resulting wires are schematically illustrated in Fig. 6.4a and shown in Fig. 6.4b in a scanning electron microscope image. The NWs have a central core with a diameter of $\approx$ 50 nm, and a thick GaP cap of 150 nm. The

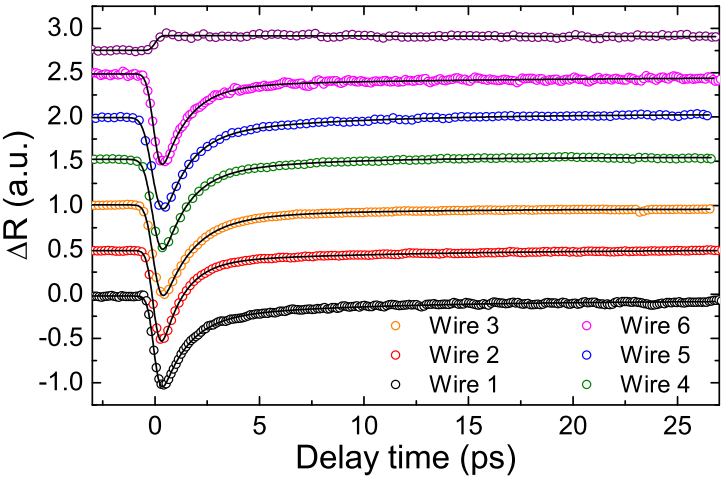

Figure 6.5: Transient reflectivity (TR) measurement on six different NWs, labeled according to Fig. 6.4c. The top TR-measurement is taken on the bare Si/SiOx substrate.

thick capping layer should decrease the polarization anisotropy and enhance our spin sensitivity. After growth the perpendicular NWs are transferred to a marker-sample with predefined Au dots for easy recognition of individual NWs in microscopy studies. An optical microscope image of an area with low NW density, is shown in Fig. 6.4c. Some of the NWs are labeled for further reference. Fig. 6.4d shows a raster scan of the area indicated by the white box in Fig. 6.4c. It demonstrates the spatial resolution of the setup, which enables single wire measurements.

6.4.1 Transient reflectivity measurements

First, we focus on TR measurements taken on wires $1-6$ as shown in Fig. 6.5. These measurements are taken at a temperature of 5 K and a laser photon energy of 1.61 eV. At $\Delta t = 0$ a sharp decrease of the TR is observed, followed by a recovery on a 20 ps timescale. The signal can be well fitted according to Eq. 6.1, of which the main fit parameters are shown in Table 6.1. A remarkable similarity of the two timescales is observed with those obtained from measurements on the ensemble wires. Hence, we can also in this case identify τ_1 as the time-scale of electron thermalization, and τ_2 as the carrier recombination time. It appears that also for these wires non-radiative recombination processes are dominant, and most likely mediated via defect states at the GaP/GaAs interface. The capping of the GaAs-core with the GaP-shell does not seem to lead to surface passivation, which has been observed in other systems [16, 17]. From Table 6.1 it further follows that this fast carrier relaxation

Table 6.1: Parameters of a fit of Eq. 6.1 to the transient reflectivity signal of the six labeled NWs in Figure 6.5.

Wire	τ_1 (ps)	τ_2 (ps)	A_1	A_2
1	1.3	9.2	-5.7	-1.0
2	1.1	10.9	-6.9	-0.8
3	1.4	7.2	-6.4	-0.7
4	1.2	5.5	-6.7	-1.2
5	1.2	7.5	-6.8	-1.3
6	1.2	12.9	-6.5	-0.6

is characteristic for all wires from which a decent TR-signal could be obtained. The top TR-measurement in Fig. 6.5 is taken on the bare Si/SiOx substrate, and shows a step-like signal, which we attribute to excited carriers in the Si, which have a relatively long recombination time due to the indirect bandgap of Si. We note that this contribution, to some extend, is present in all single wire measurements, and is also observed in the ensemble measurement of Figs. 6.1 and 6.2.

In Fig. 6.6 we present measurements performed on different positions on a line scan over NW 5. It shows the reflection of the probe beam, the TR-signal at a fixed time delay of 1 ps, and an image containing time-traces, all as a function of position. The three segments of the wire can be clearly identified in the reflection scan (Fig. 6.6a), where the reflectivity of the center GaAs segment is slightly higher than the reflectivity of the two GaP segments. In the TR-scan (Fig. 6.6b) only the GaAs segment can be recognized, indicating that only in this segment free carriers are excited. This is expected because the laser photon energy (1.6 eV) is below the indirect bandgap of GaP (2.26 eV), but above that of GaAs (1.52 eV). The time-resolved signals in color scale show that for positions < -6 μm and > 6 μm, the measurement data is similar to the top measurement of Fig. 6.2, and originates from the Si substrate. Also, as expected from the TR-scan, only on the positions that match the GaAs segment a clear TR-signal is observed. This proves that we are indeed probing (parts of) a single nanowire.

6.4.2 Magneto-optical measurements

Let us now turn to the magneto-optical (MO) measurements taken on NWs 1 and 6, which are shown in Fig 6.7. Here we see, surprisingly, an exponentially decaying signal both in the positive as well as in the negative delay time direction. This can be understood if we consider the fact that a single nanowire is an effective scatterer, since the width is much smaller than our laser spot. Therefore, a significant portion of the pump laser pulse is scattered in all directions, including towards the detector. This scattered pump light contains information of excited carriers when the pump beam arrives later at the sample than the probe beam, in a similar way as in the

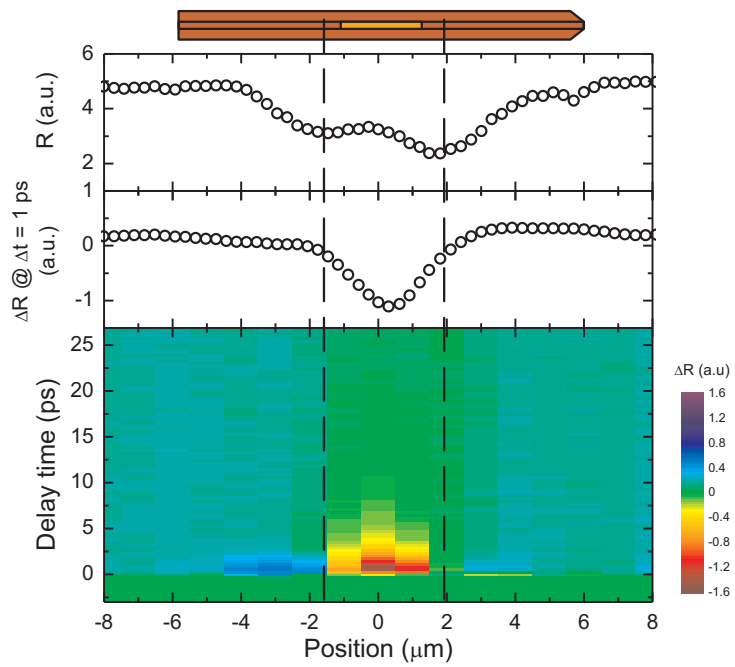

Figure 6.6: (a) Line scan of NW 5 showing the reflection (R) of the probe beam vs. position. (b) Line scan over NW 5 showing the transient change in reflectivity (ΔR) at a fixed time delay of 1 ps. (c) Image showing TR time-traces taken on different positions along NW 5.

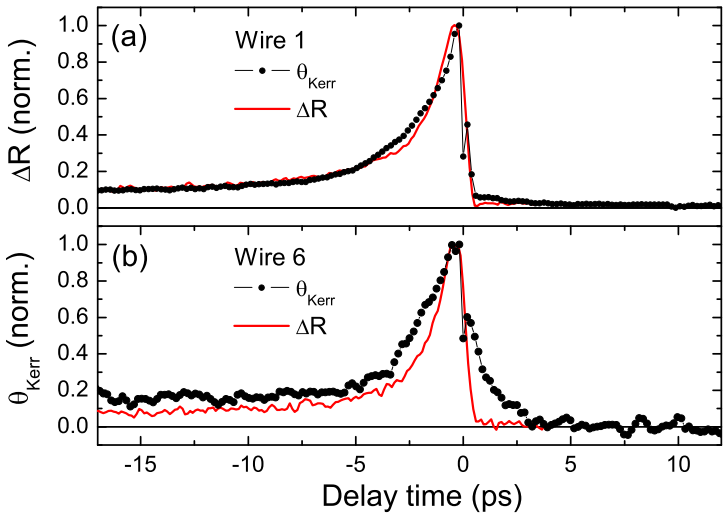

Figure 6.7: Time-resolved magneto-optical measurement performed on wire 1 (a) and wire 6 (b). Also shown are transient reflectivity measurements of the same wires (red lines), which are mirrored in the vertical axis (positive and negative delay time is reversed).

transient reflectivity measurements discussed above. At negative time delay the function of pump and probe beam are thus reversed, and the measurement scheme is that of a standard ellipsometry measurement [18]. We are thus performing time-resolved ellipsometry, and the measurement is sensitive to changes in the complex refractive index, e.g. due to excited carriers in the wire. This interpretation is supported by the fact that the time-resolved MO-signal at negative delay time is similar to the TR-signal at positive delay time, as shown in Fig. 6.7 where TR-measurements on NWs 1 and 6 are shown in a red line with the time-axis reversed. At positive time delays, the technique is only sensitive to pure magneto-optics, proving we are measuring spin dynamics in a single NW. The exponential decay in the MO-signal shows a time-constant of 2.4 ps and 1.3 ps for NW 1 and 6, respectively. A second exponential in the time-resolved signal could not be observed in this case, due to the low signal-to-noise ratio. We note that the MO-signal-to-TR-signal-ratio varies from NW to NW and that it depends strongly on the position on the NW that is probed. For some NW the signal-to-noise ratio was too low to measure the MO-signal.

Two-color experiments

In order to reduce the pump scattering, and enhance the signal-to-noise ratio, we performed a two-color pump-probe experiment using two phase-locked Ti:Sapphire

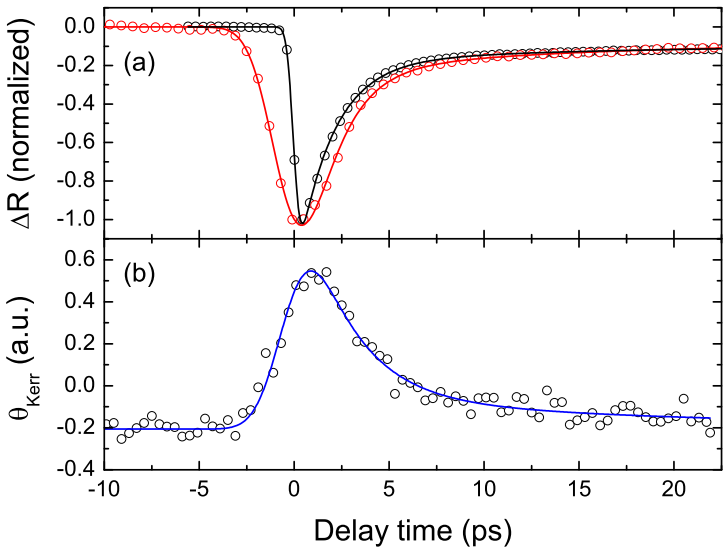

Figure 6.8: (a) Time-resolved transient reflectivity with pump and probe photon energy of 1.61 eV, using one laser (black) and two lasers (red), performed on wire 6 at room temperature. (b) Magneto-optical measurement at the same wire, with a pump photon energy of 1.58 eV and a probe photon energy of 1.50 eV. Solid lines are fits to the data using Eq. 6.1.

lasers. By placing a notch-filter, centered around 1.582 eV with blocking window 1.542-1.623 eV, in front of the detector, scattered pump light (photon energy of 1.58 eV) could be blocked while transmitting the probe beam (photon energy of 1.50 eV). In order to check the effect of phase-locking the two Ti:Sapphire lasers, we performed two TR-measurement on wire 6, taken at room temperature with the same pump and probe photon energy of 1.61 eV, using either one laser, or two phase-locked lasers, as shown in Fig. 6.8a. Due to jitter in the locking electronics, causing a fluctuating difference between pump and probe delay, the two-laser time-trace is broadened. We could still use Eq. 6.1 to fit the two-laser data, by increasing the value for the width of the Gaussian, d, to $d = 2.72$ ps, thereby effectively treating the effect of the jitter as a broadened Gaussian pump pulse. The timescales obtained from this fit are $\tau_1 = 1.8 \pm 0.1$ ps, and $\tau_2 = 14 \pm 1$ ps, which are slightly higher than the timescales at 5 K in Table 6.1.

A two-color MO-measurement (pump photon energy 1.58 eV, probe photon energy 1.50 eV), taken on wire 6, is shown in Fig. 6.8b. Here, we see again the effect of electronic jitter, resulting in a broadened peak around $\Delta t = 0$ ps. Also a clear decay of the MO-signal at positive delay times is evident, while at negative delay times no signal is present. This confirms our interpretation of the one-color MO-

measurement, that the signal at negative delay times is due to pump scattering. We can fit the full time-resolved MO-signal with Eq. 6.1, by fixing the value of d and setting A_3 to zero, as no magneto-optical contribution from the substrate is expected. This way, we find for the two time constants $\tau_1 = 2.6 \pm 0.5$ ps, and $\tau_2 = 20 \pm 16$ ps. As there is a reasonable agreement with the timescales of the TR-measurement, the MO-measurement points towards a recombination limited spin lifetime.

6.5 Conclusion

Summarizing, we have performed time-resolved all-optical experiments on segmented GaP / GaAs nanowires, thereby addressing both carrier as well as spin dynamics in ensemble and single nanowires. The carrier recombination is observed to range between 5 and 15 ps for all addressed single nanowires, which is in the range as those obtained from the ensemble wires. This, and the fact that the carrier recombination time is independent of temperature, indicates a strong contribution of non-radiative recombination via defect states at the GaAs/air and GaAs/GaP interface. By performing two-color experiments on single nanowires, we have demonstrated that our technique is capable of measuring spin dynamics within a single nanowire. These measurements suggests that for these nanowires the spin lifetime is recombination limited. This approach enables studying carrier and spin dynamics in single nanowires and is complementary to (time-resolved) photoluminescence.

Bibliography

[1] C. M. Lieber, *Nanoscale Science and Technology: Building a Big Future from Small Things*, MRS Bull. **28**, 486 (2003). 6.1

[2] M. Law, J. Goldberger, and P. Yang, *Semiconductor nanowires and nanotubes*, Annu. Rev. Mater. Res. **34**, 83 (2004). 6.1

[3] X. Duan, Y. Huang, Y. Cui, J. Wang. and C. M. Lieber, *Indium phosphide nanowires asbuilding blocks for nanoscaleelectronic and optoelectronic devices*, Nature (London) **409**, 66-69 (2001). 6.1

[4] M. S. Gudiksen, L. J. Lauhon, J. Wang, D. C. Smith, and C. M. Lieber, *Growth of nanowire superlattice structures for nanoscale photonics and electronics*, Nature (London) **415**, 617 (2002).

[5] M. T. Borgström, M. A. Verheijen, G. Immink, T. de Smet, and E. P. A. M. Bakkers, *Interface study on heterostructured GaP-GaAs nanowires*, Nanotechnology **17**, 4010-4013 (2006). 6.1, 6.3

[6] J. Wang, M. S. Gudiksen, X. Duan, Y. Cui, and C. M. Lieber, *Highly Polarized Photoluminescence and Photodetection from Single Indium Phosphide Nanowires*, Science **293** 1455 (2001). 6.1, 6.3.2

[7] J. Xiang, W. Lu, Y. Hu, Y. Wu, H. Yan, and C. M. Lieber, *Ge/Si nanowire heterostructures as high-performance field-effect transistors*, Nature (London) **441**, 04796 (2006). 6.1

[8] E. Stern, J. F. Klemic, D. A. Routenberg, P. N. Wyrembak, D. B. Turner-Evans, A. D. Hamilton, D. A. LaVan, T. M. Fahmyl, and M. A. Reed, *Label-free immunodetection with CMOS-compatiblesemiconducting nanowires*, Nature (London) **445**, 7127 (2007). 6.1

[9] M. C. McAlpine, H. Ahmad, D. Wang, and J. R. Heath, *Highly ordered nanowire arrays on plasticsubstrates for ultrasensitive flexiblechemical sensors*, Nat. Mater. **6**, 379-384 (2007). 6.1

[10] T. Martensson, C. Patrik, T. Svensson, B. A. Wacaser, M. W. Larsson, W. Seifert, K. Deppert, A. Gustafsson, L. R. Wallenberg, and L. Samuelson, *Epitaxial III-V nanowires on silicon*, Nano Lett. **4**, 1987-1990 (2004). 6.1

[11] E. P. A. M. Bakkers, J. A. van Dam, S. De Franceschi, L. P. Kouwenhoven, M. Kaiser, M. Verheijen, H. Wondergem, and P. van der Sluis, *Epitaxial growth of InP nanowires on germanium*, Nat. Mater. **3**, 769-773 (2004). 6.1

[12] M. A. Verheijen, G. Immink, G., T. de Smet, M. T. Borgström, and E. P. A. M. Bakkers, *Growth Kinetics of Heterostructured GaP-GaAs Nanowires*, J. Am. Chem. Soc. **128**, 1353-1359 (2006). 6.3

[13] R. J. Nelson, and R. G. Sobers, *Minority-carrier lifetime and internal quantum efficiency of surface-free GaAs*, J. Appl. Phys. **49**, 6103 (1978). 6.3.1

[14] N. Sköld, L. S. Karlsson, M. W. Larsson, M.-E. Pistol, W. Seifert, J. Trägårdh, and L. Samuelson, *Growth and Optical Properties of Strained GaAs-$Ga_xIn_{1-x}P$ Core-Shell Nanowires*, Nano Lett. **5**, 1943-1947 (2005). 6.3.1

[15] L. V. Titova, T. B. Hoang, H. E. Jackson, L. M. Smith, J. M. Yarrison-Rice, J. L. Lensch, and L. J. Lauhon, *Low-temperature photoluminescence imaging and time-resolvedspectroscopy of single CdS nanowires*, Appl. Phys. Lett. **89**, 053119 (2006). 6.3.1

[16] M. Matilla, T. Hakkarainen, H. Lipsanen, H. Jiang, and E. I. Kauppinen, *Enhanced luminescence from catalyst-free grown InP nanowires*, Appl. Phys. Lett. **90**, 033101 (2007). 6.4.1

[17] L. V. Titova, T. B. Hoang, J. M. Yarrison-Rice, H. E. Jackson, Y. Kim, H. J. Joyce, Q. Gao, H. H. Tan, C. Jagadish, X. Zhang, J. Zou, and L. M. Smith, *Dynamics of Strongly Degenerate ElectronHole Plasmas and Excitons inSingle InP Nanowires*, Nano Lett. **7**, 3383-3387 (2007). 6.4.1

[18] S. N. Jasperson, and S. E. Schnatterly, *An improved method for high reflectivity ellipsometry based on a new polarization modulation technique*, Rev. Sci. Instr. **40**, 761-767 (1969). 6.4.2

Chapter 7

Optical control over electron g factor and spin decoherence in (In,Ga)As/GaAs quantum dots

We have studied the dependence of the electron in-plane g factor and spin decoherence time on the built-in electric field (E_i) at the position of a single layer of self-assembled (In,Ga)As/GaAs quantum dots (QDs). Control of E_i is achieved by inducing screening charges in a $p-i-n$ GaAs matrix with a continuous wave (cw) laser. Using a time-resolved pump-probe technique to measure the spin dynamics via the magneto-optical Kerr effect, we observe a large hole spin decoherence time of 440 ps. Measurements as a function of the cw laser power and, thus, of E_i show that the electron spin decay time in the QDs depends strongly on E_i and decreases from 310 to 110 ps with increasing E_i. We attribute this effect to increasing tunneling rates of electrons out of the QDs at high E_i. We observe a slight increase of the electron g factor from 0.40±0.03 to 0.46±0.04 with increasing E_i, which might be a result of a changing wavefunction as a result of a different confinement potential due to E_i.[1]

[1]This Chapter is published as J. H. H. Rietjens, G. W. W. Quax, C. A. C. Bosco, R. Nötzel, A. Yu. Silov, and B. Koopmans, *Optical control over electron g factor and spin decoherence in (In,Ga)As/GaAs quantum dots*, J. Appl. Phys. **103**, 07B116 (2008)

7.1 Introduction

Semiconductor quantum dots (QDs) are good candidates for buildings blocks of future spintronic devices, such as single photon emitters for quantum information applications [1], and qubits for quantum computation [2]. In the latter application, the electron spin in a quantum dot forms a two-level quantum system that is the basis of the qubit. Two key ingredients for full functionality of the qubit are a long spin decoherence time and the ability to manipulate each spin. Spin decoherence times should be longer than the time needed for performing spin operations. One way to enable local spin manipulation that might lead to scalable qubits is g factor engineering in a solid state environment. Methods reported for g factor engineering include the use of parabolic quantum wells and a gate voltage [3, 4] strain engineering of the quantum dot growth [5], and electrical tunability of the molecular spin state g factor in quantum dot molecules [6]. Besides this application driven research, some fundamental issues still exist, such as the precise dependence of the electron and hole g factor and spin decoherence time on the size, shape, and composition of the QDs [7, 8]. In this paper, we study the dependence of the electron g factor and spin decoherence time on the built-in electric field (E_i) at the position of a single layer of self-assembled (In,Ga)As/GaAs QDs by a time-resolved magneto-optical technique. Control over E_i is achieved by screening E_i with photoexcited carriers by continuous wave (cw) laser excitation. The tunability of the electron g factor and spin decoherence time will be discussed.

7.2 Experimental details

7.2.1 Quantum dot growth and properties

The self-assembled (In,Ga)As/GaAs QDs are grown by molecular beam epitaxy at a temperature of 525°C. The single layer of QDs is situated at the center of the intrinsic region of a GaAs $p-i-n$ heterostructure which is grown on a p-doped GaAs substrate, as shown in Fig. 7.1(a). The heavily p^{++} and n^{--} regions have a doping concentration of 5×10^{18} cm^{-3}, which results in a built-in electric field over the 60 nm intrinsic region of ≈ 240 kV/cm. The (In,Ga)As QDs are grown on GaAs via the Stranski-Krastanov growth method. Atomic force microscope images taken at the same sample right after the quantum dot growth indicated that the QDs have a height of 6.7 ± 1.5 nm and an average diameter of 24.8 ± 5.0 nm. The dot density was determined to be 4.5×10^{10} cm^{-2}. Photoluminescence (PL) spectra were taken with a cw laser operating at 1.55 eV as a function of excitation power (P_{exc}). A PL spectrum taken with $P_{exc} = 0.4$ kW/cm^2 is shown in Fig. 7.1(b). It has a peak at 1.269 eV and a full width at half maximum of 80 meV owing to the size distribution and, therefore, the ground state energy levels of the QDs. The PL spectra exhibit a Stark shift as a function of P_{exc}, with saturation when $P_{exc} > 0.2$ kW/cm^2. The saturation indicates the full quenching of E_i and by mapping E_i via

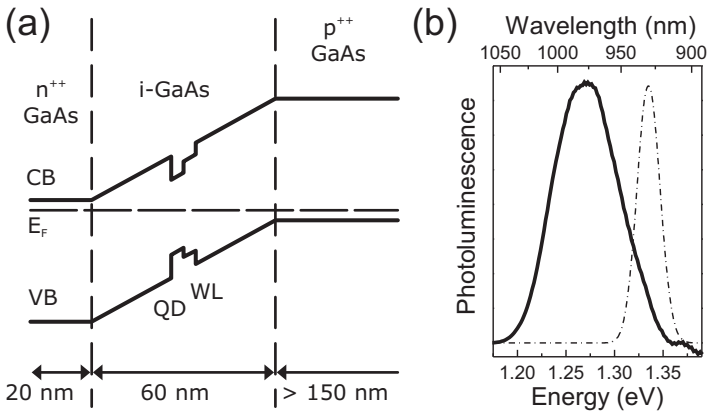

Figure 7.1: (a) Schematic energy diagram of the $p{-}i{-}n$ heterostructure with the quantum dots (QDs) and wetting layer (WL) at the center of the intrinsic region. The position of the conduction band (CB), valence band (VB), and Fermi level (EF) is indicated. (b) Photoluminescence spectrum of the QDs with $P_{exc} = 0.4$ kW/cm^2. Also, the (low) emission from the wetting layer at 1.37 eV can be seen. The dashed line represents the spectral profile of the laser pulses used in the time-resolved experiments.

the Stark shift to P_{exc}, we are able to tune E_i from 0 to 240 kV/m. These PL results will be published elsewhere [9].

7.2.2 Measurement technique: TiMMS

We have studied electron and hole spin dephasing by optical means, using time-resolved magnetization modulation spectroscopy (TiMMS). The quantum dot sample is placed in a magneto-optical cryostat at a temperature of 5 K and in a magnetic field (up to 0.35 T) in the Voigt geometry (parallel to the sample plane). A mode-locked Ti:sapphire laser, operating at 80 MHz, produces ≈100 fs laser pulses with a wavelength of 930 nm (1.335 eV, which is below the GaAs bandgap). The spectral width of the laser pulses is typically 10 nm (14.4 meV) so we probe a relative large portion of the QDs that emit in the high energy tail of the PL spectrum [see Fig. 7.1(b)]. Consequently, the obtained decoherence times and g factors are averages over the probed ensemble of QDs. In order to perform stroboscopic time-resolved measurements, the laser beam is divided in a strong pump beam (≈ 5 mW) and a weaker probe beam (≈ 1.5 mW). The use of these relatively strong laser powers is justified by the low absorption of the thin wetting layer and QDs. The time delay between pump and probe beams is controlled by a motorized translation stage. The pump beam passes through a photoelastic modulator, producing left- and right-

circularly polarized light at a frequency of 50 kHz for optical spin injection. Both pump and probe beams are focused to an overlapping spot of $\approx$ 12 μm on the quantum dot sample and the reflected probe light is collected with a Si photodiode, after passing a quarter wave plate ($\alpha_{qwp} = 45°$) and analyzer ($\alpha_{ana} = 0°$). It can be shown [10] that the measured signal is proportional to the magneto-optical Kerr rotation, which originates from differences in the joint density of states of spin up and spin down carriers. It is thus proportional to the electron and hole spin in the system. We note that a TiMMS measurement yields the electron and hole spin decay time ($T_{s,e}$ and $T_{s,h}$, respectively). The electron-hole recombination time (τ_r) should be used to extract the true electron and hole spin decoherence times $\tau_{s,e}$ and $\tau_{s,h}$, respectively, via $1/T_{s,e} = 1/\tau_r + 1/\tau_{s,e}$.

Additionally, we use a cw HeNe laser with $\lambda = 632.8$ nm (1.92 eV, above the GaAs bandgap) and a laser power of $0 - 3.2$ mW ($P_{HeNe} = 0 - 0.4$ kW/cm^2). The laser beam is also focused to an overlapping spot of $\approx$ 16 μm diameter in order to create charge carriers in the GaAs that screen E_i. We note that the capture of carriers excited by the pump pulse is much larger than those excited by the HeNe laser.

7.3 Results and discussion

7.3.1 Spin capture, precession and relaxation

A TiMMS measurement taken with $P_{HeNe} = 0.38$ kW/cm^2 and $B = 0.35$ T is shown in Fig. 7.2. The observed time response consists of several parts. First, there is a peak in the TiMMS signal around zero delay, which we attribute to coherent higher order processes during temporal overlap of pump and probe beams. Second, after the coherent peak, the TiMMS signal is negative and rises exponentially toward a maximum positive value with a characteristic time much larger than the temporal width of the laser pulses. This exponential rise of the signal can be attributed to the capture of electron and holes, first excited in the wetting layer, into the quantum dots. Finally, the signal decays to zero and consists of an exponentially decaying part and an oscillatory component. In bulk materials, where the spin relaxation time of holes ($\tau_{s,h}$) is typically very short (< 1 ps) (Ref. [11]) due to the mixing of heavy and light hole states, one would expect a damped sine wave oscillating around zero due to electron spin precession and dephasing (with characteristic time $\tau_{s,e}$) when $B > 0$. Here, however, a striking difference is observed, as the signal does not oscillate around zero. Such a response may arise when $\tau_{s,h}$ is of the same order as $\tau_{s,e}$. This is very well possible in QDs, where similar to the situation in quantum wells [12], due to quantum confinement effects, the degeneracy between heavy and light holes is lifted. Therefore, the hole spins do not precess and $\tau_{s,h}$ is enhanced up to several orders of magnitude [13–15]. The fact that the first minimum reaches nearly zero signal indicates that equal amounts of electron and hole spins are present

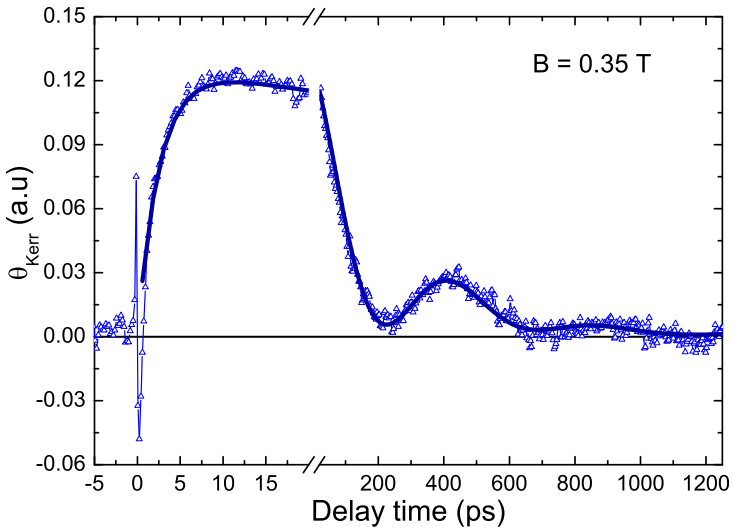

Figure 7.2: TiMMS signal with $B = 0.35$ T and $P_{HeNe} = 0.38$ kW/cm^2. The solid line is a fit of the data using Eq. 7.1.

in the system with comparable decay times.

Apart from the coherent peak, the full time response can be well described by the following fitting function:

$$\theta = A[1 - e^{-t/\tau_c}][e^{-t/T_{s,e}} cos(\omega t) + e^{-t/T_{s,h}}] \tag{7.1}$$

Here, A is the amplitude of the signal, τ_c the capture time (taken to be equal for both electron and holes, assuming charge neutrality), $T_{s,e}$ and $T_{s,h}$ the spin decay time time of electrons and holes, respectively, and the angular frequency of the precessing electrons. Fitting the response using Eq. 7.1, gives the following parameters: $\tau_c = 2.0 \pm 0.1$ ps, $T_{s,e} = 240 \pm 9$ ps, $T_{s,h} = 307 \pm 23$ ps, and $\omega = 13.8 \pm 0.3$ GHz. Indeed, $T_{s,e}$ and $T_{s,h}$ are of the same order of magnitude. Correcting for a recombination time of 1 ns (obtained from timeresolved PL measurement [9]) yields $\tau_{s,e} = 316$ ps and $\tau_{s,h} = 443$ ps and, thus, a large hole spin decoherence time is observed. From $\omega = g_{\parallel}\mu_B B/\hbar$, with μ_B the Bohr magneton, we find an absolute value of the in-plane electron g factor of $g_{\parallel} = 0.44$, which is in good agreement with recent theoretical predictions [7, 8]. We note that although we cannot determine the sign of the g factor, and although the absolute value is similar to the bulk g factor of GaAs, the observed capture time and the large hole spin decoherence time are indications that we are truly sensitive to spins in the quantum dots.

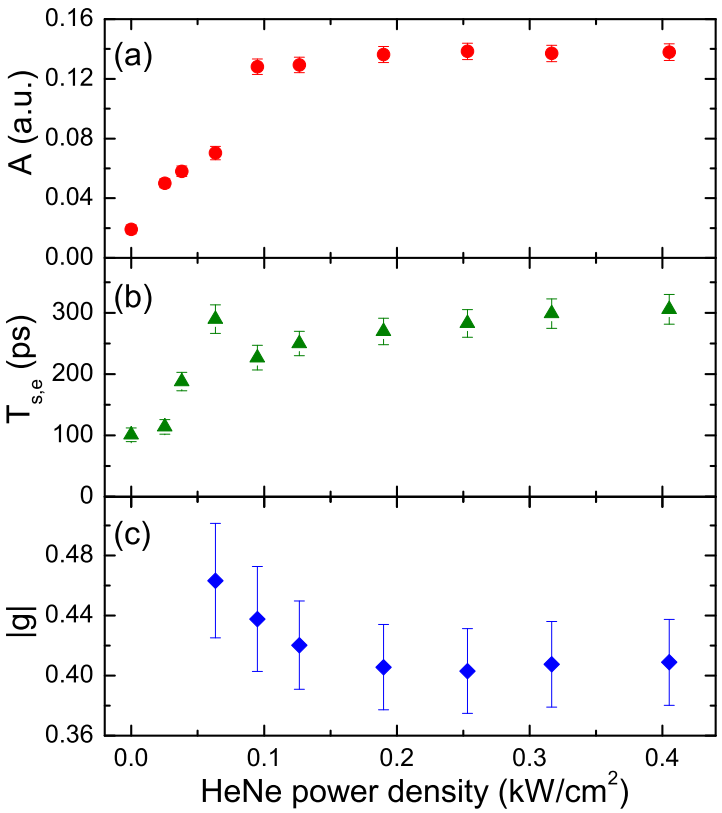

Figure 7.3: (a) The amplitude of the TiMMS signal, (b) electron spin decay time, and (c) electron g factor as a function of P_{HeNe}. Error margins result from the errors of the fitting procedure as well as from variations in different measurements.

7.3.2 Electric field dependence

We have performed similar measurements as a function of P_{HeNe}, from which we have extracted the amplitude A of the TiMMS signal, the electron spin decay time τ_e and the in-plane electron g factor $g_\parallel$, as shown in Fig. 7.3. Discussion of the hole spin decay times is beyond the scope of this paper. We note that in the analysis of some measurements, we omitted the exponential rise part of Eq. 7.1. We observe that A strongly depends on P_{HeNe} [Fig. 7.3(a)], rising from 0.02 at low P_{HeNe} (high E_i) to 0.14 when E_i is fully quenched. A similar dependence on P_{HeNe} is found for τ_e. These observations can be attributed to the increased loss of electron spin due to tunneling of electrons from the QDs to the GaAs at high E_i. As shown in Fig. 7.1, at high E_i, a triangular barrier between the QDs and the GaAs exists through which electrons can tunnel. As it is difficult to correct for the exact contribution of tunneling, we cannot conclude that the observed decrease in τ_e indicates a decrease in the electron spin decoherence time τ_{se}. Figure 7.3(c) shows the dependence of the electron g factor on P_{HeNe}. Although the uncertainty in the determination of $g_\parallel$ is rather large as a result of the combination of relative low B and small $g_\parallel$, these results indicate a slight increase of $g_\parallel$ from 0.40 ± 0.03 at high P_{HeNe} to 0.46 ± 0.04 at smaller P_{HeNe} (thus, increasing E_i). It is known that the electron g factor can change when the overlap of the wavefunction with the surrounding material changes, however, it is not trivial to predict what the change will be for these particular QDs.

7.4 Conclusion

In conclusion, we have performed time-resolved magneto-optical measurements on a single layer of selfassembled (In,Ga)As/GaAs QDs as a function of the built-in electric field E_i. We have observed electron spin precession and large hole spin decoherence times in the QDs. The decrease of the observed electron spin decay time with increasing E_i can be attributed to enhanced tunneling of electrons out of the QDs. Also, we have observed a slight increase of the electron in-plane g factor from 0.40 ± 0.03 to 0.46 ± 0.04 with increasing E_i, however, additional experiments are needed to fully resolve the behavior of $g_\parallel$ at high E_i.

Note added

We already mentioned that the electronic properties of quantum dots, and in particular the electron and hole g factors, depend strongly on the size and shape of the dots. According to calculations of Pryor and Flatté, for InAs self-assembled dots with a circular base, a height of ≈ 3 nm, and an optical gap of 1.3 eV, the electron g factor is close to $+0.4$, while the hole g factor is close to -0.15, for both in-plane directions. These calculation also show that dots with increased height show a decreased magnitude of electron g factors, and an increased magnitude of the hole g factors. Elongation of the base of the dot has a more rigorous effect

on the hole g factor, indicated by a change from -0.15 to -0.8 when the aspect ratio of the elliptical base is increased from 1 to 1.4 (again for an optical gap of 1.3). Further analysis of the atomic force microscopy images of the samples in the present study revealed an average dot elongation of about 1.6. Together with an average dot height of $\approx 6 - 7$ nm, this could imply a higher magnitude of the hole g factor compared to the electron g factor. If this is the case, the correct interpretation of the experimental data presented in this Chapter is that the observed precession is in fact precession of the hole spin. In Figures 7.2 and 7.3, the labels for electron and hole should then be interchanged.

Bibliography

[1] Z. Yuan, B. E. Kardynal, R. M. Stevenson, A. J. Shields, C. J. Lobo, K. Cooper, N. S. Beattie, D. A. Ritchie, and M. Pepper, *Electrically Driven Single-Photon Source*, Science **295**, 102 (2002). 7.1

[2] D. Loss and D. P. DiVincenzo, *Quantum computation with quantum dots*, Phys. Rev. A **57**, 120 (1998). 7.1

[3] G. Salis, Y. Kato, K. Ensslin, D. C. Driscoll, A. C. Gossard, and D. D. Awschalom, *Electrical control of spin coherence in semiconductor nanostructures*, Nature (London) **414**, 619-622 (2001). 7.1

[4] Y. Kato, R. C. Myers, D. C. Driscoll, A. C. Gossard, J. Levy, and D. D. Awschalom, *Gigahertz electron spin manipulation using voltage-controlled g-tensor modulation*, Science **299**, 1201-1204 (2003). 7.1

[5] T. Nakaoka, T. Saito, J. Tatebayashi, S. Hirose, T. Usuki, N. Yokoyama, and Y. Anakawa, *Tuning of g factor in self-assembled In(Ga)As quantum dots through strain engineering*, Phys. Rev. B **71**, 205301 (2005). 7.1

[6] M. F. Doty, M. Scheibner, I. V. Ponomarev, E. A. Stinaff, A. S. Bracker, V. L. Korenev, T. L. Reinecke, and D. Gammon, *Electrically Tunable g Factors in Quantum Dot Molecular Spin States*, Phys. Rev. Lett. **97**, 197202 (2006). 7.1

[7] C. E. Pryor and M. E. Flatté, *Landé g Factors and Orbital Momentum Quenching in Semiconductor Quantum Dots*, Phys. Rev. Lett. **96**, 026804 (2006). 7.1, 7.3.1

[8] W. Sheng and A. Babinski, *Zero g factors and nonzero orbital momenta in self-assembled quantum dots*, Phys. Rev. B **75**, 033316 (2007). 7.1, 7.3.1

[9] G. W. W. Quax, *All-optical control of the g factor in self-assembled (In,Ga)As/GaAs quantum dots*, Ph.D. Thesis, Eindhoven University of Technology, Eindhoven, The Netherlands (2008). 7.2.1, 7.3.1

[10] B. Koopmans, M. van Kampen, and W. J. M. de Jonge, *Electron and Hole Spin Dynamics in Magnetic Semiconductors*, Phys. Status Solidi B **215**, 217 (2000). 7.2.2

[11] D. J. Hilton and C. L. Tang, *Optical Orientation and Femtosecond Relaxation of Spin-Polarized Holes in GaAs*, Phys. Rev. Lett. **89**, 146601 (2002). 7.3.1

[12] R. W. Martin, R. J. Nicholas, G. J. Rees, S. K. Haywood, N. J. Mason, and P. J. Walker, *Two-dimensional spin confinement in strained-layer quantum wells*, Phys. Rev. B **42**, 9237-9240 (1990). 7.3.1

[13] K. Gündogdu, K. C. Hall, E. J. Koerperick, C. E. Pryor, M. E. Flatté, T. F. Boggess, O. B. Shchekin, and D. G. Deppe, *Electron and hole spin dynamics in semiconductor quantum dots*, Appl. Phys. Lett. **86**, 113111 (2005). 7.3.1

[14] S. Laurent, B. Eble, O. Krebs, A. Lemaître, B. Urbaszek, X. Marie, T. Amand, and P. Voisin, *Electrical Control of Hole Spin Relaxation in Charge Tunable InAs/GaAs Quantum Dots*, Phys. Rev. Lett. **94**, 147401 (2005).

[15] L. M. Woods, T. L. Reinecke, and R. Kotlyar, *Hole spin relaxation in quantum dots*, Phys. Rev. B **69**, 125330 (2004). 7.3.1

[16] J. Pingenot, C. E. Pryor, and M. E. Flatté, *Method for full Bloch sphere control of a localized spin via a single electrical gate*, Appl. Phys. Lett. **92**, 222502 (2008).

Summary

Spin dynamics in hybrid spintronic devices and semiconductor nanostructures

The research described in this Thesis is positioned in the field of Spintronics. The aim of this research field is to enable spin-based electronics (in contrast to contemporary charge based electronics), which should lead to improved device performance and new device functionalities. A well known example of a spintronics device is the giant magnetoresistive sensor used in computer hard disk drives to read the magnetic information. The development of this sensor followed only ten years after the discovery of the giant magnetoresistance (GMR) effect, a discovery which has been awarded with the Nobel Prize in physics in 2007. Another example of a spintronic device is the magnetoresistive random access memory (MRAM), which has the potential to become a universal non-volatile memory. In order to fully exploit the spin degree of freedom in conventional semiconductor devices, one has to be able to inject, manipulate, transport, and detect a spin polarization in a semiconductor system. In conventional semiconductors (such as silicon or gallium arsenide), a created spin polarization will not last forever as a result of several spin scattering mechanisms. Therefore, only a limited amount of time is available for spin manipulation and transport, which is essential for obtaining device functionality. Knowledge and control of the dynamic properties of spin in (hybrid) semiconductor devices is thus essential.

In this Thesis we have used time-resolved microscopic optical techniques to study spin and magnetization dynamics in hybrid spintronic devices and semiconductor nanostructures. The technique involves a so-called pump-probe scheme, in which the system under investigation is perturbed by a pump pulse, and in which the response of the system to this perturbation is measured by an optical probe pulse. In order to study magnetization dynamics in a ferromagnetic layer, the pump pulse is a magnetic field pulse, and the perturbation is measured via the magneto-optical Kerr-effect of the optical probe pulse. In case of semiconductor materials, the pump pulse is an optical pulse which creates a non-equilibrium spin polarization, while the evolution of this spin polarization is measured via (again) the magneto-optical Kerr-effect.

The basics of magnetization dynamics, and spin relaxation and precession are described in Chapter 2 of this Thesis. Also, we discuss the implications of optical excitation in the medium to high fluence regime on the spin dynamics. A detailed description of the experimental magneto-optical techniques is given in Chapter 3. In order to interpret the magneto-optical Kerr-signal originating from magnetic multilayers, and semiconductor heterostructures, we have performed a detailed analysis, thereby accounting for multiple interface reflections and the photon energy of the laser light. We discuss the applicability of the magneto-optical techniques and analysis with illustrative examples, such as the development of perpendicularly magnetized electrodes for spin injection, a system of two cobalt-platinum multilayer blocks suited for demagnetization experiments, and spin relaxation, precession and diffusion in a lateral spin injection device.

The main systems investigated in this Thesis are presented and discussed in the next Chapters, and involve a building block for an MRAM, a spin light-emitting diode, GaAs based nanowires, and (In,Ga)As quantum dots.

Chapter 4 presents spatio-temporal measurement of the magnetization dynamics in the free-magnetic layer of an MRAM-element. The observation of a non-uniform magnetization precession, in the form of the occurrence of localized modes at the edges of the micron sized element, implies an obstacle for uniform precessional switching of the magnetization. It is shown that the presence of a significant strayfield from the pinned layer is responsibly for these localized modes, and that this strayfield manifests itself in the domain structure of the magnetization of the free layer.

The dependence of the electron spin relaxation rate on the current through a spin-LED is investigated in Chapter 5. The main observation is a current-induced increase of the electron spin relaxation rate. Detailed measurements as a function of current, laser fluence, laser photon energy, and spatial position, together with device simulations, give a non-trivial picture of the spin relaxation in the spin-LED. The dominant contribution to the current-induced increase of the electron spin relaxation rate is by an increased hole density and temperature via the Bir-Aronov-Pikus spin flip mechanism.

In Chapter 6 the carrier and spin dynamics in GaAs-based nanowires is investigated. Spectroscopic measurements on an ensemble of multi-segmented GaP-GaAs nanowires show a rapid recombination rate of the optically excited carriers. This rapid recombination rate is attributed to a strong non-radiative recombination via defect or surface states, as a result of the large surface-to-volume ratio of these wires. It is shown that the experimental technique is capable of performing measurements on individual GaP-GaAs-GaP nanowires, and that it is possible to study a single segment of such a nanowire. Measurements on several nanowires show again a rapid recombination rate, while the spin lifetime seems to be limited by this rapid recombination. This limits the accurate determination of the intrinsic spin relaxation mechanisms.

The influence of an internal electric field on the g factor of electron and holes in a single layer of self-assembled (In,Ga)As quantum dots is the topic of Chapter 7. Measurement of spin relaxation and precession as a function of the internal electric field, show a decreasing spin lifetime and a small increase of the g factor when the internal electric field increases. Increasing tunnel probabilities of carriers out of the quantum dots at high internal electric field, and changing carrier wavefunctions due to a different confinement potential might explain these effect. These results might enable g factor (and thereby) spin manipulation in such quantum dots.

Samenvatting

Spin dynamics in hybrid spintronic devices and semiconductor nanostructures

Het onderzoek beschreven in dit proefschrift kan worden ondergebracht in het onderzoeksgebied 'Spintronica'. Dit onderzoeksgebied bestudeert en zoekt naar toepassingen die gebruik maken van de 'spin' van het electron. Het elektron zelf is het elementaire deeltje met een elektrische lading waarop de hedendaagse elektronica is gebaseerd. Een electron is echter ook een klein magneetje: het heeft een magnetisch moment dat 'spin' genoemd wordt. Het actieve gebruik van deze 'spin' in nieuwe 'spintronische' apparaatjes (ofwel devices), zal leiden tot betere prestaties en nieuwe functionaliteiten. Een zeer bekend 'spintronisch' device is de zogenaamde reuzen-magneto-weerstand sensor, die gebruikt wordt in de leeskop van harde schijven voor het lezen van de magnetische informatie. De ontwikkeling van deze revolutionaire sensor volgde slechts tien jaar na de ontdekking van het reuzen-magneto-weerstand effect, een ontdekking die bekroond is met de Nobelprijs voor de natuurkunde in 2007. Deze sensor heeft de stormachtige groei van de opslagcapaciteit van een harddisk gedurende het afgelopen decennium mogelijk gemaakt. Een ander voorbeeld is het magnetische random-access-memory, dat in de toekomst mogelijk een universeel niet-vluchtig geheugen zal vormen, waardoor de soms lange opstarttijd van een computer tot het verleden behoort.

Om de 'spin' van het electron volledig uit te buiten in huidige en toekomstige halfgeleider devices, moeten een aantal problemen worden opgelost. Deze bestaan onder andere uit het injecteren van een significante hoeveelheid 'spin' (ook wel spin polarisatie) in een halfgeleider, en het transporteren, manipuleren, en detecteren van deze spin-polarisatie. In de meest gebruikte halfgeleiders zoals silicium en gallium arsenide (GaAs), verdwijnt deze spin-polarisatie zeer snel, in typisch een miljardste van een seconde, door allerlei spin-relaxatie mechanismen. Hierdoor is er maar een beperkte tijd beschikbaar voor het uitvoeren van spin manipulatie en transport, terwijl dit essentieel is voor het maken van een werkend en functioneel device. Kennis van en controle over de dynamische eigenschappen van 'spin' in halfgeleider devices (of in halfgeleider-metaal, de zogenaamde hybride devices) is dus essentieel.

Voor het onderzoek beschreven in dit proefschrift, is gebruikt gemaakt van een tijd-, plaats- en spectraal opgeloste optische techniek om de dynamica van 'spin' en magnetisatie (de geordende spins in een magnetisch materiaal) te bestuderen in hybride spintronische devices en in halfgeleider nanostructuren. Deze stroboscopische techniek werkt volgens het pump-probe principe. Hierbij wordt een systeem verstoord ('gepompt') door een 'pump'-puls en wordt deze verstoring gemeten door een 'probe'-puls, waarbij de tijd tussen 'pump' en 'probe' puls nauwkeurig gecontroleerd kan worden tot beneden de picoseconde (een miljoenste van een miljoenste van een seconde). Om de magnetisatie dynamica te meten in een ferromagnetische laag, wordt als pomp een magnetische veld puls gebruikt en wordt de respons van de magnetisatie gemeten met een laser puls via het magneto-optische Kerr-effect. Om spin dynamica in halfgeleiders te meten, wordt als pomp een laser puls gebruikt die een spin polarisatie creëert in de halfgeleider. Het verval en gedrag van deze spin polarisatie wordt wederom gemeten met een laser puls via het magneto-optische Kerr-effect.

Na een introductie van het onderzoeksgebied Spintronica, wordt in Hoofdstuk 2 van dit proefschrift een beschrijving gegeven van magnetisatie dynamica in ferromagnetische materialen, en van spin dynamica in halfgeleiders. Met name de spin relaxatie mechanismen in GaAs komen aan bod en de implicaties van spin relaxatie en precessie in $n-$gedoteerd GaAs na optische excitatie met een relatief sterke laser puls worden met enkele numerieke modellen uitgewerkt. In Hoofdstuk 3 worden de experimentele technieken in detail beschreven, waarbij het magneto-optische Kerr-effect een centrale rol inneemt. Met name wordt aandacht besteed aan de analyse van het Kerr-effect dat afkomstig is uit magnetische multilagen en halfgeleider heterostructuren, waarbij rekening wordt gehouden met meervoudige grensvlak reflecties en de golflengte van de laser pulse. Met enkele illustratieve voorbeelden (zoals de ontwikkeling van loodrecht gemagnetiseerde electroden voor spin injectie, een systeem van twee blokken met cobalt-platina multilagen voor demagnetisatie experimenten, en spin relaxatie, precessie en diffusie in een lateraal spin injectie device) wordt de kracht van deze technieken en analyse toegelicht.

De belangrijkste devices en structuren die in het kader van dit proefschrift zijn onderzocht, worden gepresenteerd in de Hoofdstukken 4 tot en met 7. Het betreft hier een bouwsteen van een magnetisch geheugen, een spin-LED, halfgeleider nanodraden gemaakt van GaAs, en zogenaamde quantum dots bestaande uit een mix van indium arsenide en gallium.

Hoofdstuk 4 beschrijft de tijd- en plaats-opgeloste metingen van de magnetisatie dynamica in de vrije laag van een magnetische tunneljunctie (met afmetingen van 13 bij 9 micrometer), die een bouwsteen vormt van een magnetisch geheugen. Deze metingen laten een niet-uniforme respons van de magnetisatie op een magnetische veld puls zien. De precessie van de magnetisatie die volgt op deze magnetische puls heeft aan de randen van de vrije laag een andere frequentie en uitdoving dan in het midden van het element. Dit gedrag bemoeilijkt het snel uniform precessioneel

switchen van de magnetisatie van de vrije laag. Aangetoond wordt dat de oorzaak van dit gedrag het magnetisch strooiveld afkomstig van de niet-vrije laag van de tunneljunctie is, en dat dit strooiveld ook de domein structuur van de vrije beïnvloed.

In Hoofdstuk 5 wordt aangetoond dat de effectiviteit van de spin relaxatie van elektronen in de actieve laag van een spin-LED toeneemt met de stroom door deze spin-LED. Gedetailleerde experimenten, waarbij zowel de stroom, het laser vermogen, de golflengte van de laser, en de plaats op de spin-LED zijn gevarieerd, laten zien dat de dominante bijdrage aan de toegenomen effectiviteit van spin relaxatie kan worden toegeschreven aan een verhoogde gaten-dichtheid en temperatuur in de active laag van de spin-LED. Het relaxatie-mechanisme dat hiervoor zorgt is het zogenaamde Bir-Aronov-Pikus-mechanisme. Deze waarnemingen zijn in goede overeenstemming met numerieke simulaties van de stroom, gaten-dichtheid, en temperatuur van de spin-LED.

De dynamica van ladingsdragers en spins in halfgeleider nanodraden gebaseerd of GaAs wordt besproken in Hoofdstuk 6. Spectroscopische metingen aan een grote verzameling nanodraden bestaande uit segmenten van gallium fosfide (GaP) en GaAs laten een zeer snelle recombinatie zien van ladingsdragers na optische excitatie met een laser puls. Deze zeer snelle recombinatie wordt toegeschreven aan een sterke niet-stralende recombinatie aan defecten in het rooster of aan het oppervlak van de nanodraden, tengevolge van de grote oppervlakte-volume verhouding. Gedemonstreerd wordt dat de experimentele techniek het mogelijk maakt om metingen te verrichten aan individuele nanodraden, en dat zelfs een enkel segment in een GaP-GaAs-GaP nanodraad kan worden geïdentificeerd. Metingen aan verscheidene nanodraden laten wederom een zeer snelle recombinatie van ladingsdragers zien. Magneto-optische metingen duiden op een spin levensduur die gelimiteerd wordt door deze snelle recombinatie, wat een nauwkeurige meting van de intrinsieke spin levensduur bemoeilijkt.

In Hoofdstuk 7 wordt de invloed van een intern elektrisch veld op de spin relaxatie en de g factor van elektronen en gaten in een enkele laag van zelf-samengestelde (In,Ga)As quantum dots onderzocht. Het actief kunnen veranderen van de g factor moet het mogelijk maken om spins in quantum dots te kunnen manipuleren. Metingen van de spin relaxatie en precessie als functie van het intern elektrisch veld, laten zien dat de spin levensduur verminderd en de g factor enigszins groter wordt, naarmate de sterkte van het intern elektrisch veld stijgt. Deze afhankelijkheid van het elektrisch veld kan mogelijk worden toeschreven aan een veranderende opsluitingspotentiaal van ladingsdragers in de quantum dot, en aan veranderde waarschijnlijkheden voor ladingsdragers om uit de quantum dot te tunnelen.

List of publications

J. H. H. Rietjens, C. A. C. Bosco, P. Van Dorpe, W. Van Roy, and B. Koopmans
Current-induced increase of the electron spin relaxation rate in a spin-LED
In preparation

J. H. H. Rietjens, C. A. C. Bosco, M. T. Borgström, E. P. A. M. Bakkers, and B. Koopmans
Probing carrier and spin dynamics in GaAs-based nanowires
In preparation

G. Malinowski, F. Dalla Longa, J. H. H. Rietjens, P. V. Paluskar, R. Huijink, H. J. M Swagten, and B. Koopmans
Control of speed and efficiency of ultrafast demagnetization by direct transfer of spin angular momentum
Nat. Phys. **4**, 855 (2008).

J. H. H. Rietjens, G. W. W. Quax, C. A. C. Bosco, R. Nötzel, A. Yu. Silov, and B. Koopmans
Optical control over electron g factor and spin decoherence in (In,Ga)As/GaAs quantum dots
J. Appl. Phys. **103**, 07B116 (2008)

G. W. W. Quax, T. E. J. Campbell Ricketts, A. M. Yakunin, T. van Lippen, R. Nötzel, P. M. Koenraad, C. A. C. Bosco, J. H. H. Rietjens, B. Koopmans, and A. Yu. Silov
All-optical control of the exciton g-factor in InAs/GaAs quantum dots
Phyica. E **40**, 1832-1835 (2008)

J. H. H. Rietjens, C. Józsa, H. Boeve, W. J. M. de Jonge, and B. Koopmans
Effect of stray field on local spin modes in exchange-biased magnetic tunnel junction elements
Appl. Phys. Lett. **87**, 172508 (2005)

J. H. H. Rietjens, C. Józsa, H. Boeve, W. J. M. de Jonge, and B. Koopmans
Probing local spin modes in exchange-biased MTJ elements
J. Magn. Magn. Mater. **290**, 494-497 (2005).

C. Józsa, J. H. H. Rietjens, M. van Kampen, E. Smalbrugge, M. K. Smit, W. J. M. de Jonge, and B. Koopmans
Retrieving pulse profiles from pump-probe measurements on magnetization dynamics
J. Appl. Phys. **95**, 7447 - 7449 (2004)

About the author

Jeroen Henricus Hubertus Rietjens was born on October 18$^{\text{th}}$ 1978 in Weert, the Netherlands. He grew up in Nederweert and attended the Philips van Horne Scholengemeenschap in Weert, where he received his VWO-diploma in June 1997.

Between September 1997 and April 2004 he studied Applied Physics at the Eindhoven University of Technology (TU/e). He did internships at the group Plasma and Materials Processing (TU/e), Vanderlande Industries, and at the Institute for Astronomy in Honolulu, Hawaii. His final project was carried out in the group Physics of Nanostructures (TU/e), and concerned precessional magnetization dynamics in micron sized ferromagnetic elements. He received is Master in Applied Physics (cum laude) in April 2004, and was awarded the Mignot Award for best master thesis of the Eindhoven University of Technology of 2004.

Between April 2004 and December 2008 he has been working as a PhD-candidate in the group Physics of Nanostructures (TU/e) on a research project within the NanoNed initiative. His research focused on the magnetization and spin dynamics in hybrid spintronic devices and semiconductor nanostructures. This work has led to several publications in renowned scientific journals and presentations at international conferences.

Besides his professional activities, he has been a member of the board of the study-association for Applied Physics "Johannes Diderik van der Waals", and is at present Secretary of VENI, the alumni-association of Applied Physics in Eindhoven, and Treasurer of Stichting Natuurkunst, a foundation whose main activity was the realization of a grand public artwork, SOH19 States of Nature, at the entrance of the campus of the TU/e.

Dankwoord

Met deze laatste woorden van mijn proefschrift wil ik graag iedereen bedanken die op zijn of haar manier een bijdrage heeft geleverd aan het totstandkomen van dit werk.

In het bijzonder gaat mijn dank uit naar mijn promotoren, Bert Koopmans en Henk Swagten, en commissielid Wim de Jonge. Zij hebben niet alleen deze promotieplaats mogelijk gemaakt, maar ook gezorgd voor goede begeleiding, aansturing, kritische vragen, op de juiste momenten gezonde motiverende prikkels, en niet in de laatste plaats voor de fantastische sfeer in de groep Fysica van Nanostructuren. Het zijn deze zaken die mij houvast hebben geboden en mij in staat hebben gesteld om mijn promotieonderzoek tot een goed einde te brengen.

Bert, bedankt voor je vertrouwen, je enthousiasme en geduld, je grondige kennis en het bijna altijd vinden van antwoorden en mogelijke oplossingen op mijn vragen over theorie en experiment. Het was een eer om in jouw groep te mogen werken, ik heb er ontzettend veel van geleerd. Henk, bedankt voor je adviezen en luisterend oor, zowel in N-laag als af en toe in de trein naar Weert, zowel met betrekking tot mijn onderzoek als (ver) daarbuiten en voor de goede correcties en suggesties bij het schrijven van dit proefschrift. Wim, bedankt voor je interesse in mijn onderzoek en de soms confronterende (maar wel noodzakelijke) vragen tijdens de werkbesprekingen. De gesprekken over de meest uiteenlopende zaken die volgden op het 'even goedendag zeggen' vormden een welkome afleiding. Het was me een genoegen me te mogen verdiepen in de meest onwaarschijnlijke problemen met computers en internet die alleen jou leken te overkomen.

Bedankt ook mijn co-promotor Erik Bakkers en Magnus Borgström van Philips Research voor de samenwerking op het gebied van halfgeleider nanodraden, met name voor het leveren van de samples en voor verhelderende discussies. Hetzelfde geldt voor Wim Van Roy, Pol Van Dorpe en Reinier Vanheertum van IMEC Leuven, voor de samenwerking met de spin-LED en de spin injectie devices, en voor Guido Quax en Andrei Silov voor het quantum dot project. Deze samenwerkingen hebben mij de mogelijkheid geboden om met systemen te werken die niet binnen de groep FNA vervaardigd konden worden en hebben in alle gevallen geleid tot mooie resultaten en vormen ieder een essentieel onderdeel van dit proefschrift.

De nog niet genoemde commissieleden Andrea Fiore, Paul van Loosdrecht en

Gerd Bacher wil ik danken het plaatsnemen in de promotiecommissie en voor het kritisch lezen van mijn proefschrift.

Vanzelfsprekend gaat veel dank uit naar iedereen van de groep FNA voor het vormen van een gezonde werkomgeving, de sportieve afleiding met zaal- en veldvoetbal, en de gezelligheid in de koffiekamer tijdens de pauze, Sinterklaas-, Kerst- en champagnepartijtjes en tijdens groepsuitjes en conferenties. Jürgen, Oleg, Gerrie, Jef en Jeroen, bedankt voor jullie assistentie bij experimenten en technische problemen. Karin, bedankt voor al het administratieve werk en de vele op maat gesneden adviezen met betrekking tot het gezinsleven. Uiteraard gaat mijn dank uit naar de promovendi en post-docs met wie ik gedurende mijn verblijf in de groep FNA heb gewerkt: de laserlabpers Carlos, Francesco, Greg en Csaba, de groeiers Paresh, Jurgen, Corine, Reinoud en Coen, de molecuulmannen Francisco en Wiebe, de NMR-ers Sabine en Harm, de STM-ers Muriel en Omer, en de schrijvers van 2004 Veronica, Karel en Corné.

Van de vele afstudeerders en stagiaires die in de groep FNA hebben gewerkt, gaat mijn speciale dank uit naar Sebastiaan Rieter, Paul Claassen, William Hermkens, Wim van Hemmen en Joost van Bree. Het was me een genoegen om jullie te mogen begeleiden en te profiteren van het vele goede werk dat jullie hebben verricht.

Tijdens mijn promotieonderzoek ben ik ook vele malen geholpen door personen buiten de groep FNA. Met name wil ik Marius, Han, Henk, Frank, Ginny en Marco van de werkplaats, Rens, Toon en Marieke van de receptie, en Karin Raijmakers en Jan Millenaar graag hartelijk bedanken voor de meest uiteenlopende hulp.

Natuurlijk ben ik ook veel dank verschuldigd aan personen die de gedurende mijn promotieonderzoek mijn zogenaamde neven- en sociale activiteiten tot een waar plezier hebben gemaakt en daarmee ook voor motivatie en inspiratie voor mijn onderzoek hebben gezorgd.

In het bijzonder wil ik alle (bestuurs)leden van Stichting Natuurkunst bedanken voor de prettige samenwerking en het gigantisch mooie resultaat dat we samen hebben bereikt en dat hopelijk tot in de lengte van dagen te aanschouwen zal zijn op de campus van de TU/e. Ook de bestuursleden van alumnivereniging VENI (Saskia, Jan-Jaap, Igor, Sonja, Erik, Patrick, Wiebe, Daniel en Thijs) dank ik voor de vele gezellige vergaderingen en het goede werk dat we samen hebben verricht. Veel dank aan de Heeren van Evolutie voor vele ontspannende en hilarische momenten tijdens uitstapjes, etentjes en andere activiteiten. Hetzelfde geldt voor de leden van Stiefelcommissie Natuurkunde, met name tijdens het befaamde Stiefelweekend. Dank ook aan mijn teamgenoten van Eindhoven AV3/4 (het spijt me dat mijn knie tot tweemaal toe roet in het eten heeft gegooid), en aan de Snarfjes, Aanhangsnarfjes en Babysnarfjes.

Tenslotte wil ik mijn grote dank uitspreken aan mijn familie, die gedurende mijn gehele onderzoeksperiode, maar zeker ook in de laatste fase een enorme steun zijn geweest. Mijn ouders Henk en Corry, mijn zus Ellen en Wilfred, mijn schoonouders Wiel en Lenie en schoonbroer Hubert, heel, heel veel dank. Femke, ook tot jou

wil ik nog enkele woorden richten. Jouw komst was een moment was een moment van grote blijdschap, het was heerlijk om je te zien opgroeien en te zien spelen met Huub. De klap van jouw verlies zullen we misschien nooit te boven komen, vergeten zal ik je in ieder geval nooit.

Als allerlaatste gaat mijn dank uit naar degenen die het dichtst bij mij staan. Willy, ik kan onmogelijk in woorden uitdrukken hoeveel je voor me betekent en hoeveel steun ik aan je heb gehad. We hebben gedurende de tijd van mijn promotieonderzoek vele grote stappen gezet die onze relatie alleen maar hebben verrijkt. Samen met Huub en Guus, die ons iedere dag weer laten beseffen hoe gelukkig we zijn en die de gouden gave bezitten om op willekeurige momenten met een onschuldige opmerking, handeling of boevenstreek een lach op ons gezicht te toveren, zie ik de toekomst vol vertrouwen tegemoet.